

**THE DEVELOPMENT OF A NEW TESTING
METHODOLOGY IN DYNAMIC MECHANICAL
CHARACTERIZATION OF CONCRETE**

**A Thesis Submitted to
The Graduate School of Engineering and Sciences of
Izmir Institute of Technology
in Partial Fulfillment of the Requirements for the Degree of**

MASTER OF SCIENCE

in Mechanical Engineering

**by
Semih Berk SEVEN**

July 2018

İZMİR

We approve the thesis of **Semih Berk SEVEN**

Examining Committee Members:

Prof. Dr. Alper TAŞDEMİRÇİ

Department of Mechanical Engineering, İzmir Institute of Technology

Assist. Prof. Dr. Selçuk SAATCI

Department of Civil Engineering, İzmir Institute of Technology

Assist. Prof. Dr. Levent AYDIN

Department of Mechanical Engineering, İzmir Katip Çelebi University

04 July 2018

Prof. Dr. Alper TAŞDEMİRÇİ

Supervisor, Department of
Mechanical Engineering
İzmir Institute of Technology

Prof. Dr. Mustafa GÜDEN

Co-Supervisor, Department of
Mechanical Engineering
İzmir Institute of Technology

Prof. Dr. Metin TANOĞLU

Head of the Department of
Mechanical Engineering

Prof. Dr. Aysun SOFUOĞLU

Dean of the Graduate School of
Engineering and Sciences

ACKNOWLEDGMENTS

I would like to thank my advisor Prof. Dr. Alper TAŞDEMİRÇİ for inspiring and encouraging me during my thesis study. His support, guidance, and expertise during this study helped me to complete my thesis. I also would like to thank my co-advisor Prof. Dr. Mustafa GÜDEN for his invaluable comments, endless support, and contributions to my thesis.

I would like to state that my thankfulness to TUBITAK (Scientific and Technological Council of Turkey) for the financial support to the project number 115M534. Also, I express my appreciations Dr. Selçuk SAATCI for his contributions and my special thanks to my colleagues Dr. M. Alper ÇANKAYA and Çetin Erkam UYSAL for their collaboration, support, and hard work during this project.

I wish to thank to all my colleagues and friends at İzmir Institute of Technology; Ali Kıvanç TURAN, Emine Fulya AKBULUT, Fırat TÜZGEL, Erkan GÜZEL, Mustafa Kemal SARIKAYA, Mesut BAYHAN, and Orhan ORAL for their friendship, support, and association.

Furthermore, I want to express my gratitude to my father Selçuk SEVEN, my mother Şerife SEVEN and my brother Sener SEVEN for their emotional support during completion of my thesis.

Lastly, I would like to thank my dear girlfriend Pınar KESKİN whose love and endless support encouraged me to overcome this hardworking study.

ABSTRACT

THE DEVELOPMENT OF A NEW TESTING METHODOLOGY IN DYNAMIC MECHANICAL CHARACTERIZATION OF CONCRETE

Concrete is one of the most used material types in the world. Due to its structural complexity and insufficient testing techniques, the dynamic mechanical behavior of concrete has not yet been revealed sufficiently. This thesis aims to develop reliable and accurate mechanical characterization methodology for concrete using the combination of experimental and numerical methods together. The dynamic mechanical characterization of concrete at quasi-static and high strain rates was performed implementing unique techniques for both experimental and numerical studies. In quasi-static testing, universal compression test machine was used with strain gage mounted specimen for better strain measurements. In high strain rate tests, two modifications were implemented on the conventional Split Hopkinson Pressure Bar (SHPB) test apparatus. The first modification is the usage of pulse shaper to obtain nearly constant strain rate and dynamic stress equilibrium in the specimen. Second, piezo-electric quartz crystal force transducers were implemented on the specimen-bar interfaces to increase accuracy and sensitivity of the force measurement on the front and back forces of the specimen. Experimental results were validated constituting numerical study using finite element tool LS-DYNA. Concrete was modeled using Holmquist-Johnson-Cook (MAT_111) material model. HJC material model parameters were determined using experimental results coupling with the numerical analysis and the mechanical behavior of concrete was constituted. It was concluded that using pulse shaper and quartz crystals pretty useful when testing concrete and other brittle materials at high strain rates. Modification of new specimen geometries on numerical analysis showed better understandings of the effect of geometry on the dynamic stress equilibrium.

ÖZET

BETONUN DİNAMİK MEKANİK KARAKTERİZASYONU İÇİN YENİ BİR TEST METODOLOJİSİNİN GELİŞTİRİLMESİ

Beton, dünyada en çok kullanılan malzeme tiplerinden biridir. Yapısal karmaşıklığı ve yetersiz test teknikleri nedeniyle betonun dinamik mekanik davranışı henüz yeterince açığa çıkarılmamıştır. Bu çalışmada, deneysel ve sayısal yöntemler birlikte kullanılarak test metodolojisindeki iyileştirmelerle birlikte betonun güvenilir ve doğru bir mekanik karakterizasyonunun geliştirilmesi amaçlanmıştır. Kuasi-statik ve yüksek şekil değiştirme hızlarında betonun dinamik mekanik karakterizasyonu, hem deneysel hem de sayısal çalışmalarda özgün teknikler kullanılarak gerçekleştirilmiştir. Kuasi-statik testler, daha iyi şekil değiştirme ölçümleri için gerinim ölçerler test numunesi üzerine yapıştırılarak üniversal basma cihazı kullanılarak gerçekleştirilmiştir. Yüksek şekil değiştirme hızlarındaki testlerde, konvansiyonel Split Hopkinson Basınç Barı (SHBB) test cihazında iki değişiklik yapılmıştır. İlk değişiklik, numunede neredeyse sabit şekil değiştirme hızı ve dinamik gerilme dengesi elde etmek için darbe şekillendiricinin kullanılmasıdır. İkinci değişiklik ise, numunenin ön ve arka kuvvetleri üzerindeki kuvvet ölçümünün doğruluğunu ve hassasiyetini arttırmak içsssin numune-bar arayüzlerine piezo-elektrik kuvarz kristal uygulamasıdır. Deneysel sonuçlar, sonlu elemanlar yazılımı LS-DYNA kullanılarak nümerik olarak doğrulanmıştır. Beton malzemesi, Holmquist-Johnson-Cook (MAT_111) malzeme modeli kullanılarak modellenmiştir. HJC malzeme modeli parametreleri, nümerik analiz ile deneysel sonuçlar kullanılarak belirlenmiş ve betonun dinamik mekanik yükler altındaki davranışı oluşturulmuştur. Darbe şekillendirici ve piezo-elektrik kuvars kristallerin yüksek şekil değiştirme hızı testlerinde beton ve benzeri diğer kırılğan malzemelerin test edilmesinde oldukça yararlı olabileceği sonucuna varılmıştır. Yeni numune geometrilerinin nümerik analizlerde modellenmesi ile, numune geometrisinin dinamik gerilim dengesi üzerindeki etkisi daha iyi anlaşılması sağlanmıştır.

TABLE OF CONTENTS

| | |
|--|-----|
| LIST OF FIGURES | vii |
| LIST OF TABLES..... | xi |
| CHAPTER 1. INTRODUCTION..... | 1 |
| 1.1 Introduction..... | 1 |
| 1.2 Literature Review | 3 |
| 1.3 Scope of the Study | 20 |
| CHAPTER 2. EXPERIMENTAL METHODOLOGY | 22 |
| 2.1 Introduction..... | 22 |
| 2.2 Concrete Material | 22 |
| 2.3 Quasi-Static Testing..... | 23 |
| 2.4 High Strain Rate Testing..... | 27 |
| 2.4.1 SHPB Apparatus | 28 |
| 2.4.2 SHPB Theory | 33 |
| CHAPTER 3. EXPERIMENTAL RESULTS AND CHARACTERIZATION | 40 |
| 3.1 Introduction..... | 40 |
| 3.2 Experimental Results | 40 |
| 3.3 Johnson-Holmquist-Cook Material Model | 67 |
| 3.4 Determination of Model Parameters..... | 70 |
| CHAPTER 4. NUMERICAL STUDY | 76 |
| 4.1 Introduction..... | 76 |
| 4.2 Modeling of SHPB Test and Numerical Results | 77 |
| 4.3 Numerical Study on the SHPB Specimen Geometry..... | 85 |
| CHAPTER 5. CONCLUSIONS | 90 |
| REFERENCES | 93 |

LIST OF FIGURES

| <u>Figure</u> | <u>Page</u> |
|--|--------------------|
| Figure 1.1. Loading techniques to achieve a variety of strain rate range at different loading conditions | 3 |
| Figure 1.2. Apparatus developed by Bertram Hopkinson for the measurement of pressure | 5 |
| Figure 1.3. Kolsky's apparatus | 6 |
| Figure 1.4. Lindholm's SHPB test setup | 7 |
| Figure 1.5. Strain rate effect on the compressive strength of concrete..... | 9 |
| Figure 1.6. Schematic of modified split Hopkinson pressure bar with the implementation of quartz crystals..... | 11 |
| Figure 1.7. Influence of inertial confinement for homogeneous and mesoscale concrete model | 15 |
| Figure 1.8. Various cases of specimen and insert geometries 1) Metallic specimen without inserts, (2) Ceramic specimen without inserts, (3) Cylindrical WC inserts only, (4) Conical Al ₂ O ₃ inserts only, (5) Ceramic specimen with cylindrical WC inserts, (6) Ceramic specimen with conical Al ₂ O ₃ inserts, (7) Dog-bone specimen with matching diameters, (8) Dog-bone specimen with non-matching diameters. | 19 |
| Figure 2.1. Prismatic concrete mold and core-drilled cylindrical test specimen | 23 |
| Figure 2.2. Quasi-static test setup..... | 25 |
| Figure 2.3. Test specimen with strain gages..... | 26 |
| Figure 2.4. Split-tensile testing of a concrete | 27 |
| Figure 2.5. Schematic of SHPB bar..... | 28 |
| Figure 2.6. Piezo-electric quartz crystal bonded to the aluminum bar and the concrete specimen sandwiched between bars..... | 31 |
| Figure 2.7. Data acquisition and video recording system in the SHPB..... | 31 |
| Figure 2.8. Pulse shaper insertion on the impact face of the incident bar | 32 |
| Figure 2.9. Split Hopkinson Pressure Bar test setup..... | 33 |
| Figure 2.10. A typical voltage-time history of a SHPB test of concrete | 34 |

| | |
|---|----|
| Figure 2.11. Schematic of the testing area of split Hopkinson pressure bar..... | 35 |
| Figure 3.1. Test 1 stress-strain curve at 10^{-4} s^{-1} strain rate | 41 |
| Figure 3.2. Test 2 stress-strain curve at 10^{-4} s^{-1} strain rate | 41 |
| Figure 3.3. Test 3 stress-strain and Poisson's ratio 10^{-4} s^{-1} strain rate..... | 42 |
| Figure 3.4. Test 3 actual strain rate fit at 0.0045 mm/s cross head speed | 43 |
| Figure 3.5. Stress-strain comparison at 10^{-4} s^{-1} strain rate..... | 43 |
| Figure 3.6. Test 1 stress-strain curve for 10^{-3} s^{-1} strain rate..... | 44 |
| Figure 3.7. Test 2 stress-strain curve for 10^{-3} s^{-1} strain rate..... | 44 |
| Figure 3.8. Test 3 stress-strain and Poisson's ratio 10^{-3} s^{-1} strain rate..... | 45 |
| Figure 3.9. Test 3 actual strain rate fit at 0.045 mm/s cross head speed | 45 |
| Figure 3.10. Stress-strain comparison at 10^{-3} s^{-1} strain rate..... | 46 |
| Figure 3.11. Test 1 stress-strain curve for 10^{-2} s^{-1} strain rate..... | 46 |
| Figure 3.12. Test 2 stress-strain curve for 10^{-2} s^{-1} strain rate..... | 47 |
| Figure 3.13. Test 3 stress-strain and Poisson's ratio 10^{-2} s^{-1} strain rate..... | 47 |
| Figure 3.14. Test 3 actual strain rate fit at 0.45 mm/s cross head speed | 48 |
| Figure 3.15. Stress-strain comparison at 10^{-2} s^{-1} strain rate..... | 48 |
| Figure 3.16. Stress-strain comparison at different strain rates | 49 |
| Figure 3.17. Split tensile test results | 50 |
| Figure 3.18. Split tensile test damage history of the specimen (a) undamaged, (b) first crack formation (c) damaged specimen..... | 50 |
| Figure 3.19. Stress histories of the without pulse shaper tests | 52 |
| Figure 3.20. Stress wave analysis of the test without pulse shaper | 53 |
| Figure 3.21. Strain-Strain rate history of the without pulse shaper test..... | 53 |
| Figure 3.22. Force histories of the bar-specimen interfaces and quartz crystals of the without pulse shaper test | 54 |
| Figure 3.23. Stress-strain curve comparison of the 1-wave stress analysis and the incident piezo stress of the without pulse shaper test | 55 |
| Figure 3.24. Stress histories of the with pulse shaper tests..... | 56 |
| Figure 3.25. Stress wave analysis of the test with a pulse shaper..... | 57 |
| Figure 3.26. Strain-Strain rate history of the with pulse shaper test..... | 57 |
| Figure 3.27. Force histories of the bar-specimen interfaces and quartz crystals of the with pulse shaper test | 58 |
| Figure 3.28. Stress-strain curve comparison of the 1-wave stress analysis and the incident piezo stress of the with pulse shaper test..... | 59 |

| | |
|---|----|
| Figure 3.29. The effect of pulse shaper on the incident pulse shape | 60 |
| Figure 3.30. The effect of pulse shaper on the 1-wave stress analysis and stress produced by piezo-electric quartz crystals..... | 60 |
| Figure 3.31. The effect of pulse shaper on the strain-strain rate behavior | 61 |
| Figure 3.32. The effect of pulse shaper on the dynamic stress equilibrium parameter | 62 |
| Figure 3.33. Stress-strain and modulus of elasticity comparison of dynamic and quasi-static tests | 63 |
| Figure 3.34. The deformation initiation/progression of a quasi-static compression test..... | 65 |
| Figure 3.35. The deformation initiation/progression of a SHPB test | 66 |
| Figure 3.36. Normalized pressure-equivalent stress relation of the HJC model | 68 |
| Figure 3.37. Normalized pressure and damage relation of HJC model | 69 |
| Figure 3.38. The hydrostatic pressure-volume relation of HJC model..... | 70 |
| Figure 3.39. Strain rate sensitivity parameter fit | 72 |
| Figure 3.40. Pressure-Shear strength relation for 48 MPa and 140 MPa concrete slabs..... | 72 |
| Figure 3.41. Transmitter bar stress and numerical trials..... | 73 |
| Figure 3.42. Stress-strain results of a cyclic compression test | 74 |
| Figure 4.1. Numerical model of the Split Hopkinson Pressure Bar test..... | 77 |
| Figure 4.2. Stress history of the numerical test without pulse shaper | 78 |
| Figure 4.3. Experimental and numerical Comparison of stress-strain wave analysis of test without pulse shaper..... | 79 |
| Figure 4.4. Numerical stress wave analysis of the test without pulse shaper | 80 |
| Figure 4.5. Comparison of the experimental and numerical strain-strain rate history of the without pulse shaper test | 80 |
| Figure 4.6. Comparison of the experimental and numerical $R(t)$ parameter | 81 |
| Figure 4.7. Stress history of the numerical test with pulse shaper..... | 82 |
| Figure 4.8. Experimental and numerical Comparison of stress-strain wave analysis of test with pulse shaper..... | 83 |
| Figure 4.9. Numerical stress wave analysis of the test with pulse shaper | 84 |
| Figure 4.10. Comparison of the experimental and numerical strain-strain rate history of the test with pulse shaper..... | 84 |

| | |
|--|----|
| Figure 4.11. Comparison of the experimental and numerical $R(t)$ parameter | 85 |
| Figure 4.12. Numerical test specimens with different L/D ratio | 86 |
| Figure 4.13. The effect of L/D ratio on the dynamic stress equilibrium parameter in the test without pulse shaper | 87 |
| Figure 4.14. The effect of L/D ratio on the dynamic stress equilibrium parameter in the test with pulse shaper | 87 |
| Figure 4.15. Numerical test specimens with different R_i/R_o ratio | 88 |
| Figure 4.16. The effect of annular specimen geometry on the dynamic stress equilibrium parameter in the test without pulse shaper | 89 |
| Figure 4.17. The effect of annular specimen geometry on the dynamic stress equilibrium parameter in the test with pulse shaper | 89 |

LIST OF TABLES

| <u>Table</u> | <u>Page</u> |
|---|--------------------|
| Table 2.1. Physical properties of the 7075-T6 aluminum pressure bars..... | 29 |
| Table 3.1. Mechanical properties of concrete at quasi-static strain rates | 49 |
| Table 3.2. Johnson Holmquist Cook material model parameters | 75 |

CHAPTER 1

INTRODUCTION

1.1 Introduction

Concrete is a composite, non-homogenous and porous material which is composed of water, cement, sand, and aggregate. The very early form of concrete was used in Egyptian pyramids back to 5000 years ago. Then, ancient Romans used a very similar concrete-like material on their buildings 2000 years ago. The concrete material has been developed over the years and the modern use of concrete was discovered in the 19th century with the invention of Portland cement. In the same century, the first tension and compression tests of concrete material were made. The strength tests on the concrete lead to adding reinforcements to the concrete mixture in order to increase the tensile strength of the concrete material. Nowadays, concrete has a variety of usage as a structural material such as roads, bridges, dams, houses, military applications, nuclear power plants and space station constructions. The reasons for the wide range of usage of concrete structures are mainly thanks to its manufacturability, durability, lifetime, strength properties and ease of use.

Concrete structures may be exposed to various loading conditions such as environmental effects, explosives, earthquakes, and terrorist attacks. Therefore, researchers have made a great deal of investigation in order to have a better understanding about the dynamic behavior of concrete at different loading conditions. Several test methods have been developed by researchers to determine the mechanical behavior of concrete. On beside of testing methodology, there has been much work held on the finite element modeling of concrete structures to represent the behavior of concrete numerically.

The mechanical behavior of concrete may be investigated within quasi-static and high strain rate tests in terms of strength increase, strain rate sensitivity and deformation behavior. Split Hopkinson pressure bar (SHPB) is one of the most common test methods to investigate the mechanical behavior of concrete at high strain rates. However, when performing an SHPB test of concrete, there are some conditions and

limitations that must be taken into consideration to have valid test results. The most important test requirements and factors are data processing for getting correct stress-strain curves, prevention of premature failure of the test specimen, obtaining dynamic stress equilibrium and nearly constant strain rate, design limitations and sustainable test setup.

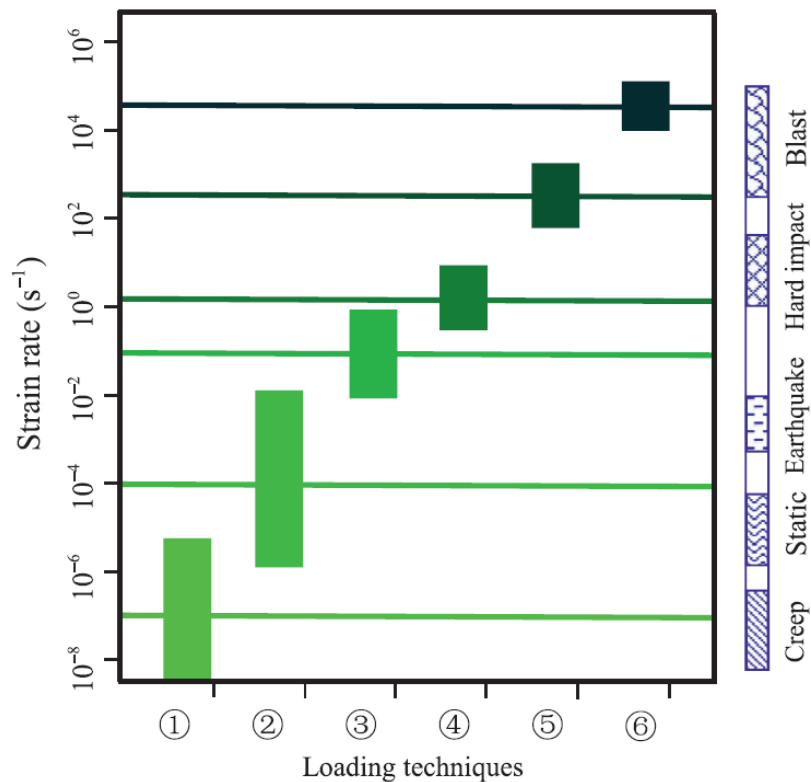
SHPB test setup can be used to examine the dynamic behavior of concrete in between 10^2 s^{-1} and 10^4 s^{-1} strain rates. Quasi-static tests, on the other hand, covers strain rates from 10^{-4} s^{-1} to 10^{-2} s^{-1} . High strain rate testing requires much more carefulness because of its complexity compared to quasi-static testing. Thus, testing of concrete using SHPB is not fully standardized yet due to the complications and limitations of the test methodology. The approach for testing methodology may differ from test setup or operator and this situation causes interpretation of test results differently. Thus, there are still needs for the improvement of SHPB test methodology.

Concrete and concrete-like materials undergo very low strains at failure. Therefore, reliable stress-strain measurements from the strain gages can be a difficult task. In addition, due to brittle nature of concrete and frictional effects at the bar interfaces, the specimen may be exposed to premature failure causing stress non-equilibrium at the bar interfaces and non-homogeneous stress distribution over the specimen. Another problem with the characterization of concrete is material model selection and determination of material model parameters. While it is still an ongoing debate whether or not concrete is a strain rate dependent or an independent material. Several material models have been developed for concrete and they have their own advantageous and disadvantageous. So, the selection and determination of suitable material model is a very important factor for the interpretation of the behavior of concrete and numerical modeling studies.

The aim of this study is to develop a testing and characterization methodology for dynamic mechanical characterization of concrete. This thesis focuses on improvements of SHPB test methodology with the utilization pulse shaper and piezo-electric quartz crystals. Integration with the experimental and numerical study, determination of material model parameters of concrete will be presented. Numerical analyses of SHPB tests will provide a better understanding of the dynamic behavior of concrete and by changing the specimen geometry will present the effect of specimen geometry.

1.2 Literature Review

There are many test techniques developed for achieving different strain rates from static to dynamic loading conditions. Lu et al. summarized these methods and type of loadings in Figure 1.1 and stated that one single device cannot cover the determination of strength of a material from low to high strain rate range. They illustrated that hydraulically driven machines are suitable for measuring strain rates ranging from 10^{-8} s^{-1} to 10^{-1} s^{-1} . Drop weight machines can provide strain rates in between 10^{-1} s^{-1} and 10^1 s^{-1} . Split Hopkinson pressure bar can be used for reaching strain rates ranging between 10^1 s^{-1} and 10^4 s^{-1} . For the blast loads, a one-stage light gas gun may be used to obtain strain rates ranging from 10^4 s^{-1} to 10^5 s^{-1} (Lu et al., 2017).



- ① is specialized-hydraulic machines, ② is a servo- hydraulic machines,
 ③ is a pneumatic- hydraulic machines, ④ is a drop weight machines,
 ⑤ is a split Hopkinson pressure bar, ⑥ is a one-stage light gas gun.

Figure 1.1. Loading techniques to achieve a variety of strain rate range at different loading conditions (Source: Lu et al., 2017)

For the dynamic mechanical characterization of the concrete, split Hopkinson pressure bar is widely used and successful test apparatus when testing of concrete in between 10^2 s^{-1} and 10^4 s^{-1} strain rates. The history of the Hopkinson pressure bar goes

back up to a hundred years ago. The very first Hopkinson bar experimental technique was developed as a result of investigation of stress wave propagation in iron wires by (J. Hopkinson and B. Hopkinson, 1901). Due to experimental limitations at these times, it was challenging to measure pressure and stress wave propagation in the work done by John Hopkinson.

In pursuit of John Hopkinson's study, his son Bertram Hopkinson developed a new experimental procedure to measure pressure-time relation by the high-speed impact or explosion of bullets in 1914. B. Hopkinson used pendulums to record the movements of cylindrical rods as shown in Figure 1.2. The apparatus shown in the figure includes a long steel rod, a short steel billet, a ballistic pendulum and a bullet or gun cotton to produce the impact pressure. Compressive pulse was generated by impacting one end of the long steel rod. A compressive pulse was traveled through the far end of rod and traversed through the short steel billet which was held by an only thin layer of grease. The generated wave would be reflected back from at the far end of the rod as a tensile wave. Since grease would not hold the billet anymore due to the tensile wave, the billet would fly off with a momentum. Then, this momentum was measured by the ballistic pendulum. The momentum of the billet may be determined by measuring maximum displacement, period, and mass of the ballistic pendulum. By changing flying steel billet dimensions, the maximum pressure and total duration could be determined. However, pressure-time measurements with this method was not so accurate or did not reflect instantaneous and maximum pressure due to the lack of measurement techniques at that time (B. Hopkinson, 1914)

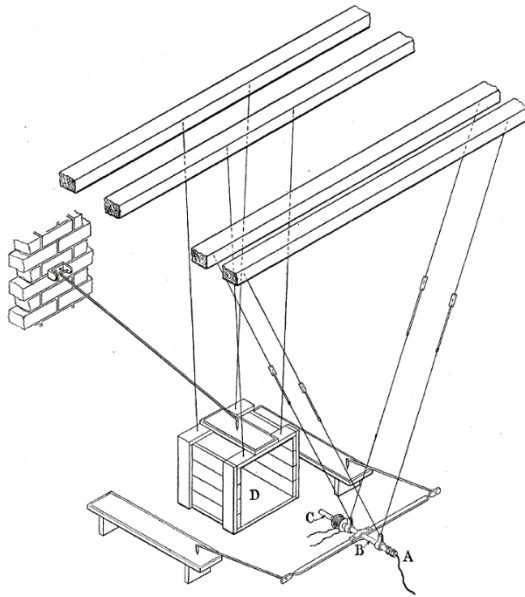


Figure 1.2. Apparatus developed by Bertram Hopkinson for the measurement of pressure (Source: B. Hopkinson, 1914)

Landon and Quinney continued the developments of Hopkinson pressure bar. They studied the effect of conical firing end and the length of the bar on the propagation of pressure wave. Also, the effect of diameter of the bar and distance of the charge from the end of the bar on the mean pressure were investigated (Landon and Quinney, 1923).

Bancroft solved frequency equation of Pochhammer and Love for the velocities of longitudinal waves in cylindrical bars. He expressed the velocity of longitudinal waves in cylindrical bars as the velocity at infinite wavelength times a function of two variables. These variables are Poisson's ratio and the ratio of the diameter of the bar to the wavelength (Bancroft, 1941).

Davies developed an electrical measurement method to express the relationship between pressure and time for Hopkinson Pressure bar experiments. Davies used a parallel plate and cylindrical condensers to measure radial and longitudinal displacements and by using oscillograph he was able to observe the variation of applied pressure as a function of time. He also described three limitations for original Hopkinson bar method and his new electrical measurement method. These limitations were described as; i) Stress that can be measured from the bar is limited by elastic wave propagation in the bar, ii) Pressure pulse is propagated without distortion and iii) Pressure pulse is distributed uniformly over the cross-sectional area of the bar (Davies, 1948).

Kolsky designed a new method based on the work done by Davies for the the improvements in measurement system (Kolsky, 1949). Originally, there was one cylindrical bar in Hopkinson pressure bar apparatus, Kolsky added a second cylindrical bar and sandwiched the specimen between these two bars as shown in Figure 1.3. After Kolsky's development, Hopkinson pressure bar named as Split Hopkinson pressure bar or Kolsky bar. The method developed by Kolsky was able to measure stress-strain behavior of materials with a sensitivity of 20 microseconds at high strain rates. A parallel-plate condenser microphone was used for the purpose of measuring pressure on the specimen. Also, a cylindrical condenser microphone was placed around the bar between detonator and the specimen to measure amplitude of the pressure pulse and the deformation of the specimen.

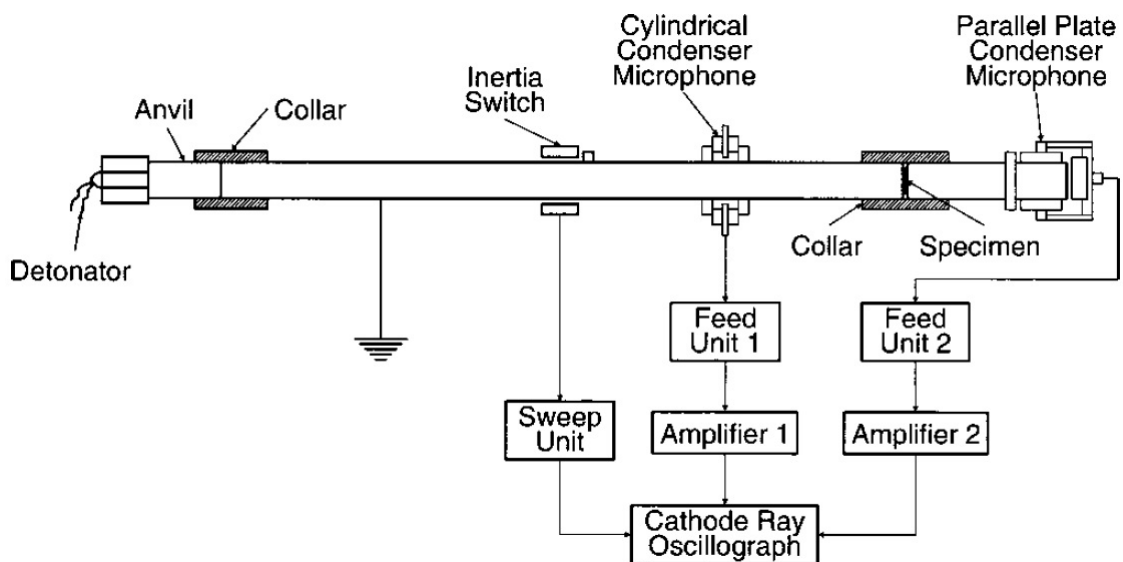


Figure 1.3. Kolsky's apparatus
(Source: Gama et al., 2004)

Krafft et al. tested iron and mild steel samples to see the effect of both static and dynamic compression as well as temperature effect in compression testing. They used Hopkinson bar to perform dynamic loading tests. His contribution to Hopkinson bar was mounting strain gages instead of condensers. Two strain gages were placed on diametrically opposite sides of bars and connected through Wheatstone bridge. He used cathode ray oscilloscope in order to visualize strain-time signals from strain gages. Then strain gage application became a standardized method to measure stress waves in the Hopkinson bar testing. Also, Kolsky and previous researchers used explosive detonator

for the impact pulse, however, Krafft et al. used a gun to fire loading bar for the benefit of repeatability (Krafft et al., 1954).

For the dynamic characterization of materials, the most valid version of the split Hopkinson pressure bar design made by (Lindholm, 1964). Although there have been improvements, advanced techniques and modified versions of Hopkinson bar for more accurate measurements, Lindholm's modification became a template of currently used SHPB apparatus. He was able to measure continuous strain-time histories of the incident, reflected and transmitted pulses. His technique allowed for recording of stress, strain, and strain rate as a function of time in the order of microseconds. Moreover, Lindholm used his method to study strain rate sensitivity of lead, aluminum, and copper. The schematic of the test setup used by Lindholm is shown in Figure 1.4.

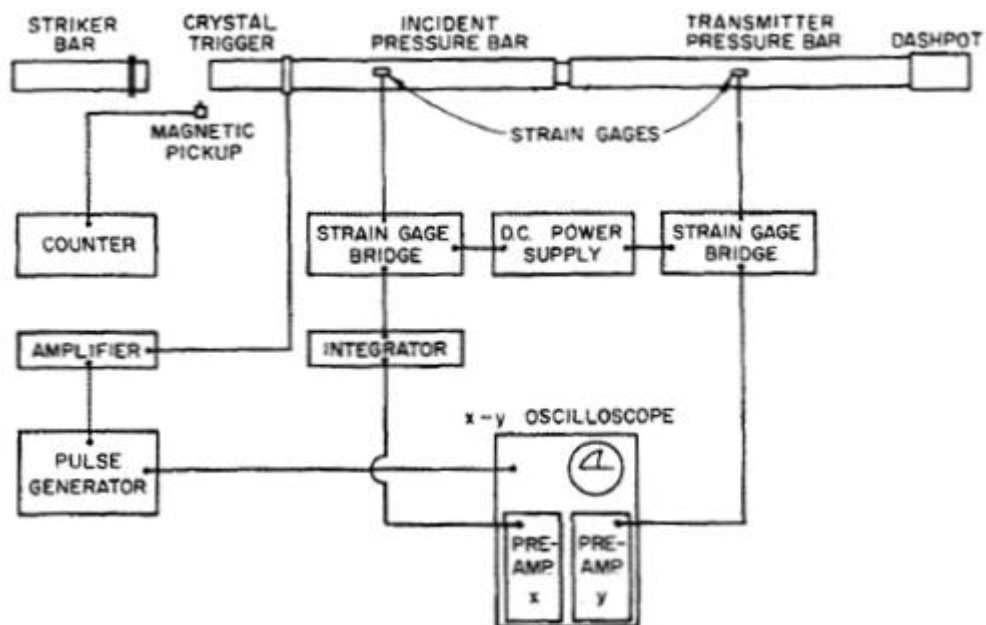


Figure 1.4. Lindholm's SHPB test setup
(Source: Lindholm, 1964)

Initially, split Hopkinson bar technique was designed for compression tests only. Researchers expanded split Hopkinson bar technique for tension and torsion tests. The logic behind of tension and torsion test are similar to compression test methodology yet it has different loading conditions and specimen gripping techniques. Further developments occurred in data acquisition systems, data reduction and analysis, dispersion correction, pressure bar design and specimen geometry. The history and recent modification of the Hopkinson bar and its applications were discussed in ASM Handbook (Gray, 2000). Even though there have been a large number of improvements

and modifications on original Hopkinson bar system, still there is no standardized methodology due to dispersion effects on data analysis in a finite diameter bar, frictional effects and inertial effects. Thus, there is always a need for further improvements on the SHPB for the validity and accuracy of the test results and better measurements and analysis.

To understand the dynamic mechanical behavior of concrete, researchers have conducted many studies over the years. Several experimental and numerical methods have been developed for better understanding of behavior of concrete at high strain rates. Split Hopkinson pressure bar is a commonly used test technique for achieving high strain rates in dynamic compressive testing of concrete.

Goldsmith et al. performed Hopkinson bar tests to investigate dynamic behavior of concrete. They also did tensile and compressive static tests on concrete. $\frac{3}{4}$ in. in diameter and 24 in. in length, specimens were used. He concluded that dynamic Young's modulus of concrete is greater than the static value (Goldsmith et al., 1966).

Malvern et al. used split Hopkinson pressure bar for dynamic compression tests of concrete specimens having failure strain rates ranging from 10 s^{-1} to 100 s^{-1} . In this study, four types of concrete with a different type of aggregates were tested. They plotted the maximum stress versus average strain rate at maximum stress and compared the results of these four types of concrete. It was stated that SHPB is a useful technique to determine strength of concrete at moderate strain rates (Malvern et al., 1985).

Ross performed direct tension, direct compression and split cylinder tests using split Hopkinson Bar. It was found that strain rate sensitivity for direct tension tests was two to four times greater than compression tests for the same strain rates. While he concluded that compressive tests fulfill the stress uniformity along the specimen length, dynamic modulus from SHPB is not reliable due to elastic deformation during the rise time of loading (A. Ross, 1989).

Tedesco and Ross made direct compression and split tensile tests for concrete specimens (Tedesco and Ross, 1998). In this study, the effects of strain rate on concrete were investigated. Quasi-static tests were conducted between 10^{-7} s^{-1} and 10^{-5} s^{-1} while dynamic rates were between 10^{-1} s^{-1} and 10^3 s^{-1} . Critical strain rates where the material showed significant strength increase were pointed out by doing statistical analysis. These critical strain rates were found as 2 s^{-1} for tension test and 60 s^{-1} for compression test. Also, strain rate dependent constitutive equations were developed.

Bischoff and Perry reviewed the compressive behavior of concrete at high strain rates. All the literature about the uniaxial compressive behavior of plain concrete at high strain rate was analyzed. In Figure 1.5, the strain rate influence in the compressive strength increase of concrete using the data available in the literature is presented. A variety of loading methods for a different range of strain rates are presented. A clear logarithmic strength increase in compressive strength of plain concrete is observed for impacts having high strain rates. Also, it was concluded that strength increase did not only depend on tensile micro cracking but also a transient state of uniaxial stress to uniaxial strain. Critical maximum strain at maximum stress, elastic modulus, secant modulus and Poisson's ratio increase was observed with increasing strain rate in the majority of studies (Bischoff and Perry, 1991).

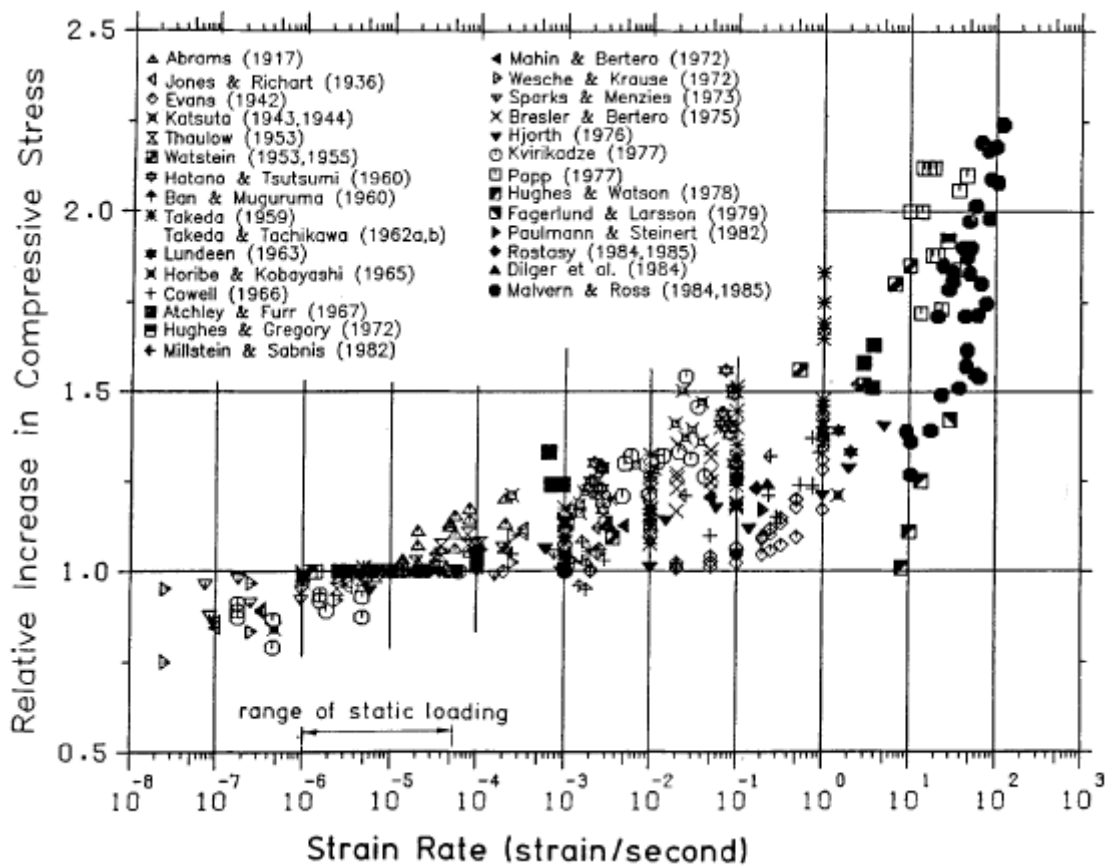


Figure 1.5. Strain rate effect on the compressive strength of concrete.
(Source: Bischoff and Perry, 1991)

Piezoelectric quartz crystals as a force transducer have been used by researchers to measure axial force occurred in pressure bars. Piezoelectricity can be explained as using quartz crystals to convert mechanical energy into electricity or vice-versa. Quartz crystals exhibit piezoelectric behavior. When a mechanical stress applied to a quartz

crystal, it turns mechanical stress into electrical potential. Thus, usage of quartz crystals thanks to its piezoelectricity has many applications in the industry. It was reported that quartz crystal force transducers are three orders of magnitude more precise than strain gages with electrical resistors (W. Chen et al., 2000).

Utilization of a quartz crystal as a force transducer was developed first by (Karnes and Ripperger, 1966) in order to evaluate stress at the back face of the cold worked aluminum specimen by mounting quartz crystal between the rear face of the specimen and the pressure bar. They found out that using a quartz crystal for measuring stress for strains below two percent and strain rates below 4000 s^{-1} gives meaningful and valid results. The implementation of quartz crystal together with the strain gages was presented by (Wasley et al., 1969) to obtain more accurate stress-strain and strain rate results for brittle solids or low strength materials. They reported that combination of both strain gage and quartz crystal transducers in split Hopkinson bar is more reliable and accurate than the conventional split Hopkinson bar technique. Togami et al. used quartz crystal and accelerometer in split Hopkinson bar to investigate accelerometers performance for the large amplitude pulses. They used a disk at the end of the aluminum bar and quartz crystal was placed this aluminum bar-disk interface. Stress pulse was measured using both quartz crystal at the aluminum bar-disk interface and an accelerometer at the end of the disk. They compared the acceleration data from both quartz and accelerometer. It was concluded that quartz gage and accelerometer data showed a very good agreement (Togami et al., 1996).

Piezoelectric quartz crystal force transducer insertion to the conventional split Hopkinson pressure bars was introduced by (W. Chen et al., 2000). As seen in Figure 1.6, a circular X-cut piezoelectric quartz crystal is embedded in the middle of the aluminum transmitter bar. The mechanical impedances of the quartz crystal and the aluminum bar are very close to each other which satisfy the one-dimensional wave propagation through the transmitter bar is not affected by the quartz crystal. The mechanical behavior of soft materials with the pulse-shaped incident wave was investigated. It was concluded that quartz crystal insertion in the middle of transmitter bar provides directly measuring low amplitude force profile of a soft specimen while pulse shaping ensures the stress equilibrium and homogeneous deformation through the specimen.

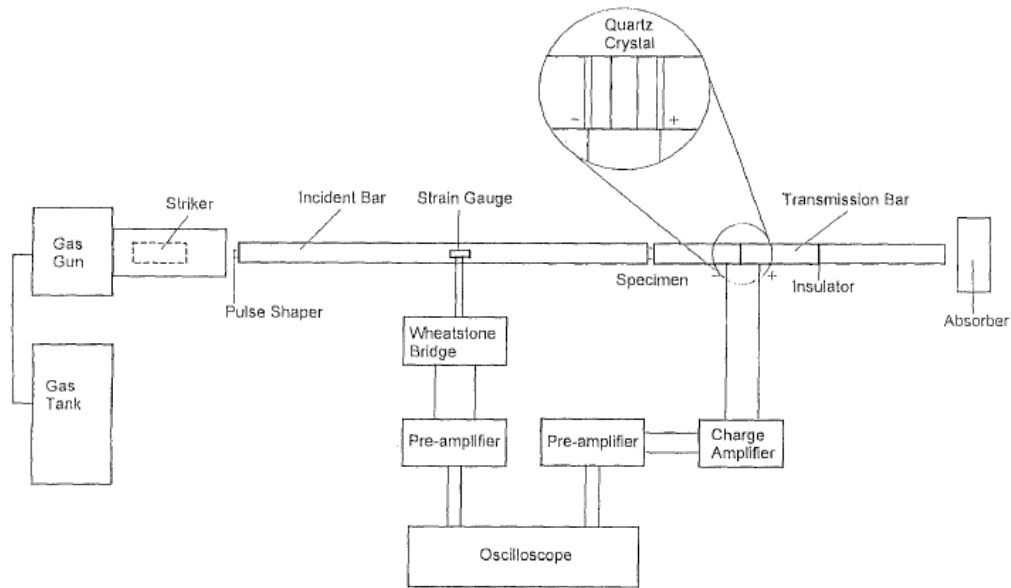


Figure 1.6. Schematic of modified split Hopkinson pressure bar with the implementation of quartz crystals (Source: W. Chen et al., 2000)

Quartz crystal force transducers were used to determine dynamic stress equilibrium of soft materials which produces low amplitude transmitted signals (Song and W. Chen, 2004). Two piezoelectric quartz crystals were installed on both front and back end surfaces of the specimen to directly measure axial forces on the specimen. In this way, they determined the dynamic stress equilibrium in the specimen by changing the loading rate and thickness of the specimen.

Song and Chen also introduced a split Hopkinson pressure bar method for characterizing soft materials using piezoelectric quartz crystals and pulse shaper (Song and W. Chen, 2005). The major problems encountered at high strain rate testing of soft materials were described. The associated challenges were stated as follows; the validity of stress-strain curve, weak transmitted signal, achieving dynamic stress equilibrium and obtaining constant strain rate with the deformation of the specimen. As it was explained in detail by Song and Chen, conventional SHPB was modified with the pulse shaper and piezoelectric quartz crystal to overcome aforementioned problems when testing of soft materials.

Quartz crystals were also used in hydraulically driven loading frame and SHPB for mechanical testing of epoxy syntactic foam for the investigation of rate effects at intermediate strain rates. Highly accurate force histories were directly measured using quartz crystal force transducers and stress equilibrium was checked using the data provided by quartz crystals (Song et al. 2007).

A quartz crystal force transducer was inserted specimen-transmitter bar interface in split Hopkinson pressure bar test setup to measure force histories of highly particle-filled composite specimens. The implementation of this method provided to measure loading force directly and without noise for such a brittle material having low wave impedance and low strength (Zhou et al., 2012).

Another application of quartz crystal in a compression split Hopkinson pressure bar was made by (Tasdemirci et al., 2012). They used X-cut piezoelectric quartz crystal on between transmitter bar and specimen interface to measure force history of Teflon foam at high strain rates. They also compared the stress results acquired by quartz crystal and strain gages. Stress-strain comparison of strain gage data and quartz crystal transmitted signal showed very similar results.

Pulse Shaping is another modification in addition to the conventional SHPB test setup. This technique was described in detail by Subhash and Ravichandran for testing of ceramics using split Hopkinson pressure bar. The steep rise in the rectangular pulse may cause a non-uniform strain rate condition for the elastic deformation of the ceramic specimen because of the differences between the slopes of stress-strain response and the applied loading rate. It is stated that instead of using a rectangular shaped incident pulse, an incident pulse matching with the slope of the elastic response of the ceramic is more suitable. Therefore, using a ramp pulse is more advantageous for not only matching the slopes of incident pulse and the stress-strain response but also attaining constant strain rate throughout the elastic deformation of the ceramic specimen. A ramp pulse can be obtained by placing a thin ductile material disk on the impact end of the incident bar. As the striker impacts the pulse shaper, plastic deformation of pulse shaper creates a ramp pulse in the incident bar. The shape of the incident ramp pulse can be changed by using different material as a pulse shaper or changing the velocity and length of the striker bar (Subhash and Ravichandran, 2000).

Frew et al. presented a pulse shaping techniques for testing of brittle materials using SHPB. They modified conventional SHPB setup by placing a pulse shaper in order to ensure that specimen is in dynamic stress equilibrium and has nearly constant strain rate. They used a thin disk copper on the impact surface of the incident bar to shape incident pulse. They found that pulse shaping is necessary to get dynamic stress equilibrium and nearly constant strain rate for testing of brittle samples (Frew et al., 2002).

Chen et al. used pulse shaped split Hopkinson pressure bar to determine mechanical behavior of paste, mortar, and concrete under dynamic test conditions. Their study showed that using pulse shaper can eliminate high frequency in the loading wave and also convert the rectangular wave into a triangular wave. Furthermore, by increasing the rising time of incident wave, uniform stress and strain in the specimen could be achieved (Chen et al., 2013).

Two pulse shaping techniques were introduced to create a shaped incident pulse for testing of concrete using SHPB. These techniques are changing the striker bar design and using a pulse shaper having different geometry. Chen et al. examined the effects of a striker in different length and tapered shape as well as the copper pulse shaper in different diameter, thickness, and annular shape. They concluded that small diameter copper pulse shaper has the best pulse shaping effect in terms of dispersion elimination, increasing rise time and achieving constant strain rate during deformation. The tapered striker provided extended rise time, elimination of oscillations and constant strain rate as compared to long striker (Chen et al., 2016).

Shemirani et al. studied about choosing proper pulse shapers for testing of concrete specimens in dynamic test conditions both numerically and experimentally. They emphasized using a pulse shaper is essential for testing of concrete specimens to validate SHPB tests. A comparatively small diameter and thick pulse shaper are suggested as a suitable pulse shaper for testing concrete specimens. It was stated that for various strain rates the striker bar velocity is proportional to the cross-sectional area and the thickness of pulse shaper (Shemirani et al., 2016).

In literature, many researchers studied about dynamic strength increase of concrete in compression. Rossi mentioned that high strength concretes are less sensitive to strain rate effects than the normal strength concrete since the free water existence in high strength concrete is very low. In addition to this, it was reported that the fractures turn more transgranular which means crack passes through both the grains and the matrix with increasing strain rate. While in low strain rates, the cracks occur in the weakest area where cracks pass through matrix and matrix-grain interfaces (Rossi, 1991a). The free water effect was examined on the mechanical behavior of concrete in the range of low and high strain rates (Rossi, 1991b). In low strain rates, water vapor diffusion is more dominant in the mechanism of the mechanical behavior of concrete while Stefan effect is more effective in the high strain rates.

Rossi et al. investigated the free water effect on the dynamic behavior of concrete. They prepared wet and dry micro concrete specimens to be tested on both static and dynamic tensile tests. Dynamic tests were carried out using Hopkinson bar by changing loading rate and static tests were performed using uniaxial tensile test apparatus. It was found that wet micro concrete is more rate dependent than dry micro concrete due to the stress concentration near to the notch in the wet specimen. Also, it was observed that the strength of wet concrete was very low as compared to dry micro concrete. In addition, a numerical analysis was performed to figure out stress concentration effect of wet micro concrete specimens. It was found that stress concentration is an important factor for increasing tensile stress. So it was concluded that dynamic to static strength ratio is 1.14 for dry micro concrete while 4.1 for the wet micro concrete. Although dynamic Young's modulus was found out lower than static modulus for wet specimens, dynamic and static Young's modulus were calculated as nearly the same for the dry specimens (Rossi et al., 1992).

Li and Meng studied the dynamic strength increase of concrete-like materials using SHPB test setup. They argued that the dynamic strength increase of concrete like materials caused by hydrostatic stress dependency and lateral inertia confinement in SHPB tests above 10^2 s^{-1} strain rate. They pointed out that the dynamic strength enhancement of concrete like materials was misinterpreted as strain rate effect which may be resulting in overpredicting the dynamic strength of concrete (Li and Meng, 2003).

Numerical analysis using mesoscale concrete model and homogeneous macroscale model were carried out together to investigate the compressive behavior of concrete like materials at high strain rates (Zhou and Hao, 2008). In macroscale model, the material was assumed as homogeneous and isotropic. Whereas, the mesoscale model includes aggregate, mortar matrix and the interfacial transition zone (ITZ). A strain rate insensitive model was used to observe the inertial effects. Influence of Inertial confinement on the dynamic strength of homogeneous and mesoscale concrete model as a function of strain rate is presented in Figure 1.7. It was noted that inertia effect becomes more important when the strain rate is beyond 200 s^{-1} . Also, the inertial effect in the mesoscale model was greater than the homogeneous model.

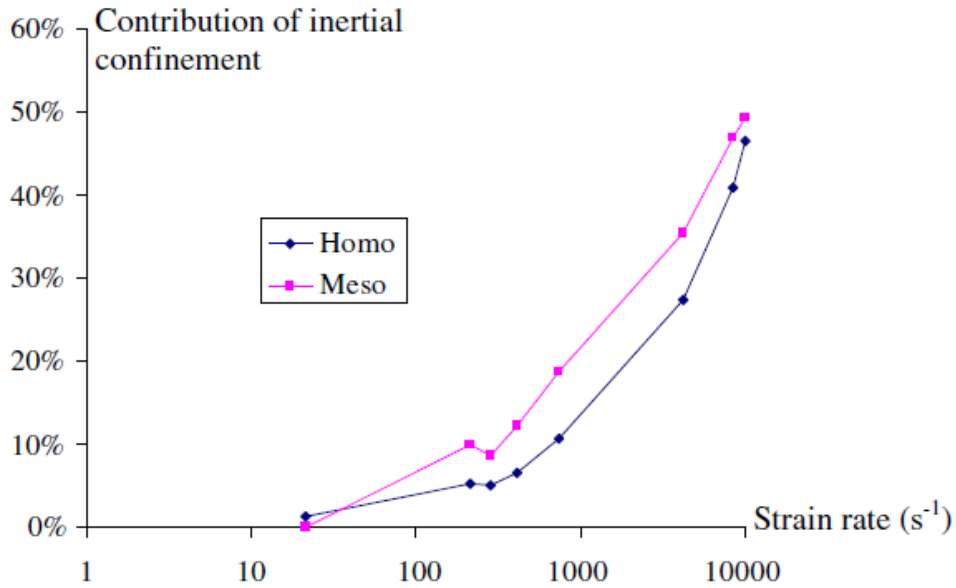


Figure 1.7. Influence of inertial confinement for homogeneous and mesoscale concrete model (Source: Zhou and Hao, 2008)

Mu et al. claimed that lateral inertia effect and the friction effect between loading apparatus and the loaded specimen were generally accepted reasons for the dynamic strength increase of concrete. However, they emphasized that there were still uncertainties how these factors affect the strain dependency and what is the main mechanisms of these factors. Thus, numerical analyses of drop hammer tests were carried out with different height to diameter ratio specimens. They concluded that in low strain range, lateral inertia effect was very limited while friction effects were dominant for the strength increase. As the strain rate increased in the high strain rate tests, inertial effects became prepotent, causing lateral confinement with increasing strain rate (Mu et al., 2012).

Hao and Hao investigated the effects of aggregates and interfacial transition zone (ITZ) between aggregates and mortar in concrete. They modeled mesoscale concrete to investigate the effect of aggregates volume on the compressive strength of concrete at high strain rates (Y. Hao and Hao, 2011).

Hao et al. studied the effect of end friction confinement, lateral inertia confinement and specimen length to diameter ratios using SHPB setup both numerically and experimentally (Y. Hao et al., 2013).

Hao et al. conducted a series of experimental test to verify the effect of aggregates and confinement caused by lateral inertia and end friction at the impact

loading conditions (Y. Hao et al., 2013). The proposed dynamic increase factors (DIF) and the reasons behind the dynamic strength increase of concrete were verified using both experimental and numerical results (Y. Hao et al., 2013; Y. Hao et al., 2013b; Y. Hao and Hao, 2011). It was found that from the three abovementioned studies, concrete strength increase at high strain rates stemmed from aggregates, interfacial transition zone (ITZ), end frictional confinement effect and the lateral inertia confinement.

There are several constitutive material models which were developed to evaluate dynamic response of concrete at impact loads. Although these material models have some advantages and disadvantages, one of the most widely used and accurate material model for testing of concrete-like materials was proposed by (Holmquist et al., 1993) named as Holmquist-Johnson-Cook (HJC) material model for concrete. It is one of the most widely used material models for concrete at high strain rates. This model provides a good agreement between simplicity and accuracy for computational work. HJC concrete material model includes large strain, high strain rates, and high pressures to define the compressive behavior of concrete at impact loads.

HJC material model was also used to determine the material model parameters of brick and mortar due to the similarity between these materials and concrete. The strength, pressure and damage behavior of brick and mortar were presented comparing with the experimental test data (Meyer, 2011).

Chen et al. performed dynamic splitting tensile tests which are a common way of tensile testing of concrete using SHPB. Different arc loading angles and impact velocities were implemented to observe failure pattern and local stress distribution in the concrete specimen. A numerical model of the dynamic splitting tensile test was constituted using LS-DYNA and HJC (MAT_111) material model. It was reported in this study, numerical model captured the stress distribution and crack propagation in the specimen and provided good consistency with experimental data (Chen et al., 2017).

HJC material model was also used for simulation of high strength or high-performance concrete structures. Tai studied the ultra-high strength concrete targets under high-velocity impact condition by changing impact velocity and steel fiber contribution. Finite element code LS-DYNA was used to model reactive powder ultra-high strength concrete target with the implementation of HJC material model. The dynamic response of concrete under high pressures and high strain rates was revealed by showing the cracking behavior, penetration progression and contact force readings at various impact velocities (Tai, 2009). Khoogar investigated the penetration of an ogive-

shaped steel projectile impacting on a semi-infinite concrete target. Numerical simulations were modeled using LS-DYNA where HJC material model was used for the concrete specimen. The results from the numerical analyses were coupled with analytical model and experimental test results. The penetration depth of a projectile into concrete targets was evaluated for different impact velocity and it was found that simulation results were good agreement with analytical and experimental results (Khoogar et al., 2013). Another research about steel projectile penetration into a concrete target was done by Johnson et al. In this study, an ogive-nose steel projectile having a velocity of 315 m/s impacted a concrete target. Radial stresses and penetration depth was evaluated using finite element analysis and compared with the experimental results. The concrete target modeled with HJC concrete material model showed crack and damage behavior as well as presented a good agreement with the experimental results (Johnson et al., 1998).

Shemirani et al modeled SHPB tests using Johnson Holmquist Cook material model for the concrete specimen. After completion of SHPB simulations, they found that stress-strain curves of experimental and numerical tests provided similar results with each other (Shemirani et al., 2016).

A mesoscale composite reinforcement concrete which consists of mortar, randomly distributed aggregates, and reinforcements was modeled using finite element method. HJC material model was used to simulate reinforcement concrete due to its compatibility with the dynamic behavior of concrete structures subjected to large strains, high strain rate, and high pressures. The material model parameters and experimental test data of reinforcement concrete were taken from literature. It was concluded that mesoscale model of reinforcement concrete where aggregates and reinforcements were modeled separately from mortar has great influence on penetration resistance, ballistic trajectories, and penetration process according to the penetration simulations (Zhang et al., 2018).

There have been several studies conducted about the specimen size and geometry as well as insert geometry used in dynamic compression testing of materials in split Hopkinson pressure bar. Especially, some researchers focused on the effect of specimen size and insert geometry on the stress concentrations. Indentation of the bar by a hard and brittle specimen due the impact loading was investigated by (W. Chen, 1995). Chen stated that while testing of ceramic materials some precautions must be taken to prevent violating SHPB assumptions. Indentation of end surfaces of the bars

may break these assumptions by creating stress concentrations and violating the parallelism and flatness of the bar-specimen surfaces. Therefore, Chen suggested two solutions to overcome this problem. First one was placing insert geometry and the second one was using dog-bone shaped specimen. Various specimen and insert geometries proposed by Chen are presented in Figure 1.8. He concluded using specimen whose diameter is less than the bar diameter may be inappropriate due to the indentations in the bars causing stress concentrations. Using impedance matched cylindrical tungsten carbide inserts and the diameter matched conical alumina inserts were reduced the stress concentrations in the specimen similarly. However, dog-bone shaped specimen provided best results in terms of minimizing stress concentrations. Also, it was determined that specimen diameter is an important factor to determine strain rate in the specimen with given incident pulse but decreasing the specimen diameter beyond the critical limit might cause violating uniaxial stress state.

The effect of slenderness ratio and tubular geometry of concrete-like materials on dynamic increase factor (DIF) was investigated numerically by Li et al. When the slenderness ratio which is the length of a specimen divided by the diameter of the specimen is between 0.3 and 1.0, the variation of DIF and strain rate can be considered as unimportant. It was also determined the radial stress distribution in the tubular specimen was lower than the solid specimen resulting in smaller radial confinement in a tubular specimen. According to test results, using tubular specimens smaller DIF values were obtained compared to solid specimens at the same strain rate (Li et al., 2009).

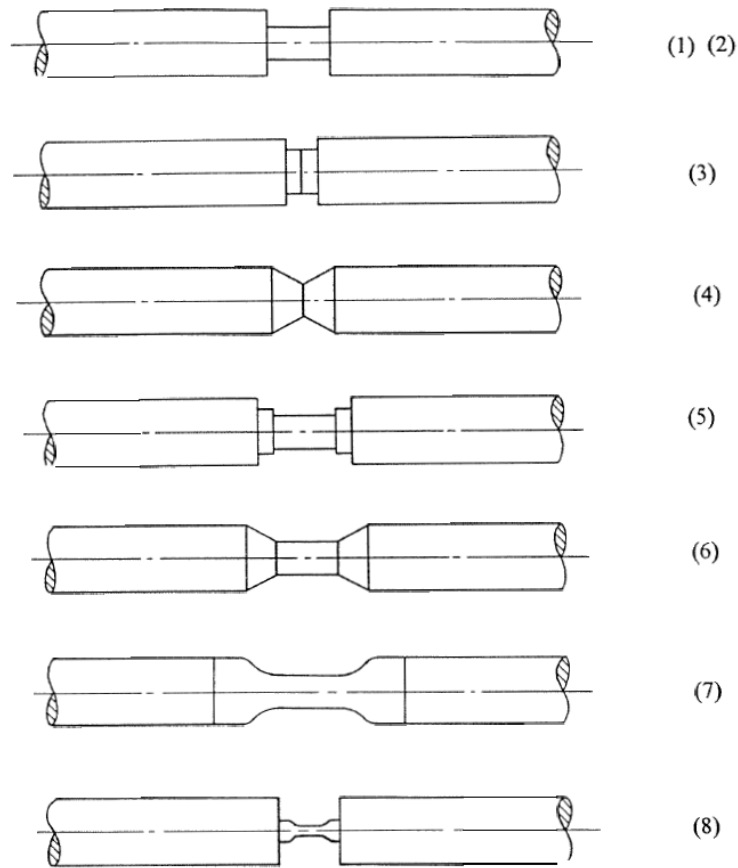


Figure 1.8. Various cases of specimen and insert geometries 1) Metallic specimen without inserts, (2) Ceramic specimen without inserts, (3) Cylindrical WC inserts only, (4) Conical Al_2O_3 inserts only, (5) Ceramic specimen with cylindrical WC inserts, (6) Ceramic specimen with conical Al_2O_3 inserts, (7) Dog-bone specimen with matching diameters, (8) Dog-bone specimen with non-matching diameters.

(Source: W. Chen, 1995)

The commercial finite element code LS-DYNA was used to simulate wave propagation and dispersion effect in Hopkinson bar test by (Ramírez and Rubio-Gonzalez, 2006). It was observed that square pulse yielded more oscillations than the trapezoidal pulse. In addition, when the rise time of the incident pulse was increased oscillations on this pulse decreased. Dispersion effects, on the other hand, becomes more severe when the projectile diameter was greater than the bar diameters. It was suggested in this study, a plastically deformable copper pad can be used in impact face of the incident bar to increase the rise time and lengthen the stress wave which are very important for testing of brittle materials.

Since it is important to prevent stress concentrations during an SHPB experiment, researchers conducted new insert designs to obtain valid results from dynamic mechanical test of low strain to failure materials. Sunny et al. used conical

insert and dog-bone shaped specimen in addition to conventional SHPB setup with a cylindrical insert to investigate dynamic behavior of Zr-based bulk metallic glass (Sunny et al., 2009).

The effect of specimen size and shape on the compressive strength of self-consolidating concrete was investigated by (Dehestani et al., 2014). They carried out compression tests on self-consolidating cube and cylinder specimen with different mixture proportions. Researchers found out the effect of specimen size became more important when the slenderness ratio was decreased. Based on the results they obtained, a relation between specimen geometry and the compressive strength of self-consolidating concrete was constituted.

Y. Hao et al. figured out that lateral inertia confinement effect depends on both specimen size and strain rate for concrete, especially strain rate above 200 s^{-1} (Y. Hao et al., 2010). Accordingly, as the specimen size increased the inertial effects would become more apparent.

1.3 Scope of the Study

This thesis focuses on the dynamic mechanical behavior and the characterization methodology of concrete. A brief introduction about concrete material and its history were proposed as an introduction. A literature review which covers testing of split Hopkinson pressure bar and its developments, mechanical behavior of concrete, usage of pulse shaping and quartz crystal force transducers, and numerical studies about concrete is presented in the first chapter.

Experimental and numerical studies were carried out together in this study. First, experimental tests were performed and then the results were compared with the numerical results. The second chapter started with the explanation of manufacturing and preparation of concrete test specimens. Then quasi-static and high strain rate testing methodologies are explained respectively. The experimental setup was explained in detail with the unique improvements in the methodology. Pulse shaping technique and implementation of piezoelectric quartz crystals to the conventional SHPB test apparatus were described. Also, SHPB theory and one-dimensional wave propagation in bars are explained. The data processing to obtain stress-strain calculations are formulated. Following this, quasi-static and high strain rate experimental test results of concrete

specimens are presented. Dynamic mechanical characterization study proceeded with the material model explanation and the determination of its parameters. Holmquist-Johnson-Cook (HJC) computational constitutive material model was selected to characterize dynamic behavior of concrete.

Numerical simulations were performed in LS-DYNA software. ANSYS and Ls-PrePost programs were used as a preprocessor in the modeling study. The validation of experimental test results are presented. In addition, the effect of specimen geometry on the dynamic stress equilibrium is discussed.

The thesis is concluded with the conclusions chapter. The findings and inferences are presented in conclusion. Suggestions for future works are also presented.

CHAPTER 2

EXPERIMENTAL METHODOLOGY

2.1 Introduction

In dynamic mechanical characterization of concrete, certain testing standards and procedures have to be followed to determine material model parameters of concrete. Experimental methodology chapter is divided into three main sections. Preparation of concrete mixture and test specimens are described in the first section. Next, quasi-static testing methodology is described with the detailed information of testing processes, specimen preparation for the tests and stress-strain data acquisition. In the last section, high strain rate testing methodology is divided into two parts. First, split Hopkinson pressure bar apparatus in the Dynamic Test and Modelling Laboratory in IZTECH is described. Afterwards, split Hopkinson pressure bar theory is explained briefly within the scope of wave generation, data processing, limitations and requirements to obtain valid and accurate test results from an SHPB test.

2.2 Concrete Material

Concrete is a construction material that it can be classified as a ceramic composite material which is basically composed of four materials. These materials are water, cement, sand, and aggregates. There are also a variety of ingredients which makes concrete more complex structure like adding reinforcement material in to the mixture such as steel, glass or plastic fibers. In this study, four fundamental components were used to create a concrete mixture.

A mixture of water, cement, sand, and aggregates were mixed in a specific ratio. To obtain the required amount of test specimen, 130 liters concrete mixture was prepared. It is important to know the quantity and the ratio of the materials in the mixture because it is directly related to the material properties of concrete. In order to get desired properties, ACI standard, 211.1 was selected and followed (ACI Committee 211, 2002). The procedure to be followed for this standard is as follows: Choice of a

slump and maximum size of aggregate, estimation of mixing water and air, determination of water/cement ratio, calculation the amount of cement and selection of aggregate content. Slump value is a measure of the degree of consistency and an extent of workability and was selected as 150 mm to 175 mm. The maximum size of aggregate was selected as 4.75 mm according to the rule 1/10 ratio of aggregate to specimen diameter and properties of specimens. Then, mixing water and air content was determined considering the table which was provided by ACI 211.1 standard. Water to cement ratio was selected as 0.40 which is directly related to the strength of concrete. After determination w/c ratio, the amount of cement and aggregate were to be apparent.

After the concrete mixture was prepared, the mixture was poured into prismatic molds having dimensions 220x45x45 mm. Once prismatic concretes were extracted from molds test specimens were taken out using a wet cut drill. 39.50 mm diameter core drills were used to take out cylindrical test specimens having 39.50 mm in diameter and 45 mm in length. The front and back surfaces were subjected to a polishing process in order to ensure that specimen surface parallels to bar surfaces. Prismatic steel molds and the test specimen which was core drilled from prismatic concrete are shown in Figure 2.1.



Figure 2.1. Prismatic concrete mold and core-drilled cylindrical test specimen

2.3 Quasi-Static Testing

The testing procedure for the mechanical characterization of concrete started with the quasi-static compression tests in this study. Quasi-static tests were performed using 300 kN Shimadzu AG-X universal tension and compression test machine. Quasi-static tests were considered in the range from 10^{-4} s^{-1} to 10^{-2} s^{-1} strain rates for concrete. Thus, three different strain rate levels were selected in order to accomplish quasi-static

tests which are 10^{-4} s^{-1} , 10^{-3} s^{-1} , and 10^{-2} s^{-1} . The purposes of choosing different strain rates were to measure quasi-static compressive strength of concrete and determine the strain rate sensitivity in the low strain rate range. These strain rates were determined according to the ratio of the cross-head velocity and the specimen length (Equation 2.1). However, actual strain rate in the specimen was found from taking the derivative of strain data as function of time in the elastic region.

Due to the brittle nature of concrete, specimens may undergo premature failure or have different stress-strain behavior for the same strain rate. Therefore, three valid and accurate tests were taken from a series of tests at each strain rates. The stress and strain relation for compressive quasi-static tests is given in Equation 2.1 and Equation 2.2.

$$\sigma_s = \frac{P}{A_s} \quad (2.1)$$

$$\dot{\epsilon}_s = \frac{V_{cr}}{L_s} \quad (2.2)$$

where σ_s and A_s are stress and cross-sectional area of the specimen and P is the measured force from the machine load cell. $\dot{\epsilon}_s$ is the desired strain rate in the specimen, V_{cr} is the cross-head speed and L_s is the length of the specimen.

The test setup for quasi-static tests is shown in Figure 2.2. The concrete specimen was marked with gage markers and placed in between moving and fixed plates. The movement of gage markers was tracked by two video extensometers. A light source was used for lighting the specimen area.

During quasi-static tests, a high-speed video camera was used to investigate the damage progress on the specimen and to find the crack initiation and propagation in the specimen. The images were taken from the high-speed video camera recordings. These images are presented in the third chapter.

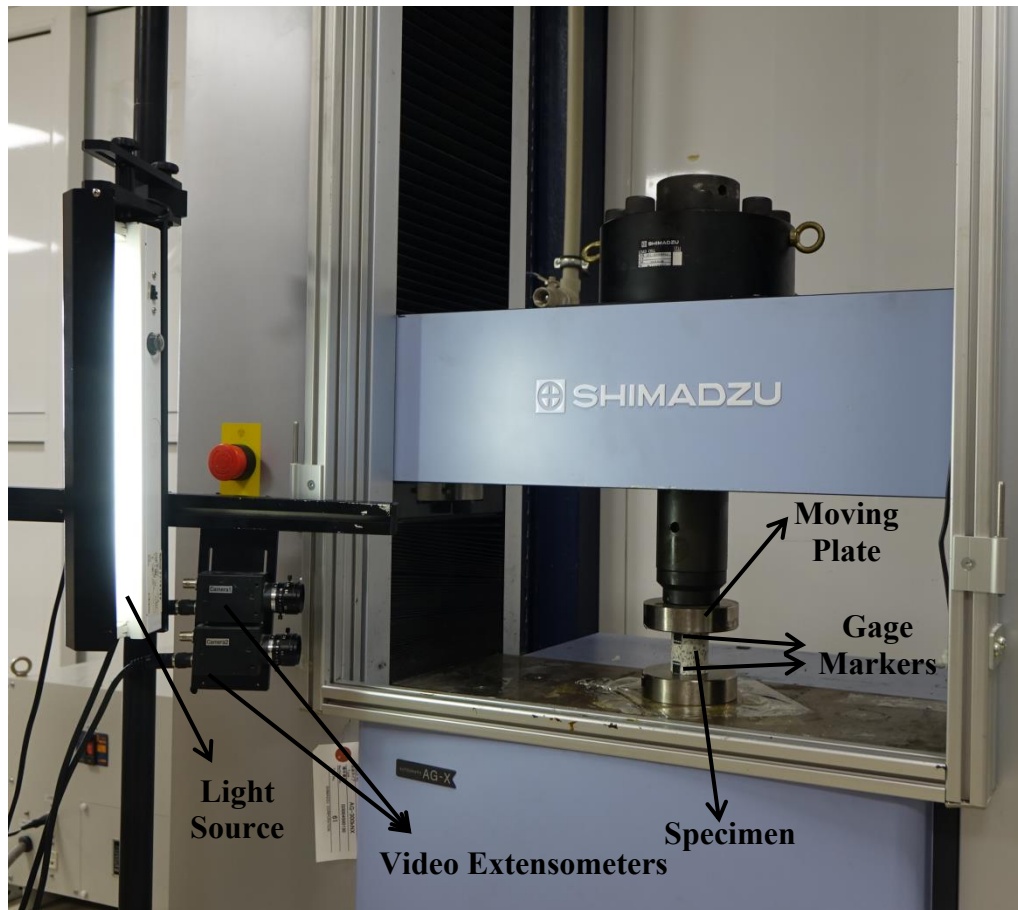


Figure 2.2. Quasi-static test setup

In order to achieve valid results, tests were performed with two different strain measurement methods. First method is measuring strain using video extensometer that two cameras specify the two markers in the specimen and measure the change in distance between these two markers. Longitudinal strain was calculated from the change between the two markers over the distance between markers.

The other method was insertion of strain gages directly to the specimen surfaces. Strain gages were connected to the oscilloscope and conditioner to get the signals as a voltage value. Using several strain gages in this method provided measuring longitudinal strain in the specimen even more accurately. In addition to vertical strain gages along with sample length, lateral strain gages were placed on the specimen surface. The ratio of the voltages read by lateral gages and vertical gages was calculated and Poisson's ratio of the concrete specimen was acquired. The illustration of strain gaged test specimen is shown in Figure 2.3.



Figure 2.3. Test specimen with strain gages

In order to find the tensile strength of concrete, split tensile tests were carried out. ASTM C 496 standard was followed during these tests (ASTM C496, 2011). 3 mm thick and 25 mm wide plywood supports were prepared and placed upper and lower contact surface of the samples. The dimension of test samples used in these tests was 39.50 mm in diameter and 25 mm in length. The loading rate was selected as 1 MPa/min in accordance with the standards and the tensile stress calculation was made using Equation 2.3.

$$T = \frac{2P}{\pi LD} \quad (2.3)$$

where T is the splitting tensile strength, P is the maximum applied load indicated by the test machine, L and D are the length and diameter of the test specimen respectively. Splitting tensile test image can be shown in Figure 2.4 where a cylindrical concrete specimen is positioned such that its longitudinal axis lies horizontally between the platens of a loading mechanism.

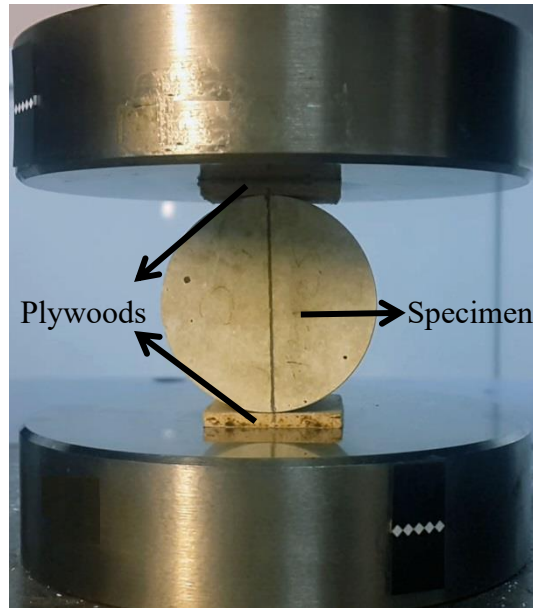


Figure 2.4. Split-tensile testing of a concrete

2.4 High Strain Rate Testing

It is known that the mechanical behavior of concrete under impact loadings differs from static loadings. So, the investigation of the dynamic mechanical behavior of concrete requires not only quasi-static or low strain rates but also high strain rate tests. Dynamic loads such as explosions, blasts, earthquakes, and ballistic loadings are often encountered in the use of concrete structures. Generally, strain rates between 10^1 s^{-1} and 10^4 s^{-1} cover aforementioned dynamic loads. Split Hopkinson Pressure Bar (SHPB) is one of the most widely used method for testing materials having strain rates ranging from 10^2 s^{-1} to 10^4 s^{-1} . SHPB test setup contains some limitations and assumptions in order to obtain valid results. However, testing a brittle material like concrete needs extra precaution when testing at high strain rates due to the accuracy of the measurements taken from an SHPB test. Since concrete undergoes small strain relative to its high compressive strength and due to its brittle nature, modifications to the traditional SHPB test setup must be applied. It is hoped that testing of concrete at high strain rates using the modifications and the methodology developed in this study would be a well-designed methodology covering in terms of pulse shaping, dispersion elimination, specimen design, friction and other limitations.

2.4.1 SHPB Apparatus

Split Hopkinson Pressure Bar apparatus basically consists of 3 main elements: These are bar components, loading mechanism, and data acquisition system. The schematic of the SHPB test setup within the modifications in this study is shown in Figure 2.5.

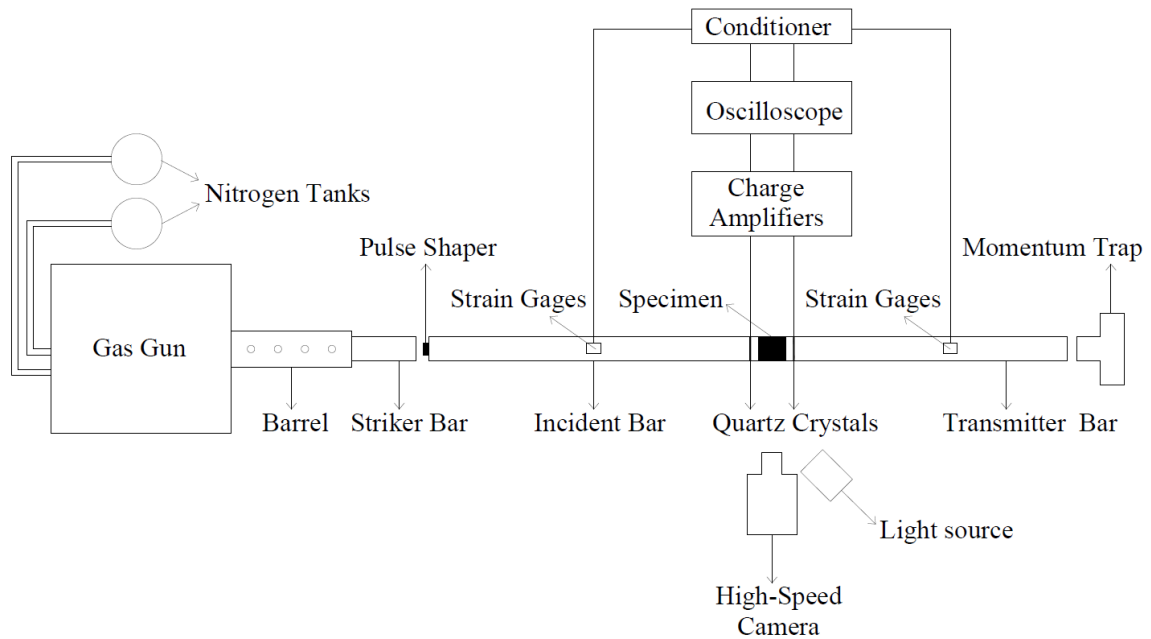


Figure 2.5. Schematic of SHPB bar

Bar components comprise three cylindrical bars; Striker bar (20 cm length), incident bar (199 cm length) and transmitter bar (155 cm length). All bars are made of the same material which is aluminum 7075-T6 and has the same diameter 40 mm. The bars move freely on their supports and must be perfectly aligned with the direction of the movement so that friction will be minimized. A momentum trap is placed at the end of the transmitter bar. It prevents to fly off the transmitter bar and stop it after impact. A momentum trap with absorber inside of it absorbs the axial impact energy of transmitter bar and prevents the repeated pulses. Physical properties of aluminum 7075-T6 bars are listed in Table 2.1.

Table 2.1. Physical properties of the 7075-T6 aluminum pressure bars

| <i>Physical Properties</i> | <i>Values</i> |
|----------------------------|------------------------|
| Density | 2810 kg/m ³ |
| Elastic Modulus | 71.7 GPa |
| Poisson's Ratio | 0.3 |

A gas gun system is used as a loading device since a gas gun provides a controllable, repeatable and safe test procedure for the impact. Two nitrogen tubes are used as the storage of compressed nitrogen gas. Then, nitrogen gas is sent through pipes and compressed in the gas tank by opening the valves of the gas gun. A rapid release of the gas will launch striker bar and striker bar moves through a long barrel which is attached to the gas gun. There are small gaps on this barrel so that striker bar can move on at a constant speed. The speed of striker bar is measured with laser optic measurement device with a two-point laser and it is controlled by the amount of gas which is stored in the gas tank.

Although there are several ways to measure strain, using strain gages is the most common method to measure strain in the split Hopkinson pressure bars. Two Vishay general-purpose 90⁰ tee rosette electrical resistance strain gages having with 2.11 Gage factor (*GF*) and 350-ohm resistance were symmetrically bonded using M-Bond 200 strain gage adhesive on the bar surface of both incident and transmitter bar. Wheatstone full bridge circuit was used as a strain gages circuit type. The strain gages on the incident and transmitter bar were positioned at the same distance from the specimen which is 77.5 cm. Usually, strain measurements on the strain gages are very small magnitudes (mili-strain) for brittle materials. Therefore, a signal amplifier is required to increase low voltage value to measure accurate strain values. Vishay A2 Signal Conditioner was used as an amplifier. Excitation voltage (V_{exc}) was applied through the bridge. After signal was amplified through the conditioner, an oscilloscope recorded the wave signals as a voltage value. The following Equation 2.4 is given for the conversion of voltage history to strain history of the wave signals which is received by mounted strain gages on the bars.

$$\varepsilon(t) = \frac{2V(t)}{V_{exc}GF K_{gain} (1 + \nu)} \quad (2.4)$$

The conditioner was set to have a gain value of 200 (K_{gain}) and 10 volt excitation voltage (V_{exc}). On the other hand, oscilloscope should have enough frequency to catch the very small duration of pulses produced on the bars. Thus, Tektronix MDO3024 Mixed Domain Oscilloscope which is capable of running at 200 MHz and 2.5 GS/s was used.

Dynamic force equilibrium at the specimen and bar interfaces should be achieved for the validation of SHPB experiments. Force values at the specimen ends are usually measured through strain gages in the conventional SHPB test setup. However, stress waves are exposed to some distortion and changes in amplitude through wave propagation. Also, it can be sometimes challenging to decide from where the waves should be separated and determine how long the waves should be shifted in time. Therefore, stress wave measurements at the strain gage location may not perfectly represents the stress wave at the specimen and bar interface. This may lead to misinterpretation of force values at the specimen-bar interfaces.

Another technique to measure force profiles of front and back faces of the specimen is using piezoelectric quartz crystals. It was stated that quartz crystal force transducers are two to three orders of magnitude more sensitive than strain gages (Song and W. Chen, 2005). In this study, dynamic force profiles of the specimen was detected with the insertion of circular X-cut quartz crystal at the specimen and bar interfaces. The quartz crystal diameter and thickness were selected from manufacturer Boston Piezo Optics which were 40.00 ± 0.1 mm in diameter and 0.254 ± 0.01 mm in thickness. Piezoelectric constant of quartz crystal was stated as 2.3×10^{-12} C/N by the manufacturer. Mechanical impedance of quartz crystal was also matched approximately with the aluminum bars where quartz crystal had 15.11×10^6 kg/m²s and aluminum bar had 14.19×10^6 kg/m²s resulting in the ratio of 1.06. Thus, one-dimensional stress wave propagation through the aluminum bars was provided with minimal disturbance. Quartz crystals were bonded in between an aluminum disc and impact end of the aluminum bars by using CircuitWorks CW2400 conductive epoxy. These aluminum discs provided bonding of quartz crystals and prevented indentation specimen into the pressure bars. Kistler 5010A charge amplifier was used to get a quartz crystal electrical signal and convert it as a voltage value so as to it can be read by oscilloscope as voltage. Quartz crystal installation in the specimen-bar interfaces is given in Figure 2.6.

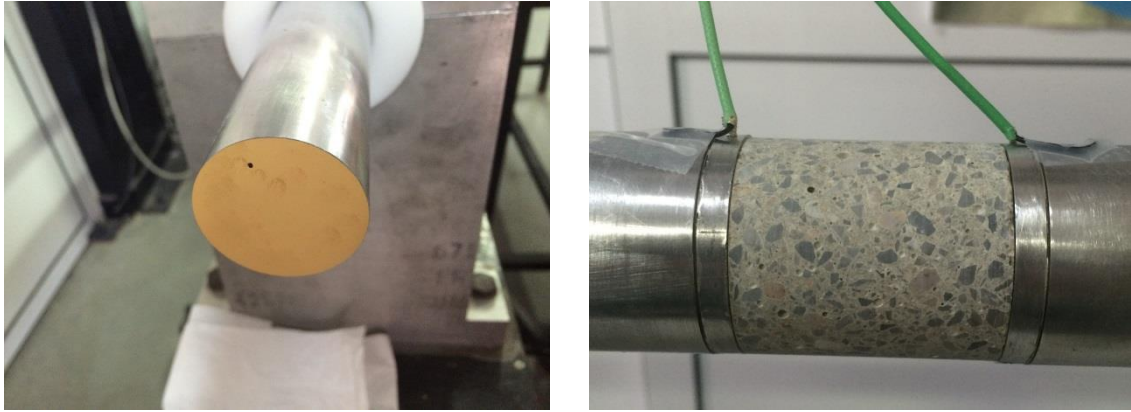


Figure 2.6. Piezo-electric quartz crystal bonded to the aluminum bar and the concrete specimen sandwiched between bars

A high-speed camera and a light source were used to record the deformation of test specimen in the SHPB tests. Fastcam SA1.1 high-speed camera capturing images at a maximum frame rate of 675000 fps and Dedolight Daylight 400D light source were used in video recording system. In Figure 2.7, video recording system and data acquisition system including conditioners and oscilloscope for strain gages and piezoelectric quartz crystals are presented.



Figure 2.7. Data acquisition and video recording system in the SHPB

The tests at high strain rates using SHPB were performed both with pulse shaper and without pulse shaper. Wave propagation through the bars is not only axial but also there is a radial acceleration due to the Poisson's effects. Although compressive wave moves in the axial direction and produces an axial stress, the acceleration in radial

direction produces inertia caused stress in the axial direction. Thus, radial inertia in the bars violates the one-dimensional wave assumption and causes two-dimensional wave propagations. This makes oscillations in the waves as a result of dispersion. Especially, as the wave propagates over distance and the bar diameter increases, pulses on the bars becomes more dispersive. Therefore, dispersion in the stress waves must be eliminated in order to obtain valid and accurate results. The dispersion can be eliminated either numerically or experimentally.

Pulse shaping is a method to achieve constant strain rate and dynamic force equilibrium through the specimen deformation by modifying incident pulse using pulse shaper. Using pulse shaper also eliminates or minimizes the dispersive behavior of wave propagation in cylindrical bars by fulfilling the one-dimensional wave propagation.

In this study, experimental pulse shaping technique was applied to split Hopkinson pressure bar setup as shown in Figure 2.8. Ethylene Propylene Diene Monomer (EPDM) rubber pulse shaper was used at the impact end of the incident bar. Circular pulse shaper having 3 mm thickness and 12.7 mm diameter was attached to the incident bar with a small amount of grease.

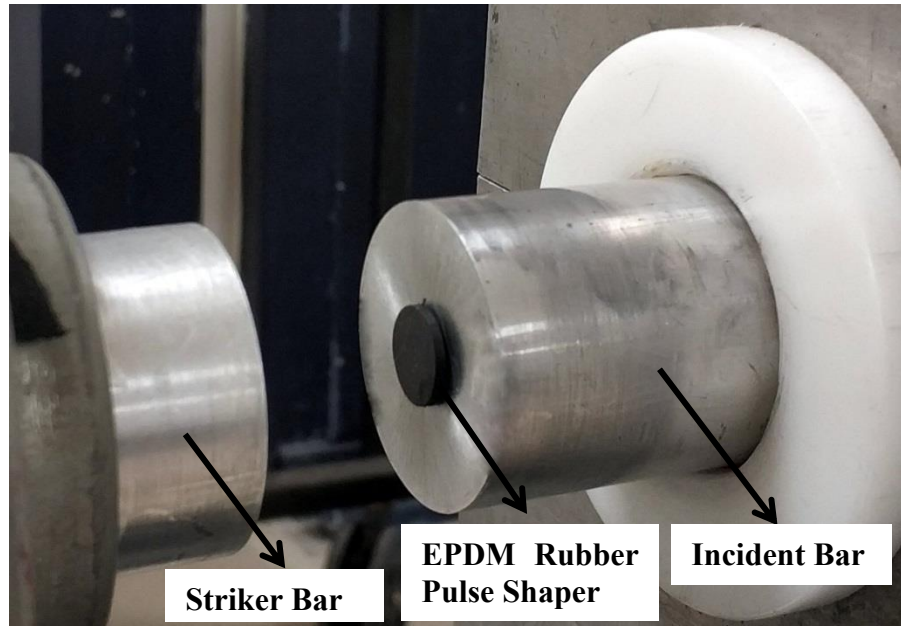


Figure 2.8. Pulse shaper insertion on the impact face of the incident bar

The split Hopkinson pressure bar test setup used in high strain rate testing of concrete specimen is presented in Figure 2.9. This setup was established in Dynamic Testing and Modelling Laboratory in IZTECH.



Figure 2.9. Split Hopkinson Pressure Bar test setup

2.4.2 SHPB Theory

Split Hopkinson Pressure Bar working principle is based on one-dimensional stress wave propagation in solids. The purpose of SHPB technique is to understand the the stress-strain behavior of materials at high strain rates. The specimen to be tested is sandwiched between incident and transmitter bars. The striker is launched by a gas gun with predetermined speed in the axial direction. After striker bar is traveled in the gun barrel, it impacts to the incident bar and creates an elastic compressive stress wave. This elastic compressive wave which is called as incident wave travels along the incident bar. The incident wave is recorded by the strain gage mounted on the incident bar and it is denoted as $\varepsilon_i(t)$. When the compressive incident wave reaches the specimen and incident bar interface, part of the wave is reflected back due to mechanical impedance mismatch between bars and specimen. This wave is called as a reflected wave $\varepsilon_r(t)$ which is a tensile and opposite sign of the incident wave. After some reverberations occur in the specimen due to the compressive wave, a part of the wave is transmitted to the transmitter bar. The strain gage in the transmitter bar measures transmitted pulse $\varepsilon_t(t)$ same sign with the incident wave. A typical SHPB test result of concrete is shown in Figure 2.10 as a voltage-time history.

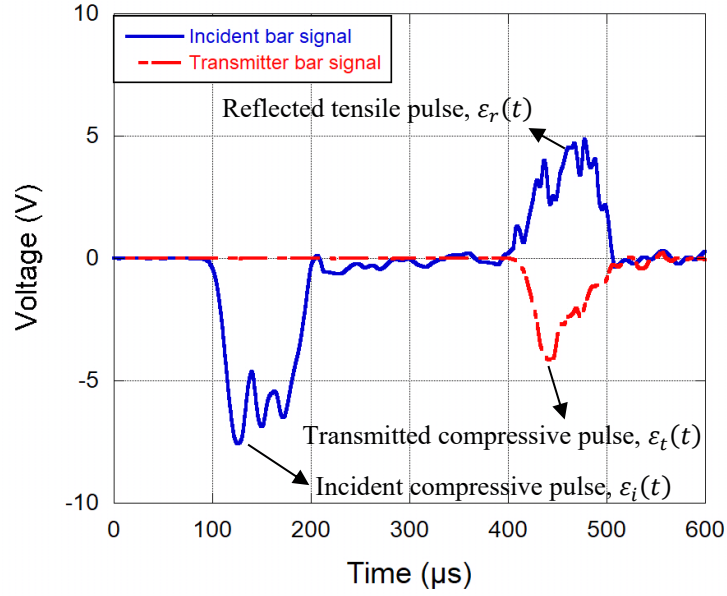


Figure 2.10. A typical voltage-time history of a SHPB test of concrete

When a perfect impact of two collinear bars carried out, the magnitude of the square shaped stress pulse is given as follows;

$$\sigma = \frac{V_1 \rho_1 C_0}{2} \quad (2.5)$$

where, σ is the magnitude of the stress pulse, V_1 is the impact velocity of the striker bar, C_0 is the wave velocity and ρ_1 is the density of the bar. The duration of the pulse depends on only the length of the striker bar and the wave velocity.

$$T = \frac{2l_1}{C_0} \quad (2.6)$$

The duration of the pulse is defined as T where l_1 is the length of the striker bar. It can be seen that the magnitude of the pulse is proportional to impact velocity. Also, physical properties of the striker bar affects both the magnitude of the pulse and its duration. However, a perfect square shaped pulse can not be attained due to the dispersive nature of the pressure bars. Dispersion in the longitudinal wave propagation in pressure bars takes place as a result of lateral inertia effects.

Stress-strain calculations for SHPB specimen is given by (Gray, 2000) in detail. Strain values of ε_i and ε_r are gathered the strain gage mounted on the incident bar while ε_t is measured from the gage on the transmitter bar. These values are read as voltage

values in the oscilloscope and need to be converted strain values analytically. Figure 2.11 presents good representation for the incident and transmitter bar interface with the specimen.

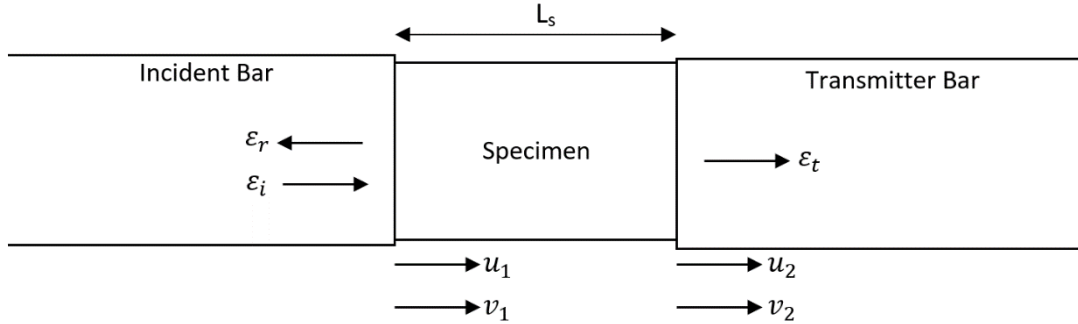


Figure 2.11. Schematic of the testing area of split Hopkinson pressure bar

The one-dimensional wave equation is given by Equation 2.7:

$$\frac{\partial^2 u}{\partial x^2} = \frac{1}{c_0^2} \frac{\partial^2 u}{\partial t^2} \quad (2.7)$$

where u is displacement, ε is strain, c_0 is longitudinal wave speed ($c_0 = \sqrt{E/\rho}$) of the bars and displacement takes place in x direction by time (t). The notation 1 is used to define incident bar specimen interface and notation 2 is for specimen transmitter bar interface. Equation 2.7 can be also written as:

$$u = f(x - c_0 t) + g(x + c_0 t) = u_i + u_r \quad (2.8)$$

The strain is defined by following formula:

$$\varepsilon = \frac{\partial u}{\partial x} = f' + g' \quad (2.9)$$

Differentiating Equation 2.8 with respect to time gives:

$$\dot{u}_1 = c_0(-f' + g') = c_0(-\varepsilon_i + \varepsilon_r) \quad (2.10)$$

Time derivative of the displacement on the transmitter bar gives:

$$\dot{u}_2 = c_0 \varepsilon_t \quad (2.11)$$

The strain rate in the specimen can be found as:

$$\dot{\varepsilon}_s = \frac{(\dot{u}_1 - \dot{u}_2)}{l_s} = \frac{c_0}{l_s} (-\varepsilon_i + \varepsilon_r + \varepsilon_t) \quad (2.12)$$

where l_s is the instantaneous specimen length, \dot{u}_1 and \dot{u}_2 are the particle velocities at the specimen bar interfaces. Incident bar force is given as:

$$F_1 = A_b E_b (\varepsilon_i + \varepsilon_r) \quad (2.13)$$

and transmitter bar force is:

$$F_2 = A_b E_b \varepsilon_t \quad (2.14)$$

where A_b and E_b are the cross-sectional area and Young's Modulus of the bars. In a valid SHPB test, it is assumed that specimen is in force equilibrium on both faces and the deformation of the specimen is uniform. With regard to these assumptions, simplification can be made by using dynamic force equilibrium ($F_1 = F_2$). This gives:

$$\varepsilon_t = \varepsilon_i + \varepsilon_r \quad (2.15)$$

Substituting Equation 2.15 into Equation 2.12 gives:

$$\dot{\varepsilon}_s = \frac{2c_0 \varepsilon_r}{l_s} \quad (2.16)$$

Calculation of stress in the specimen can be determined in three different ways. First one is called 1-wave analysis where the only transmitted wave is used to calculate the stress in the specimen. 1-wave stress can be determined as:

$$\sigma(t) = \frac{A_b E_b \varepsilon_t}{A_s} \quad (2.17)$$

where A_s is the instantaneous cross-sectional area of the specimen.

If both incident and reflected waves are used to determine stress in the specimen, this analysis is termed as 2-wave analysis which is given as:

$$\sigma(t) = \frac{A_b E_b (\varepsilon_i + \varepsilon_r)}{A_s} \quad (2.18)$$

Third stress analysis is known as 3-wave analysis which can be determined from the average of summation of all three waves. Simply, 3-wave stress can be found as dividing average of the total force $((F_1 + F_2)/2)$ by the cross-sectional area of the specimen.

$$\sigma(t) = \frac{A_b E_b (\varepsilon_i + \varepsilon_r + \varepsilon_t)}{2A_s} = \frac{(F_1 + F_2)}{2A_s} \quad (2.19)$$

Since instantaneous specimen length and cross-sectional area cannot be directly determined from SHPB test, engineering stress and engineering strain calculation for the specimen as a function of time is formulated through 1-wave, 2-wave and 3-wave stress in the Equation (2.20-2.22) respectively and strain formulation is given in Equation 2.23:

$$\sigma_{s1}(t) = \frac{A_b E_b \varepsilon_t(t)}{A_{s0}} \quad (2.20)$$

$$\sigma_{s2}(t) = \frac{A_b E_b (\varepsilon_i(t) + \varepsilon_r(t))}{A_{s0}} \quad (2.21)$$

$$\sigma_{s3}(t) = \frac{A_b E_b (\varepsilon_i(t) + \varepsilon_r(t) + \varepsilon_t(t))}{2A_{s0}} \quad (2.22)$$

$$\varepsilon_s(t) = \frac{C_0}{l_0} \int_0^t (-\varepsilon_i(t) + \varepsilon_r(t) + \varepsilon_t(t)) dt \quad (2.23)$$

where l_0 and A_{s0} instantaneous length and cross-sectional area of the specimen respectively.

There are some requirements and limitations to be satisfied in a valid SHPB test in order to make use of Equation (2.7-2.23) and achieve correct, consistent and reliable data for calculating the stress-strain behavior of brittle materials. These assumptions and design considerations are given by (Gama et al., 2004b) for ceramics and hard materials.

The First assumption is that stress equilibrium should be satisfied during deformation of the specimen. Choosing sufficiently longer incident wavelength can provide enough wave reflections to pass through the specimen. In this way, uniaxial and uniform state of stress is preserved with sufficient wave reflections and dynamic stress equilibrium is conserved before failure strength of the specimen. The dynamic stress equilibrium parameter can be found as using following equation:

$$R(t) = \left| \frac{\Delta\sigma(t)}{\sigma_m(t)} \right| = \left| \frac{\sigma_1 - \sigma_2}{(\sigma_1 + \sigma_2)/2} \right| = \left| \frac{F_1 - F_2}{F_1 + F_2/2} \right| \quad (2.24)$$

where, $R(t)$ is the dynamic stress equilibrium parameter, $\Delta\sigma(t)$ indicates the stress or force difference in between specimen end surfaces, and $\sigma_m(t)$ is the mean stress of these stresses at the specimen end surfaces. According to Ravichandran and Subhash, a stress difference of 5% at the end surfaces of the specimen with respect to mean stress is assumed to be practical to determine stress equilibrium in a ceramic specimen (Subhash and Ravichandran, 2000).

The second assumption emphasizes that the incident and transmitter bar remain elastic and the specimen-bar interfaces must be flat and parallel during the entire time of the experiment. Providing high strength bar material with controlling the impact speed of striker bar this assumption can be satisfied. However, a brittle specimen which has high strength might indent to the bar interfaces. The indentation into the bars produces stress concentrations to the specimen end faces which violate the uniaxial and uniform stress state assumption. Stress concentrations can create microcracking in the specimen

and premature failure can happen due to the microcracking. The aforementioned problem can be solved by placing inserts between specimen and bars.

The third assumption supposes that incident, reflected and transmitted waves experience minimal dispersion as they travel along the bars. If this condition is satisfied strain gage signals does not alter by time as they reach bar specimen interface. Thus, the true measurement of the response of specimen can be accomplished.

The last assumption states that first compressive incident wave is responsible for the failure and strain accumulation in the specimen. Since there are several wave reflections on the incident bar, unless specimen does not fracture in the first compressive wave other waves cause multiple loading on the specimen. Therefore, it is important to use of first incident compressive wave when the determination of stress-strain behavior of the specimen.

CHAPTER 3

EXPERIMENTAL RESULTS AND CHARACTERIZATION

3.1 Introduction

To determine material model parameters and strain rate sensitivity of the material itself both quasi-static and high strain rate tests were performed. For this purpose, three different strain rates for quasi-static tests and two different striker velocities producing equal incident pulse amplitude for the tests without pulse shaper and with pulse shaper were aimed. Stress-strain curves of each test were calculated accordingly. Strain rate and stress equilibrium histories for the dynamic test are presented. One-wave, two-wave, and three-wave stress-strain analysis and piezo-strain gage force histories were compared to each other. Based on the results, Johnson-Holmquist-Cook material model parameters for concrete were determined.

3.2 Experimental Results

Quasi-static and high strain rate test results are presented in this section. Using these results most of the material model constants were obtained and compressive dynamic mechanical behavior of concrete was constituted. The improvements used in the testing methodology and data analysis were discussed. For the quasi-static tests, five specimens were tested at three different strain rates which are 10^{-4} , 10^{-3} , and 10^{-2} s^{-1} respectively. Splitting tensile tests were also performed to determine tensile strength of the concrete material. A crosshead speed of the test machine was determined the corresponding strain rate; 0.0045 mm/s for 10^{-4} s^{-1} strain rate, 0.045 mm/s for 10^{-3} s^{-1} strain rate, and 0.45 mm/s for 10^{-2} s^{-1} strain rate were selected as crosshead speed. Two gage markers were used to record displacement in the first two specimens while electrical resistance strain gages were used in the third specimen. Since strain gages are more sensitive than video extensometers for reading strain data and video extensometers could not record horizontal and vertical strains at the same time, Poisson's ratios were determined using strain gages which were attached to the specimen.

First, quasi-static axial compression tests were completed at 10^{-4} s^{-1} strain rate. Compressive stress-strain curves for the tests recorded by video extensometers are presented in Figure 3.1 and Figure 3.2. It was found that failure stress and strain are 60 MPa and 0.003 respectively for both tests which are almost identical to each other. The duration of tests at 10^{-4} s^{-1} strain rate took 150 seconds approximately.

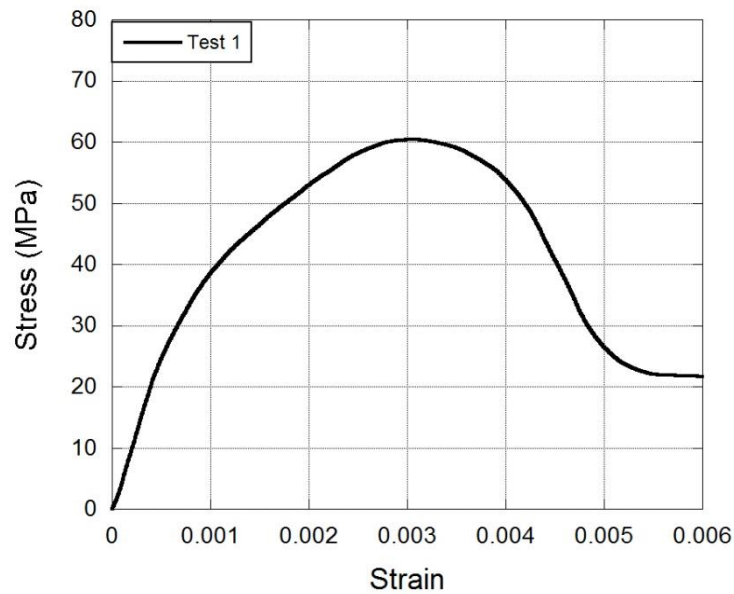


Figure 3.1. Test 1 stress-strain curve at 10^{-4} s^{-1} strain rate

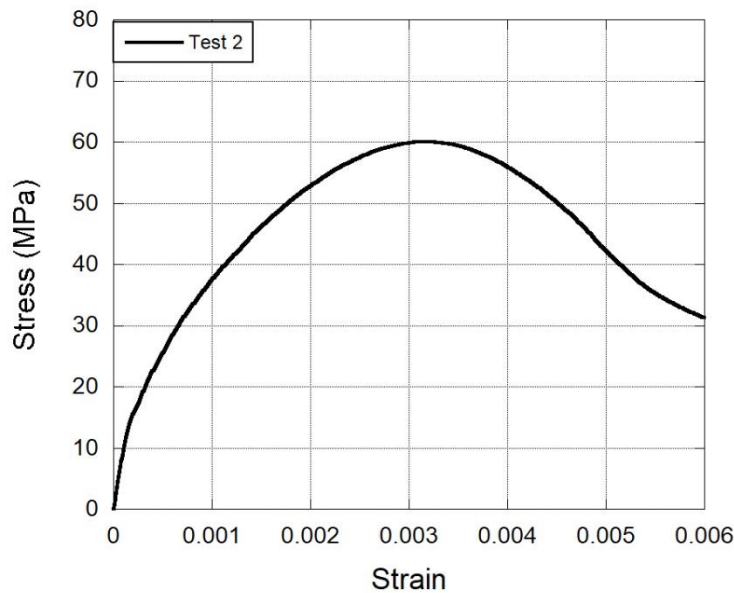


Figure 3.2. Test 2 stress-strain curve at 10^{-4} s^{-1} strain rate

Then, for the determination of actual strain rate and Poisson's ratio of the specimen, the test was carried out with the strain gages mounted on the specimen. Figure 3.3 shows the result of specimen with strain gage that failure stress was slightly increased to 62 MPa and strain was increased to 0.0035. Since strain gages were mounted on the surface of the specimen, they fell down due to failure and could not record post failure signals. Therefore, after peak stress and strain, strain gages could not read the signals furthermore. Poisson's ratio was also calculated as 0.21 by using vertical and horizontal strain gage recordings. At some point where the material plastically deforms Poisson's ratio increased dramatically due to the plastic deformation. Thus, Poisson's ratios were determined using only in the elastic limit of the material which the ratio has constant value in strain.

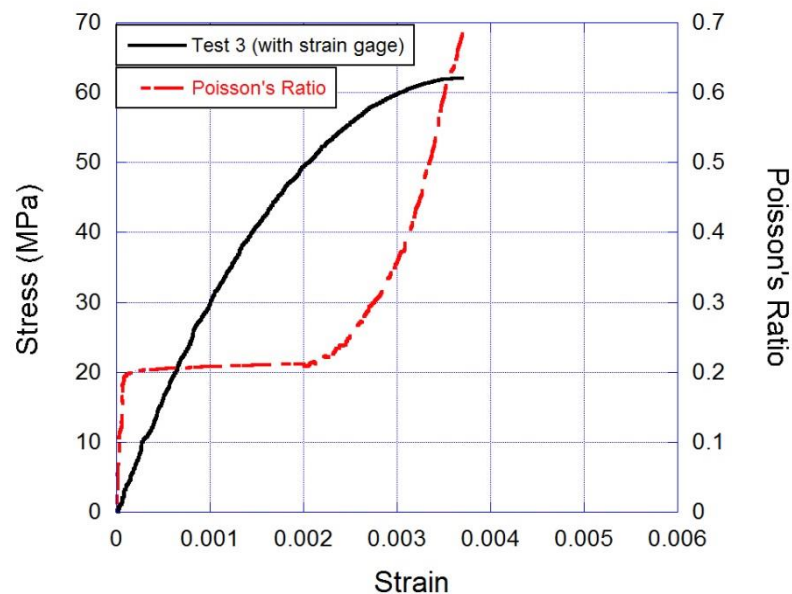


Figure 3.3. Test 3 stress-strain and Poisson's ratio 10^{-4} s^{-1} strain rate

According to the time-strain curve fit in Figure 3.4, the slope of the strain was found as $3.55 \times 10^{-5} \text{ s}^{-1}$ which is the actual strain rate in the specimen and calculated using strain gage data. Stress-strain comparison of the three 10^{-4} s^{-1} strain rate tests is shown in Figure 3.5. The results show a good agreement with each other until the peak stress-strain values. After failure of the test specimen, post peak behavior changes from test to test as expected.

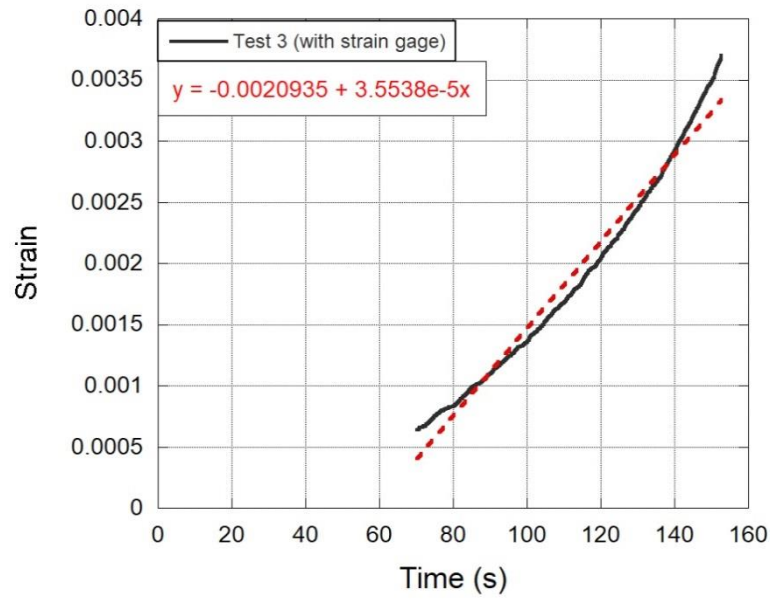


Figure 3.4. Test 3 actual strain rate fit at 0.0045 mm/s cross head speed

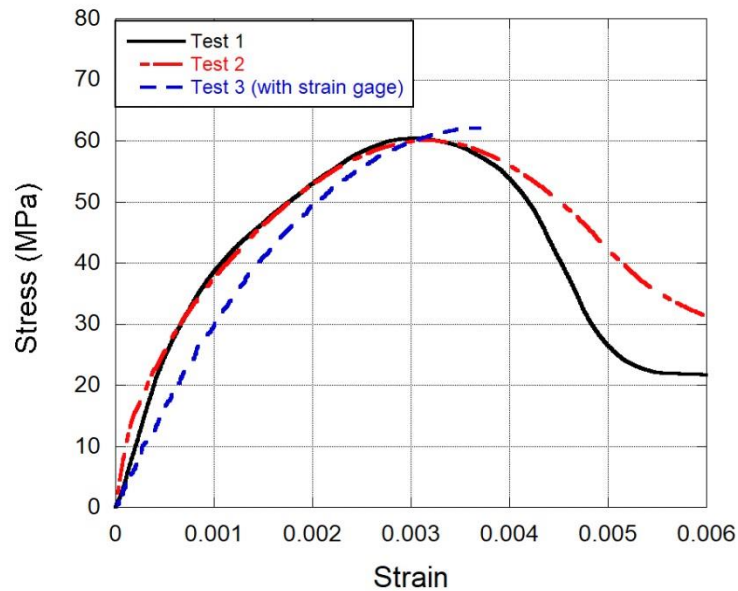


Figure 3.5. Stress-strain comparison at 10^{-4} s^{-1} strain rate

Next, three tests at 10^{-3} s^{-1} strain rate and having 0.045 mm/s cross head speed were performed. Video extensometer was used displacement recordings for the first two tests. Figure 3.6 and Figure 3.7 show that the compressive stress-strain curves of the two tests where strains were recorded by video extensometers. Test 1 in Figure 3.6 has 63 MPa failure stress and 0.0035 failure strain. The stress-strain results of test 2 is presented in Figure 3.7. Results showed that 65 MPa failure stress and 0.0037 failure strain in the test 2.

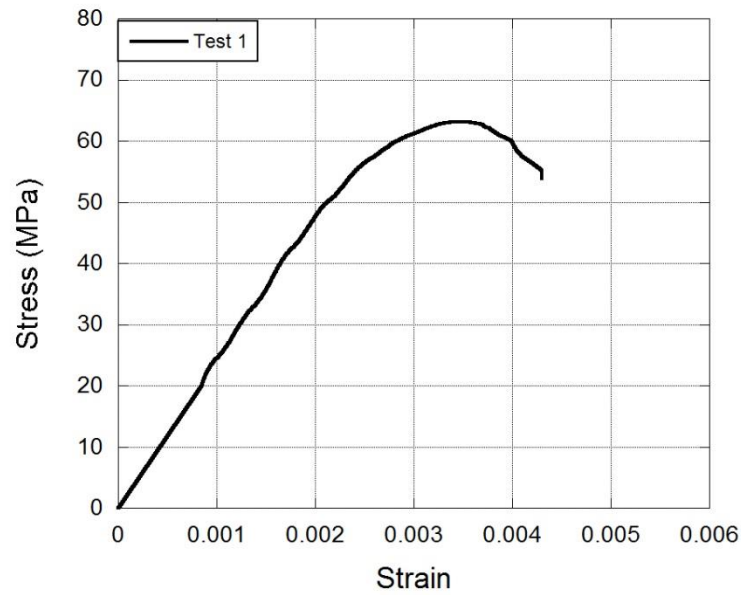


Figure 3.6. Test 1 stress-strain curve for 10^{-3} s^{-1} strain rate

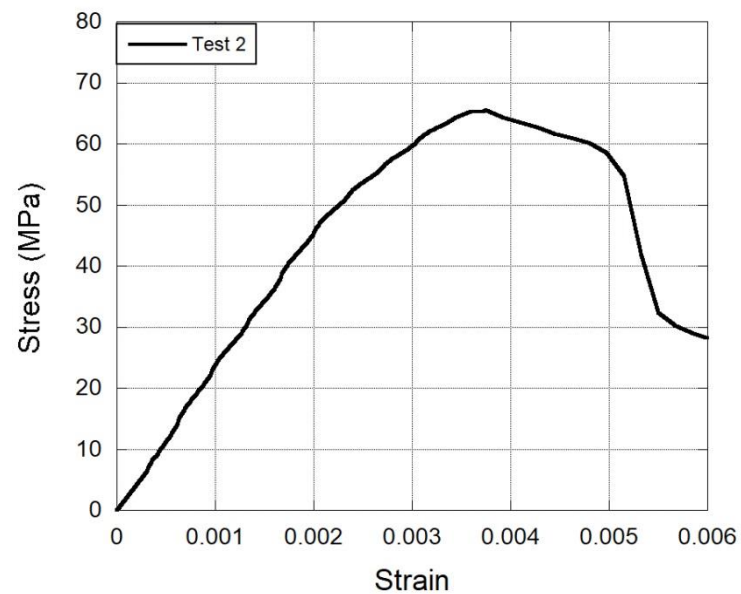


Figure 3.7. Test 2 stress-strain curve for 10^{-3} s^{-1} strain rate

Figure 3.8 shows that the test with strain gage has 64 MPa maximum stress and 0.0034 strain in failure. These results showed that failure stress and strain were increased overall in 10^{-3} s^{-1} strain rate as compared to 10^{-4} s^{-1} strain rate tests. Poisson's ratio, on the other hand, was found as close as with 10^{-4} s^{-1} strain rate test.

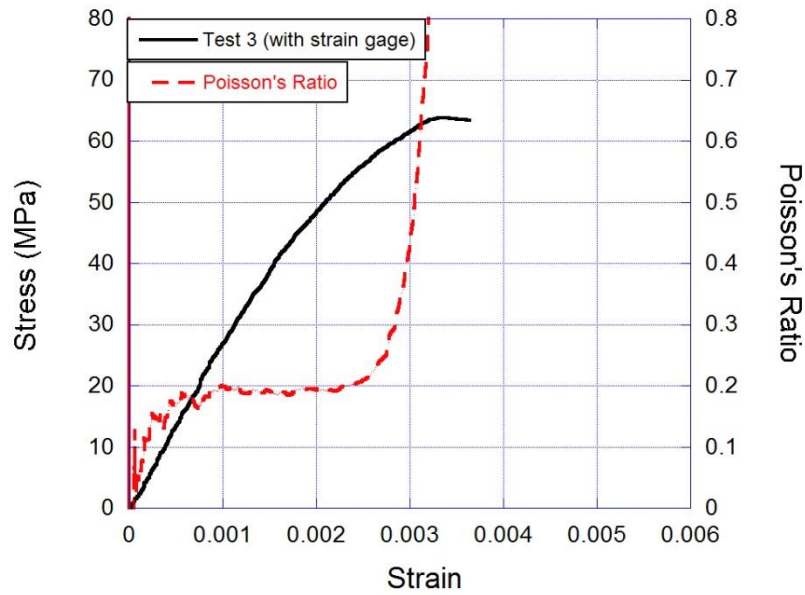


Figure 3.8. Test 3 stress-strain and Poisson's ratio 10^{-3} s^{-1} strain rate

The measured strain rate in the specimen was found as $3.22 \times 10^{-4} \text{ s}^{-1}$ in Figure 3.9 when the cross-head speed is equal to 0.045 mm/s. Stress-strain comparison of the three 10^{-4} s^{-1} strain rate tests is shown in Figure 3.10. In this figure, it can be seen that test 1 and test 3 exhibit very similar behavior but test 2 shows a little bit higher stress and strain values at failure.

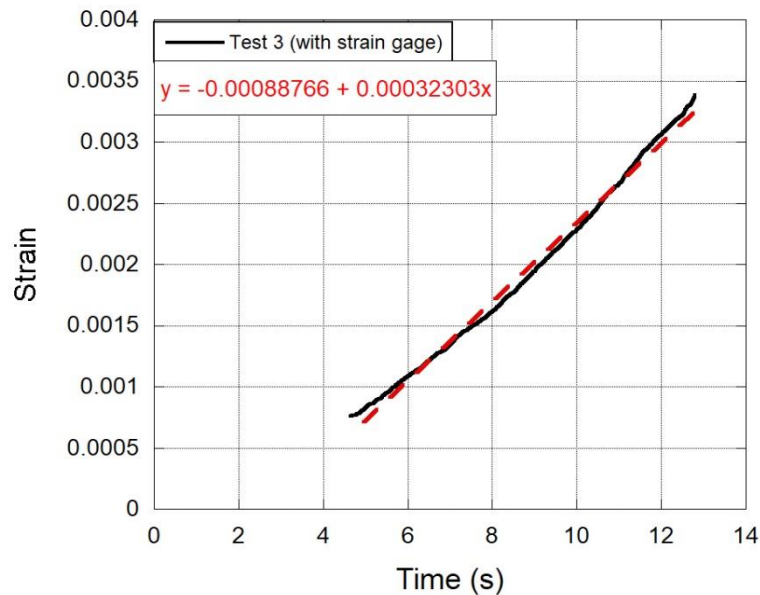


Figure 3.9. Test 3 actual strain rate fit at 0.045 mm/s cross head speed

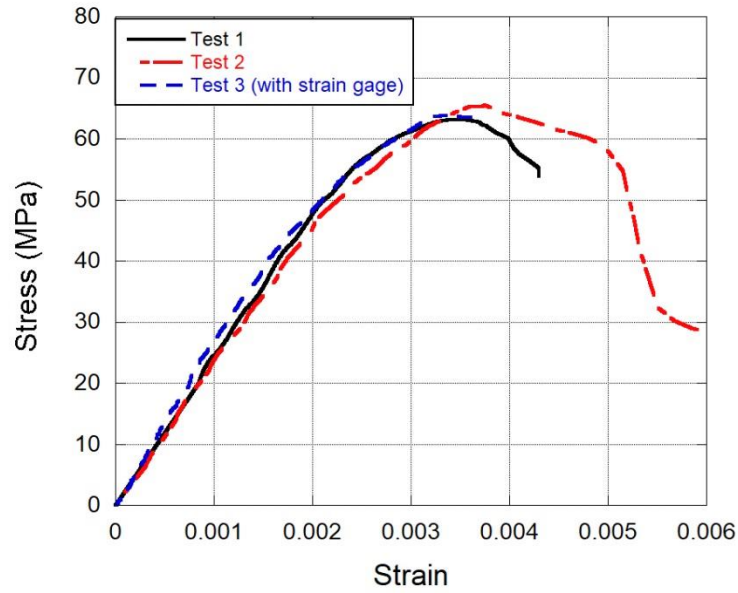


Figure 3.10. Stress-strain comparison at 10^{-3} s^{-1} strain rate

The last group of quasi-static tests was performed at 10^{-2} s^{-1} strain rate having 0.45 mm/s cross-head speed. Figure 3.11 and Figure 3.12 shows the stress-strain curves of tests whose strain data were recorded by video extensometer. In both figures, the elastic region of the stress-strain curve had almost upright direction with very small strain values. On the other hand, the test with strain gage data acquisition exhibited better linear-elastic region than the previous tests.

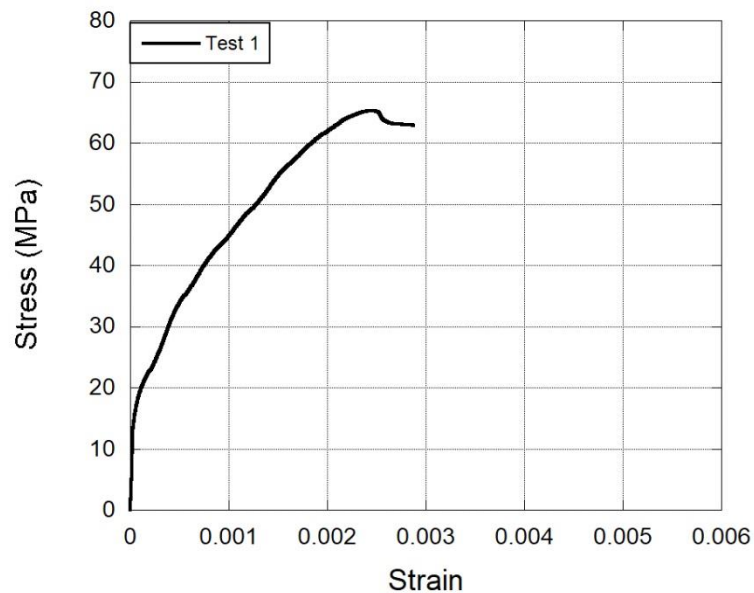


Figure 3.11. Test 1 stress-strain curve for 10^{-2} s^{-1} strain rate

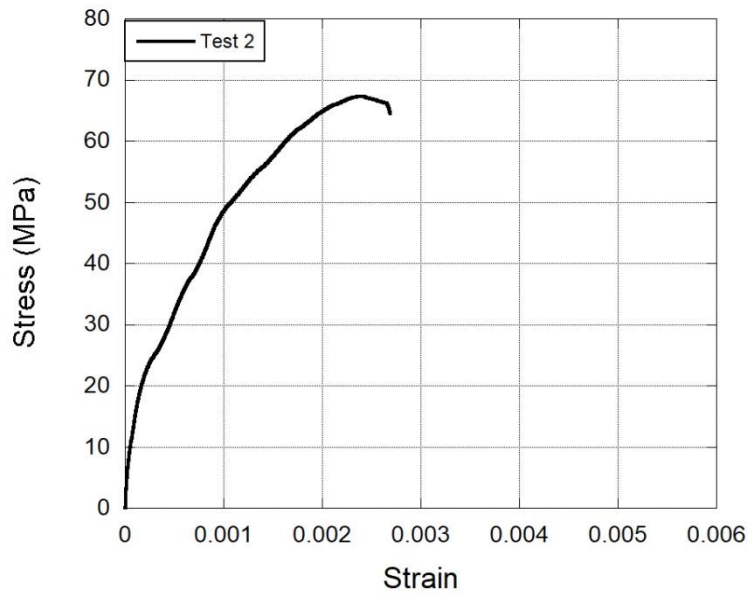


Figure 3.12. Test 2 stress-strain curve for 10^{-2} s^{-1} strain rate

Stress-strain curve of the last test at 10^{-2} s^{-1} strain rate is shown in Figure 3.13. Similar to the tests at different strain rates, the strain data was recorded by strain gages mounted on the specimen in this test. Figure 3.14 shows the test using strain gage that maximum stress reaches 70 MPa at 0.0037 strain at failure. Poisson's ratio were found as 0.19.

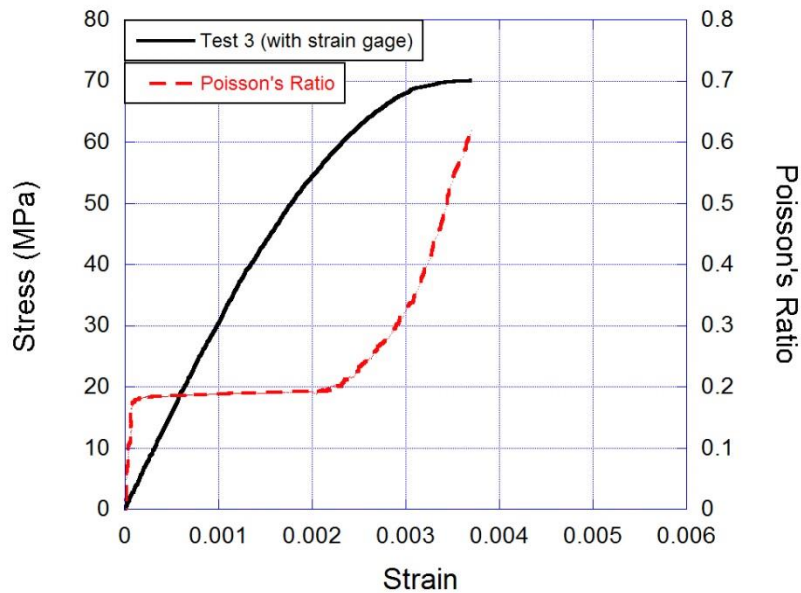


Figure 3.13. Test 3 stress-strain and Poisson's ratio 10^{-2} s^{-1} strain rate

The actual strain rate was measured as 2.971×10^{-3} with 0.45 mm/s crosshead speed as shown in Figure 3.14. The stress-strain comparison of three tests at 10^{-2} s^{-1} strain rate in Figure 3.15 demonstrates that test 1 and 2 results differ from the results obtained by the strain gage signal. Although, the peak stresses are close with each other among these tests, strain values obtained from extensometer are smaller than the strain value obtained from strain gage data. The reason for this, the extensometers are not enough sensitive to measure in the early stage of deformation.

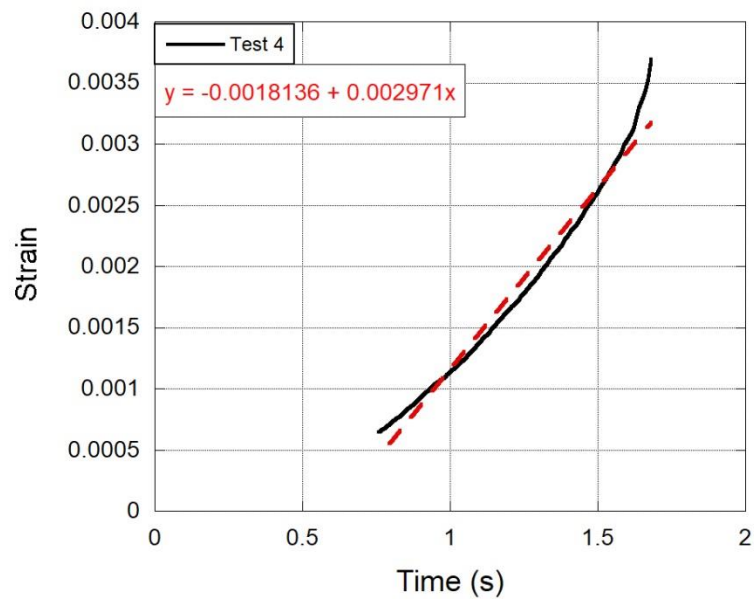


Figure 3.14. Test 3 actual strain rate fit at 0.45 mm/s cross head speed

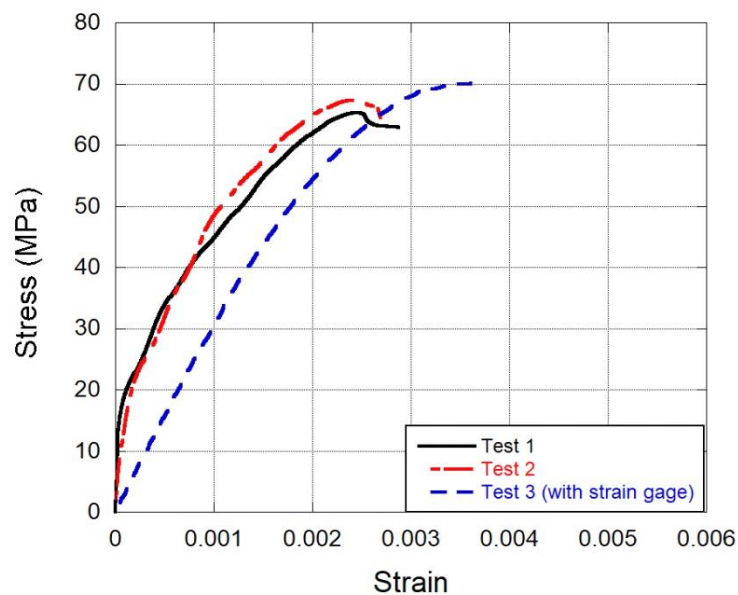


Figure 3.15. Stress-strain comparison at 10^{-2} s^{-1} strain rate

It can be seen in Figure 3.16, the failure strain is independent of strain rate. Thus, strain values were found as 0.0036-0.0037 which is identical for all three tests. However, it was obvious that strength increased with increasing strain rate. Peak stresses were recorded as 62 MPa, 64 MPa, and 70 MPa for 10^{-4} s^{-1} , 10^{-3} s^{-1} , and 10^{-2} s^{-1} strain rate, respectively. Also, elastic modulus did not change noticeably with changing strain rate in quasi-static range.

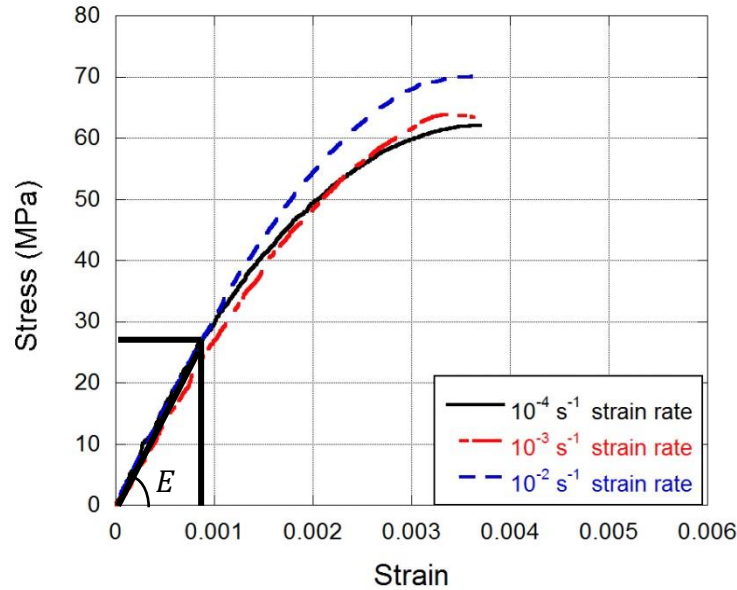


Figure 3.16. Stress-strain comparison at different strain rates

The average stress, strain, Poisson's ratio and the actual strain rates measured by strain gages are presented in Table 3.1.

Table 3.1. Mechanical properties of concrete at quasi-static strain rates

| Strain Rate (s^{-1}) | Cross Head Speed (mm/s) | Actual Strain Rate (s^{-1}) | Avg. Stress (MPa) | Avg. Strain | Poisson Ratio |
|---------------------------------|-------------------------|--|-------------------|-------------|---------------|
| 10^{-4} | 0.0045 | 3.55×10^{-5} | 62 | 0.0037 | 0.21 |
| 10^{-3} | 0.045 | 3.23×10^{-4} | 64 | 0.0036 | 0.20 |
| 10^{-2} | 0.45 | 2.97×10^{-3} | 70 | 0.0037 | 0.19 |

The splitting tensile test results to determine the tensile strength of concrete is shown in Figure 3.17. Three tests were performed according to ASTM C496 standard at 1 MPa/min loading rate. The duration of tests took in between 330 and 370 seconds and the tensile strength at failure was found as 6.3 MPa in average. The damage history of the split tensile test is illustrated in Figure 3.18. The first crack occurred in the same line with loading axis along the diameter of the specimen, Figure 3.18 (b). Then, new cracks were formed at the top portion of the specimen and these cracks grew through the center of the specimen causing fragmentation in the specimen.

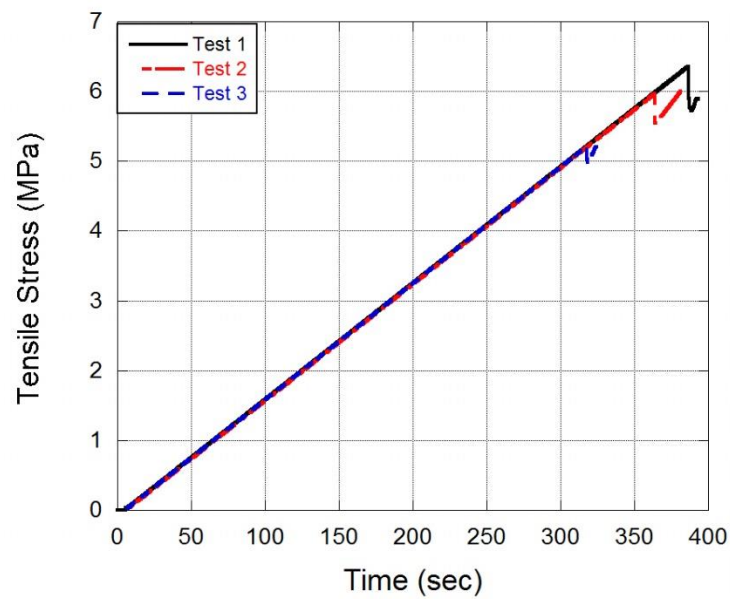


Figure 3.17. Split tensile test results

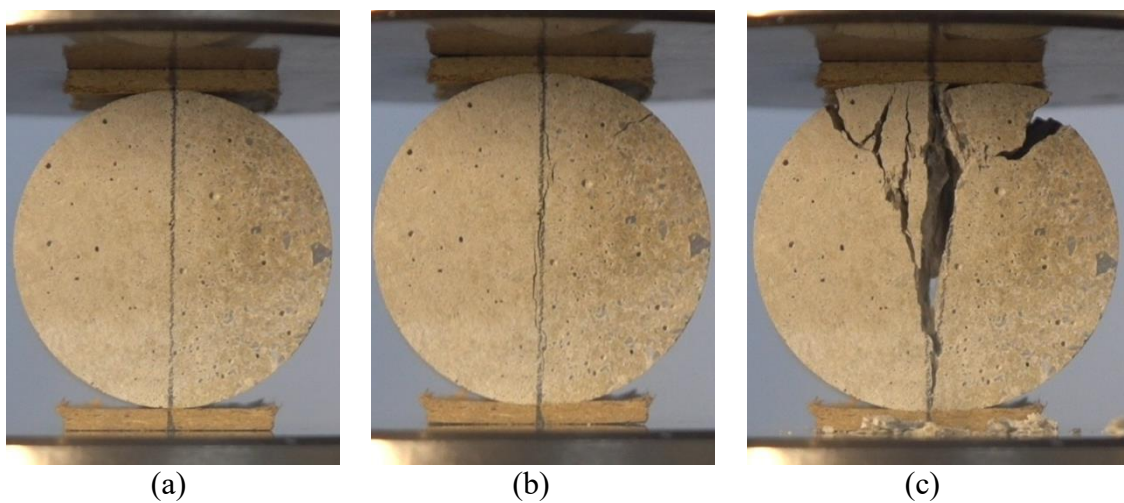


Figure 3.18. Split tensile test damage history of the specimen (a) undamaged, (b) first crack formation (c) damaged specimen

High strain rate tests were performed using 40 mm diameter aluminum Split Hopkinson Pressure Bar. In order to evaluate the effect of the pulse shaper on the dynamic behavior of concrete both tests with and without pulse shaper were executed with same incident pulse amplitude. Since insertion of pulse shaper affects the shape of the incident pulse and its amplitude, striker impact velocities were set to have a different value in order to have identical incident pulse level. Three tests were done for each case of dynamic tests. The striker velocities were recorded as 19.90 m/s for the first two and 20.22 m/s for the last test of without pulse shaper tests and 26.33 m/s, 28.28 m/s and 29.18 m/s for the tests with pulse shaper, respectively. Also, piezoelectric quartz crystal time-stress curves were recorded simultaneously with the stress waves. The time domains were identical for each test which was 600 microseconds.

In Figure 3.19, three stress histories of without pulse shaper tests are presented. Stress histories of the piezo-electric quartz crystals at the bar interfaces are shown accordingly. The first pulse in these graphs is the incident pulse and as the wave reaches specimen-bar interface the stress pulse of piezo-electric quartz crystals comes up. Then, a part of the incident wave turns back as a reflected pulse which is the only positive sign pulse and other part is transmitted to the transmitter bar named as transmitter pulse. Since, the distance between bar interfaces and strain gages are equal for both incident and transmitter bar, reflected and transmitted pulse were recorded at the same time with opposite signs.

It was observed that incident pulse amplitude was equal 200 MPa in the first two tests while 220 MPa in the third test. Also, the maximum stress developed on the piezo-electric quartz crystals was nearly equal for the first and the third test while transmitter piezo stress was higher than the incident piezo stress in the second test. For all three tests, transmitter piezo stresses were measured with 14 microseconds time delay from the incident piezo stress due to the wave propagation duration in the specimen.

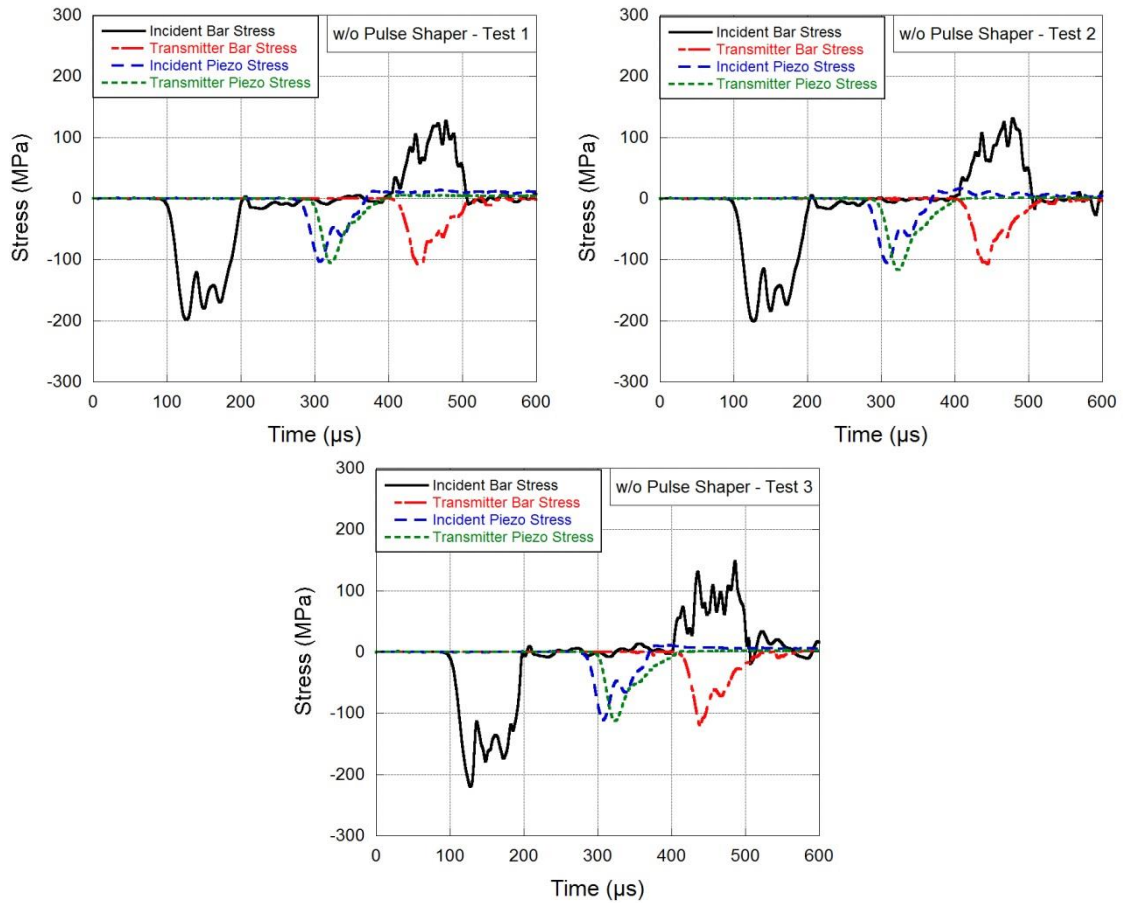


Figure 3.19. Stress histories of the without pulse shaper tests

The first test without pulse shaper test was chosen to show stress-strain curves, strain rate, force history and for further comparisons. The stress wave analysis of the without pulse shaper test is presented in Figure 3.20. The stress values were calculated according to the stress wave analysis formulations which are given in chapter 2. The two-wave analysis gives the maximum stress values at peak since it is the average of incident and reflected waves. The stress values in the three-wave analysis are between one-wave and two-wave as it is the average of the incident, reflected and transmitter wave. Lastly, one-wave analysis is obtained from transmitted signal which is lowest stress values at peak and less oscillatory than other wave analysis. On the contrary, strain values at peak stresses are lowest on the two-wave analysis and highest on the one-wave analysis.

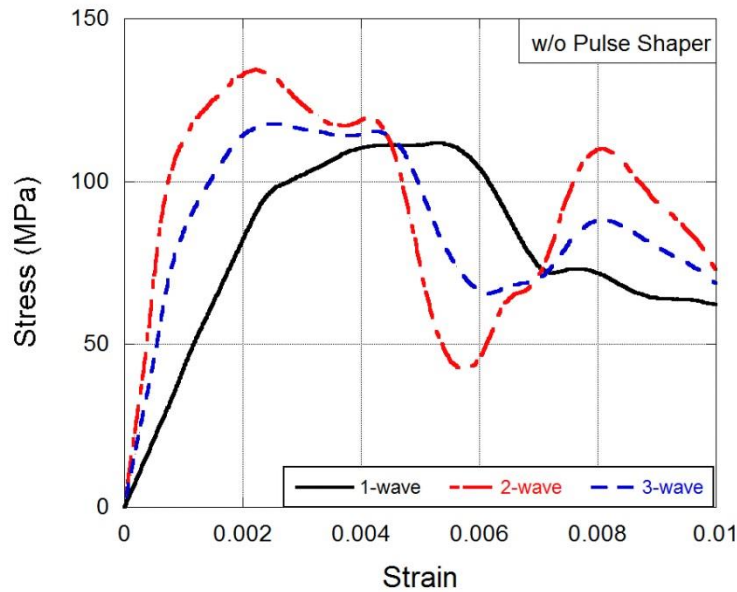


Figure 3.20. Stress wave analysis of the test without pulse shaper

Strain-strain rate history of the without pulse shaper test is shown in Figure 3.21 where strain rate reaches 247 s^{-1} at the failure strain 0.0047 as pointed out in the figure.

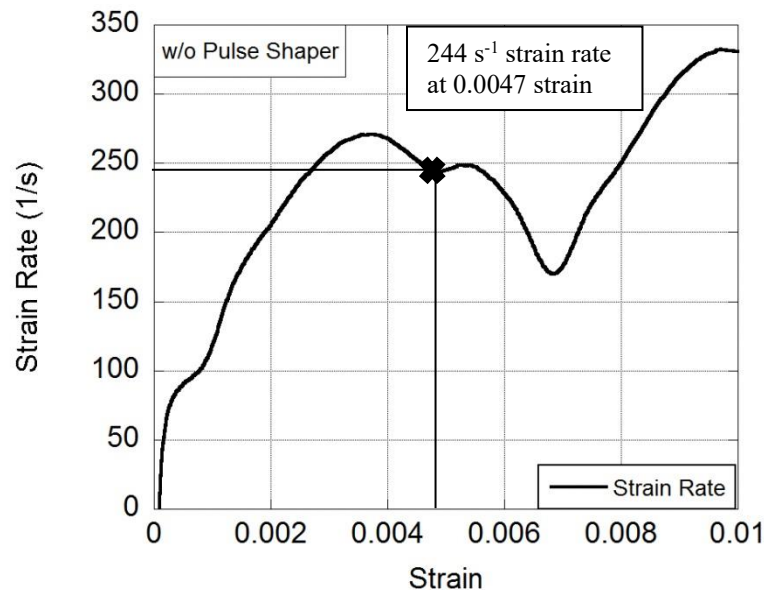


Figure 3.21. Strain-Strain rate history of the without pulse shaper test

The forces at the specimen-bar interfaces were measured by two methods. The first method was using strain gages on incident and transmitter bar. Force history of the specimen-transmitter bar interface was measured from transmitted signal only and incident bar force history was measure by taking the difference of incident and reflected pulse. On the other hand, forces were measured directly from the piezo-electric quartz

crystals which were embedded on the bar surfaces. The force-time histories of the piezo-electric quartz crystals and strain gages are shown in Figure 3.22. While the forces obtained from the strain gages have more oscillations, the force values of the quartz crystals are less oscillatory. Also, quartz crystals data showed that the forces on the back and front faces of the specimen reaches same maximum values and have a similar tendency. Whereas force data obtained from strain gages shows different force-time history and values.

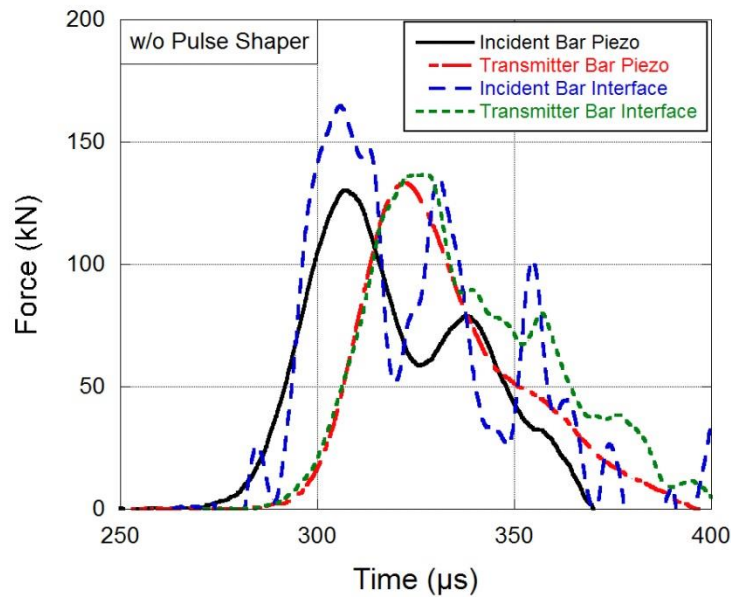


Figure 3.22. Force histories of the bar-specimen interfaces and quartz crystals of the without pulse shaper test

In this modified Split Hopkinson Pressure Bar test setup strain was calculated using strain gages which were mounted on the aluminum bars and stress can be calculated in two ways as it was mentioned earlier. These methods are using strain gage data and piezo-electric quartz crystals data. It is expected that both quartz crystals inserted on incident and transmitter bar interface provide the same amount of developed stress on the specimen. So, one-wave stress and incident piezo-electric stress are compared to each other as a function of strain in the specimen which was obtained from strain gages as shown in Figure 3.23. The plots showed that stress-strain curves have very similar behavior and nearly the same failure stress-strain values.

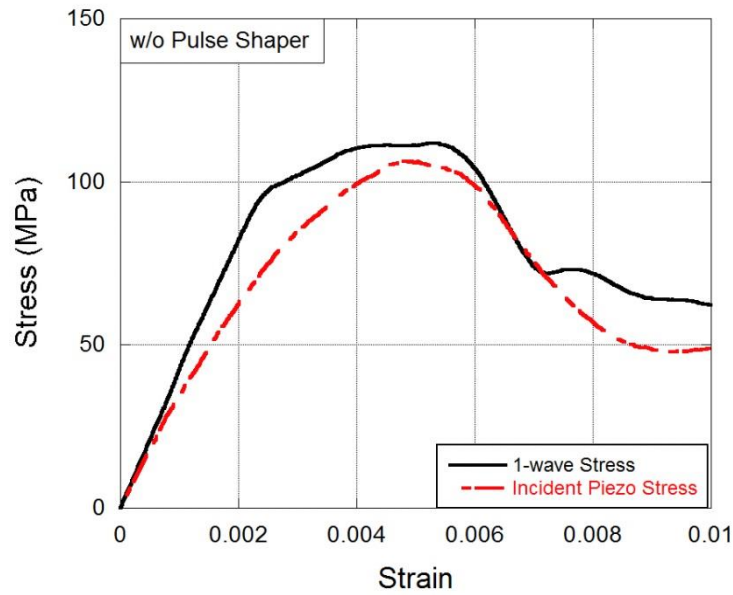


Figure 3.23. Stress-strain curve comparison of the 1-wave stress analysis and the incident piezo stress of the without pulse shaper test

Figure 3.24 shows the three stress histories of the test with pulse shaper on the modified Split Hopkinson Pressure Bar. The pulse shaper was placed the impact end of the incident bar. All these three tests were performed with piezo-electric quartz crystals inserted on specimen-bar interfaces. The signals were recorded as voltages and then converted to the stress values as it was mentioned previously.

It was observed that the maximum incident piezo stresses were higher than the transmitter piezo stresses for all three tests. Unlike the tests without pulse shaper, a common time delay was not observed between incident and transmitter piezo stresses for the tests with pulse shaper. Apart from that, incident pulse, reflected pulse, and transmitter pulse amplitudes are very close to each other.

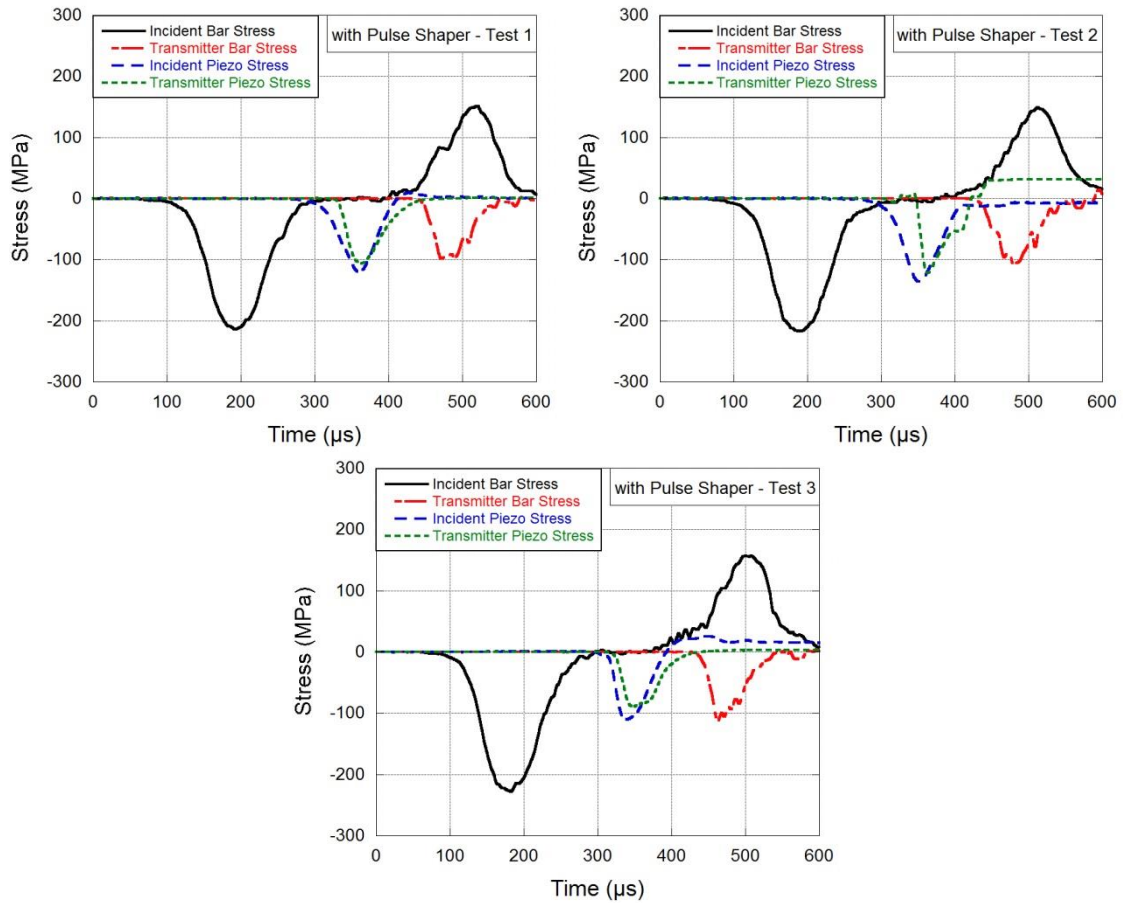


Figure 3.24. Stress histories of the with pulse shaper tests

The wave stress analysis comparison for the test with pulse shaper is presented in Figure 3.25. In this analysis, it can be clearly seen that failure strain and stress increases in the order of one-wave, three-wave, and two-wave analysis. However, 2-wave and 3-wave analyses results overestimate the failure stress and strain values for concrete. Peak stresses are 110 MPa and 125 MPa for 3-wave and 2-wave analysis respectively.

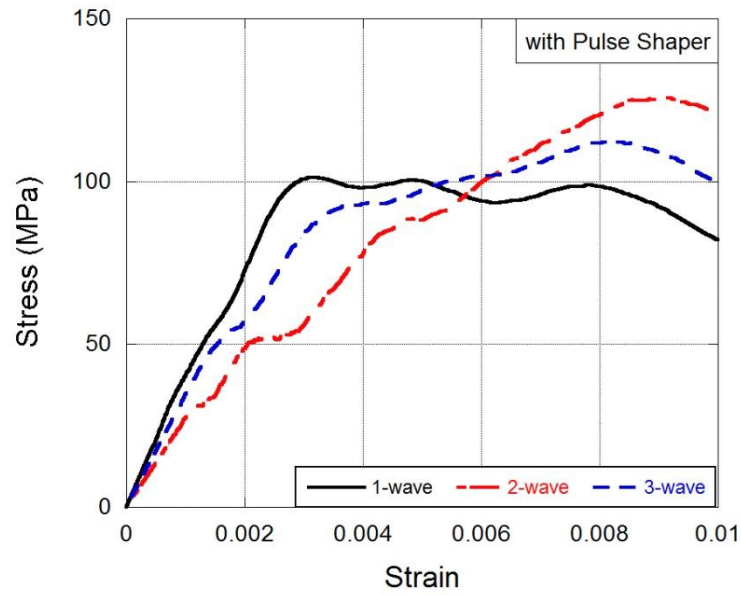


Figure 3.25. Stress wave analysis of the test with a pulse shaper

Strain rate history as a function of strain is given in Figure 3.26 for the test with pulse shaper. It was observed that the strain rate continuously increases as the strain increases. In failure strain 0.0057, strain rate reaches 242 s^{-1} as it is shown in the figure. It was important to reach the nearly same amount of strain rate at failure for both tests without pulse shaper and with pulse shaper, because in this way, the effect of pulse shaper usage can be directly observed without considering strain rate effect in an SHPB test of the concrete specimen.

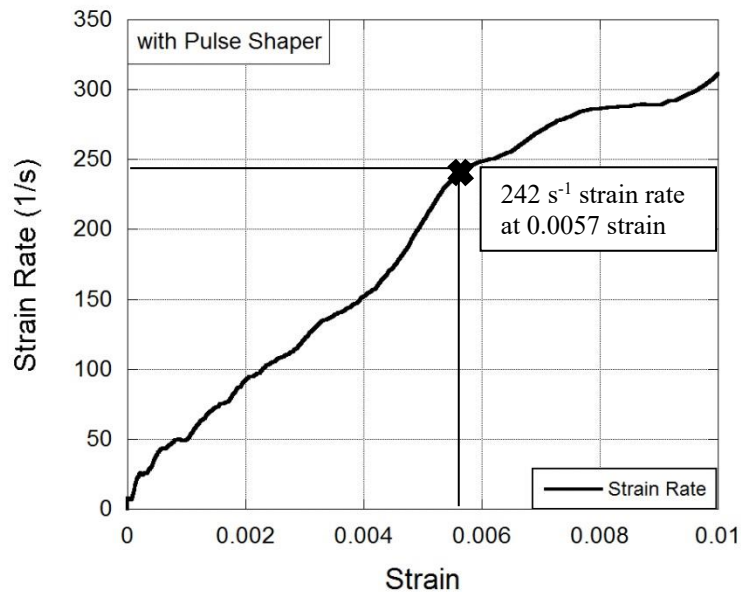


Figure 3.26. Strain-Strain rate history of the with pulse shaper test

The force histories acquired by the strain gages and piezo-electric quartz crystals for the test with pulse shaper are given in Figure 3.27. The usage of pulse shaper changed the force histories dramatically over the time. The incident bar piezo force and the incident bar force obtained from strain gage almost overlap each other. Likewise, the transmitter bar piezo force and transmitter bar force follow the same path except for the top portion of the curve. The transmitter bar force exhibits a little oscillatory behavior and less magnitude than transmitter piezo force. However, this graph proves that force measurements by the piezo-electric quartz crystals work very well compared with strain gage signals. Piezo-electric quartz crystal signals provide more uniform and non-oscillatory force history than the strain gage data. Also, it was detected that incident force on both strain gage and quartz crystal force data provides a little higher force measurement than transmitter force.

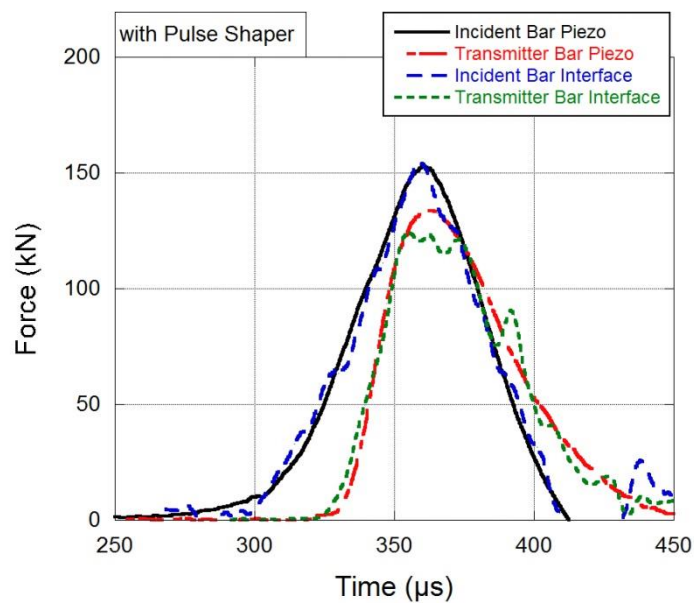


Figure 3.27. Force histories of the bar-specimen interfaces and quartz crystals of the with pulse shaper test

The stress-strain curve comparison of the strain gage data and the piezo-electric quartz crystal data is shown in Figure 3.28. The one-wave stress was calculated using transmitter bar strain gage signals and the piezo stress was measured by incident bar quartz crystal as it mentioned previously. While incident piezo stress shows a linear behavior until 0.002 strain at 80 MPa and then plastically deforms till the peak stress reaches 110 MPa and 0.0050 strain. One-wave stress goes up linear behavior until 0.001

strain at 40 MPa then it reaches 101 MPa at 0.0030 strain and fluctuates through around 0.0080 strain at 100 MPa.

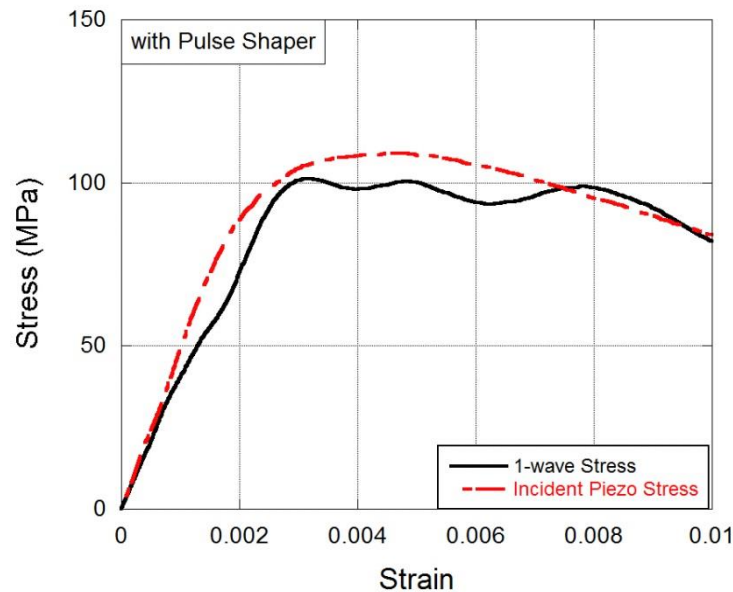


Figure 3.28. Stress-strain curve comparison of the 1-wave stress analysis and the incident piezo stress of the with pulse shaper test

To compare the effect of pulse shaper, the first test of both tests with and without pulse shaper was chosen. The graphs are presented in between Figure 3.29 and Figure 3.32. A pulse shaper can produce a ramp pulse instead of a rectangular pulse to have constant strain rate during elastic deformation and controlled damage for a ceramic specimen in a constant strain rate as it mentioned by (Subhash and Ravichandran, 2000).

As it can be seen in Figure 3.29, the usage of pulse shaper considerably affects incident pulse shape. The rise time rise time and total length increase when a pulse shaper is used. While incident pulse duration was 115 microseconds for the test without pulse shaper, using pulse shaper extended the incident pulse duration almost double. Also using pulse shaper provides non-oscillatory, uniform stress wave propagation through the specimen.

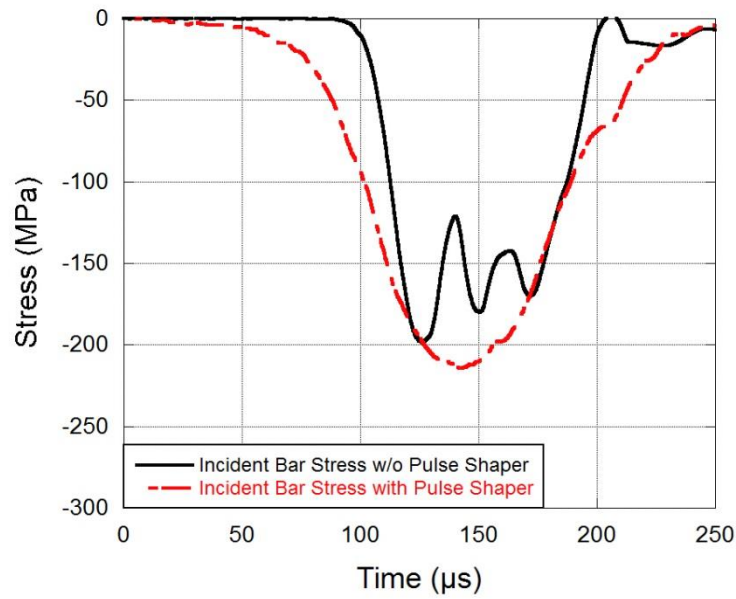


Figure 3.29. The effect of pulse shaper on the incident pulse shape

In Figure 3.30, the effect of using pulse shaper on the behavior of stress-strain curves is presented. On the left graph, one-wave analysis stress-strain curves are presented and on the right graph incident piezo stresses for both without and with pulse shaper tests is presented.

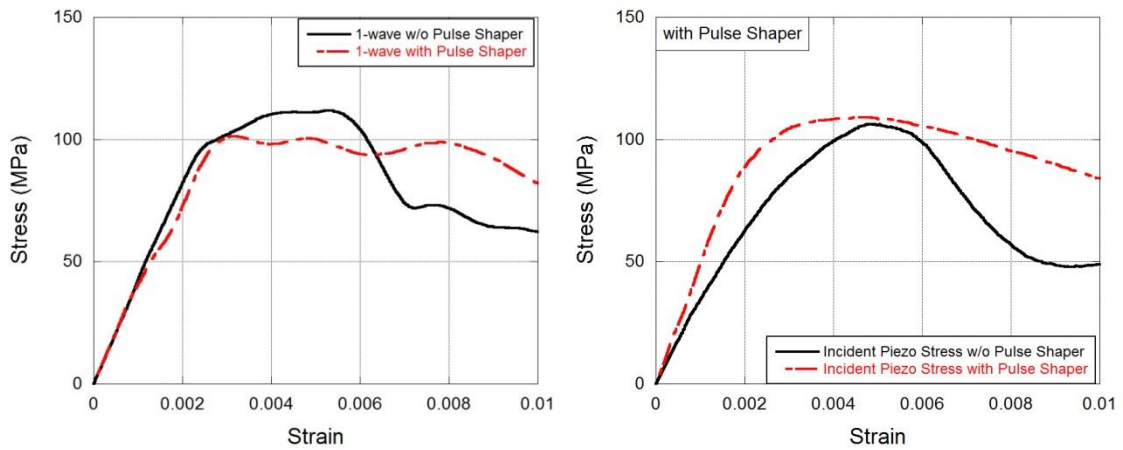


Figure 3.30. The effect of pulse shaper on the 1-wave stress analysis and stress produced by piezo-electric quartz crystals

The comparison of strain rate-strain behavior of concrete is given in Figure 3.31. The insertion pulse shaper was ensured the slowly increase in the strain rate during the deformation of the specimen. However, the test without pulse shaper indicates a rapid increase in the strain rate even in the initial stages of deformation which may cause a premature failure of the concrete sample (Tasdemirci et al., 2016).

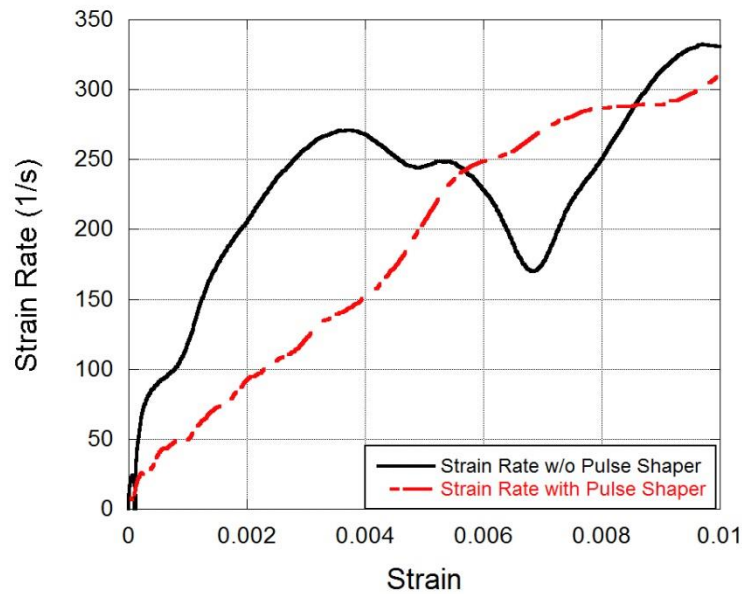


Figure 3.31. The effect of pulse shaper on the strain-strain rate behavior

The stress equilibrium comparison is carried out in Figure 3.32 to see the effect of pulse shaper on the stress balance at both ends of the specimen. Equilibrium can be satisfied when $R(t)$ value reaches zero. However, it is generally accepted that within 5% stress difference on the end surfaces of the specimen assumed to be reasonable approach for dynamic stress equilibrium. Thus, it may be said that dynamic stress equilibrium can be attained better with using pulse shaper as can be seen in Figure 3.32. Also, using pulse shaper prevents oscillations in the $R(t)$ - strain curves (Tasdemirci et al., 2016).

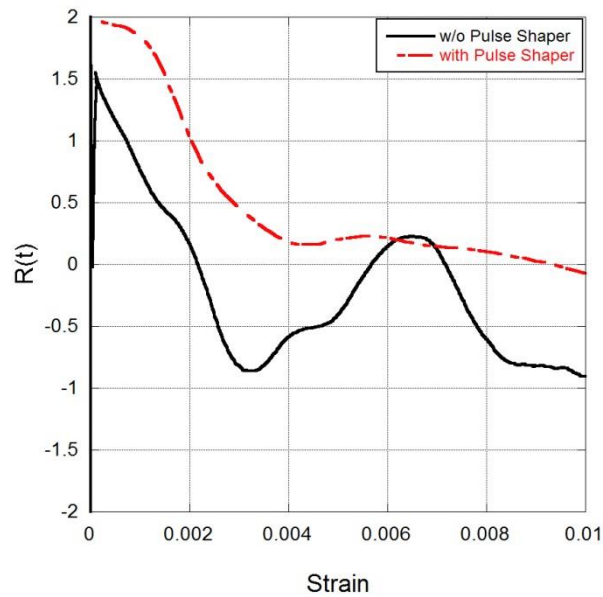


Figure 3.32. The effect of pulse shaper on the dynamic stress equilibrium parameter

In Figure 3.33, stress-strain results of dynamic and quasi-static tests at each strain rates are presented. As it was mentioned earlier, the compressive strength of concrete at the lowest bound of quasi-static strain rate tests was found as 62 MPa in average. However, apparent strength increase takes place with increasing strain rate up to $240\text{-}250\text{ s}^{-1}$ in dynamic testing of concrete. The average dynamic strength of concrete measured as 106 MPa which is 1.7 times of quasi-static strength. Correspondingly, the modulus of elasticity of concrete at quasi-static and dynamic tests differed from each other. Modulus of elasticity can be calculated as taking the slope of stress and strain value at 45% of failure strength of quasi-static and dynamic tests (ACI Committee 318, 2008). As it can be seen from Figure 3.33, static modulus of elasticity, (E_s) is found as 32 GPa where the dynamic modulus of elasticity, (E_d) is calculated as 41.48 GPa. This indicates that there is a 30% increase in the modulus of elasticity of concrete at higher strain rates.

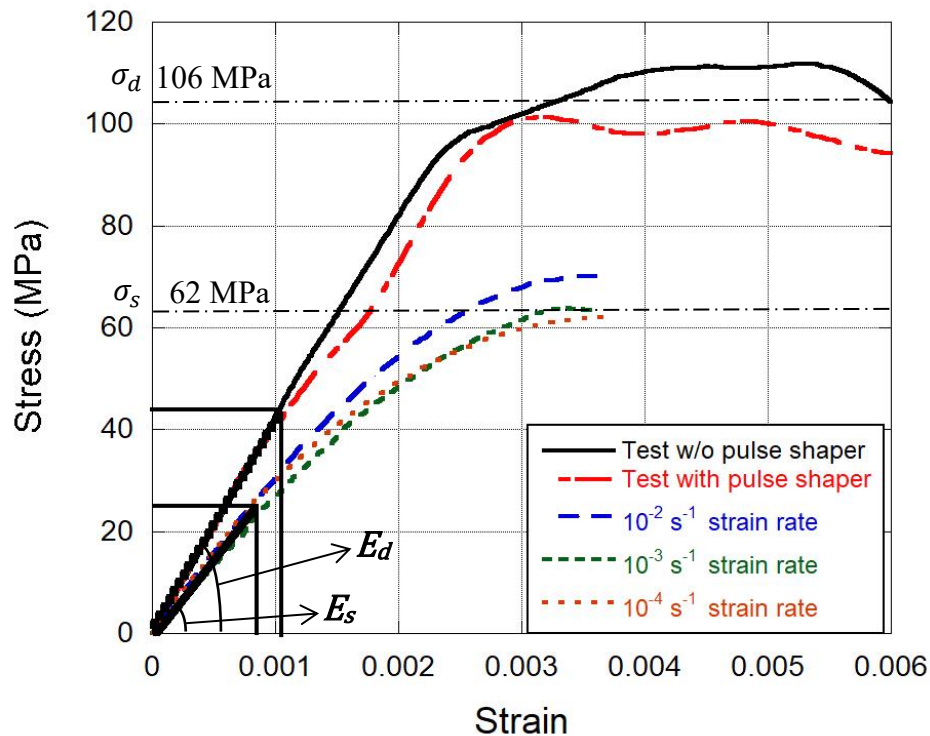


Figure 3.33. Stress-strain and modulus of elasticity comparison of dynamic and quasi-static tests

Subhash and Ravichandran reported that the reason for different behavior of quasi-static and dynamic tests of ceramic materials is microstructure of ceramic materials. Two discrepancies were observed with increasing strain rate. These are an increase in fracture strength and an increase in the number of microcrack initiation from various locations. They also stated that crack growth of brittle materials follows the same direction with loading axis during uniaxial compressive loading. Also, in quasi-static loading, when the stress level is enough to initiate a crack, a single crack starts from a weakest point and grows with the stored energy until the failure of the material. However, the rate of loading in dynamic tests is much greater than the crack growth rate. So, several cracks occur and grow instantaneously in the specimen due to the inertia related behavior of crack tip opening (Subhash and Ravichandran, 2000).

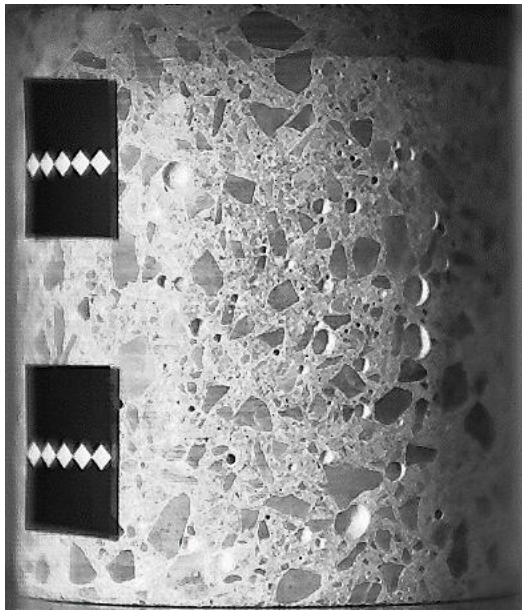
Cui et al. pointed out that the weakest bond in concrete takes place in between aggregate and mortar interfaces. Due to this reason, failure occurs in these weak areas under static loadings. In high strain rate loading, on the other hand, there is not enough time for crack formation through the weak interface. Instead, new cracks occur and follow the relatively high strength regions like aggregates itself (Cui et al., 2017). Failure of aggregates in high strain rates was also utilized as one of the reasons of dynamic strength enhancement of the concrete by (Y. Hao and Hao, 2011). Lu et. al

explained the mechanism of failure of concrete by thermal vibration of atoms called thermo-activated mechanism. In this mechanism, atomic bonds are broken due to thermal vibration and increasing strain rate causes an increase in the vibration energy. So, new cracks occur and existent cracks grow with the energy dissipation. When the strain rate is higher than the critical level, there is no time for crack growth. Consequently, the concrete will fail with multiple crack formation not through weakest interface but inside of the aggregates increasing the dynamic strength of the concrete (Lu et al., 2017).

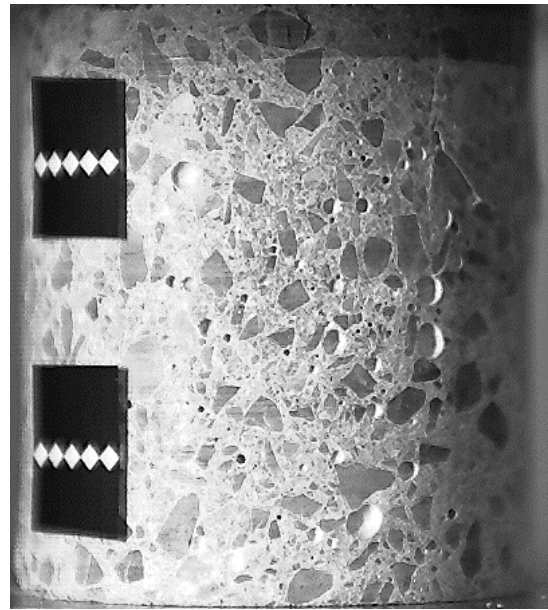
The crack initiation and deformation progression were captured using a high-speed camera in both quasi-static and high strain rate test. To show the difference between crack formation and damage mode of concrete at different strain rates, images captured from the high-speed camera are presented in Figure 3.34 and Figure 3.35. The quasi-static test images in Figure 3.34, illustrates the deformation at 10^{-3} s^{-1} strain rate. High strain rate test images were captured at the test with pulse shaper 250 s^{-1} .

In the quasi-static test, a high-speed camera at 10000 fps (frame per second) was used to record deformation. The undamaged specimen is shown in Figure 3.34 (a). In Figure 3.34 (b), cracks start from the weakest area which is at the right top portion of the image and follows the same direction with the loading axis. Next, new cracks occur in the bottom part of the specimen surface especially aggregate and cement interface, Figure 3.34 (c). As the stored energy in the specimen is enough the fail the material, bigger crack occurs through the length of the specimen causing failure from aggregates interface in Figure 3.34 (d).

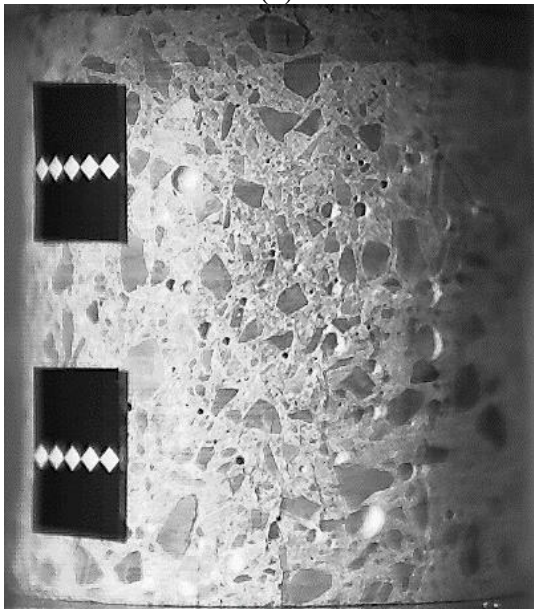
The high-speed camera images of the high strain rate test are shown in Figure 3.35. To observe deformation process more apparent, the maximum achievable frame rate at this frame was chosen which was 37500 fps resulting 26 microseconds per image. The first image illustrates the undamaged specimen at time zero. Next image shows the fully compressed specimen where the stress reaches its maximum value. Then next image shows the first crack formations that formed cracks are slightly visible at the surface of the specimen. Last image illustrates the fully damaged specimen that specimen fall apart into many small pieces. Also, cracks proceed not only cement-aggregates interfaces but also passes though aggregates itself because there is no time for cracks find the weakest spot and grow. This leads to one of the commonly known reason of increase in dynamic strength of the concrete material.



(a)



(b)



(c)



(d)

Figure 3.34. The deformation initiation/progression of a quasi-static compression test

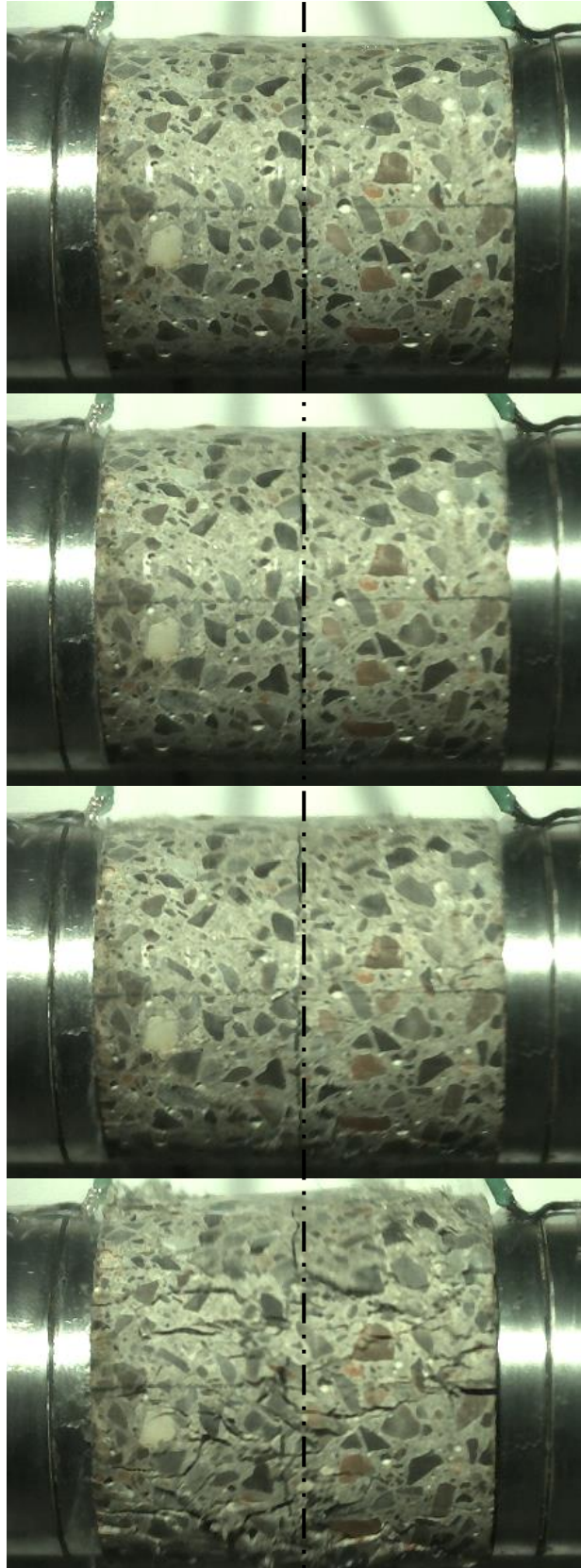


Figure 3.35. The deformation initiation/progression of a SHPB test

3.3 Johnson-Holmquist-Cook Material Model

Holmquist-Johnson-Cook (HJC) model was proposed by Holmquist et al. in 1993 in order to develop a constitutive concrete model for impact computations (Holmquist et al., 1993). The material in this model is subjected to large strains, high strain rates, and high pressures. To determine compressive stress-strain response and dynamic behavior of concrete at high strain rates in this study, HJC material model was selected for its simplicity, accuracy, and compatibility with large-scale computations. In addition, HJC material model code is built in finite element tool LS-DYNA as MAT_JOHNSON_HOLMQUIST_CONCRETE (MAT_111) so that dynamic behavior of concrete can be investigated by numerically using LS-DYNA (Livermore Software Technology Corporation, 2016). Thus, HJC material model defined in material model library in LS-DYNA was used to model concrete specimen in the numerical simulations of the SHPB tests.

Holmquist et al. expressed the stress as a function of pressure, damage and strain rate in Equation 3.1. In this expression, σ^* is the normalized equivalent stress and it is found by σ/f'_c , where σ is the actual equivalent stress and f'_c is the quasi-static uniaxial compressive strength. The strength and pressure relation of the model is shown in Figure 3.36.

$$\sigma^* = [A(1 - D) + BP^{*N}][1 + C \ln \dot{\epsilon}^*] \quad (3.1)$$

where, P^* is the normalized pressure found by P/f'_c and P is the actual pressure. S_{max} is the normalized maximum strength. A is the normalized cohesive strength and found by the interception point of σ^* at $P^* = 0$. B is the normalized pressure hardening exponent. C is the strain rate constant. D is the damage ($0 \leq D \leq 1$). $\dot{\epsilon}^*$ is defined as the dimensionless strain rate given by $\dot{\epsilon}^* = \dot{\epsilon}/\dot{\epsilon}_0$ where $\dot{\epsilon}$ is the actual strain rate and $\dot{\epsilon}_0$ is the reference strain rate.

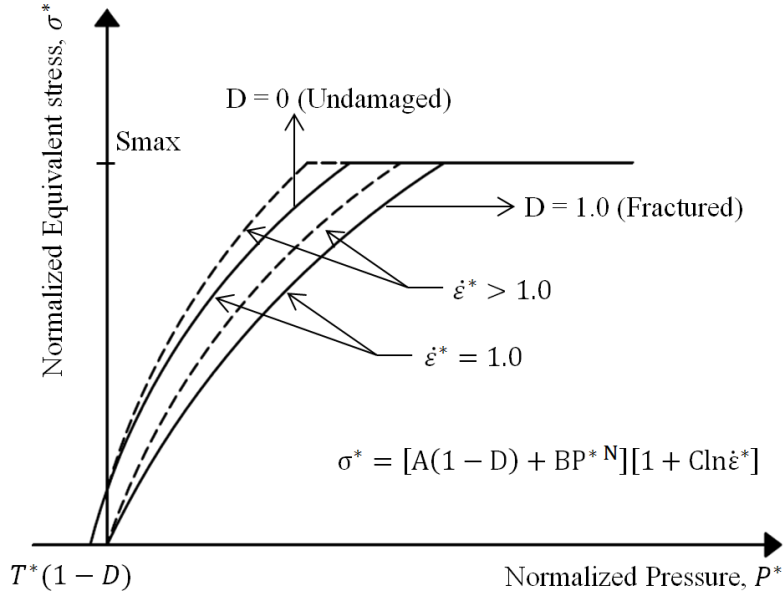


Figure 3.36. Normalized pressure-equivalent stress relation of the HJC model

The material damage in the HJC model is accumulated from strains. Both equivalent plastic strain and plastic volumetric strain are gathered for damage parameter. Damage is defined in Equation 3.2.

$$D = \sum \frac{\Delta\varepsilon_p + \Delta\mu_p}{\varepsilon_p^f + \mu_p^f} \quad (3.2)$$

where, $\Delta\varepsilon_p$ is equivalent plastic strain increment and $\Delta\mu_p$ is volumetric plastic strain increment. $\varepsilon_p^f + \mu_p^f = f(P)$ is the total plastic strain to fracture and it is defined as follows:

$$\varepsilon_p^f + \mu_p^f = D_1(P^* + T^*)^{D_2} \geq \varepsilon_p^f \min \quad (3.3)$$

where D_1 and D_2 are damage constants. T^* is the normalized hydrostatic tensile strength. $\varepsilon_p^f \min$ (EFMIN) is another damage constant providing fracture of the material at a certain amount of plastic strain. Figure 3.37 shows damage for fracture in as a function of pressure. As the normalized pressure increases plastic strain to fracture increases.

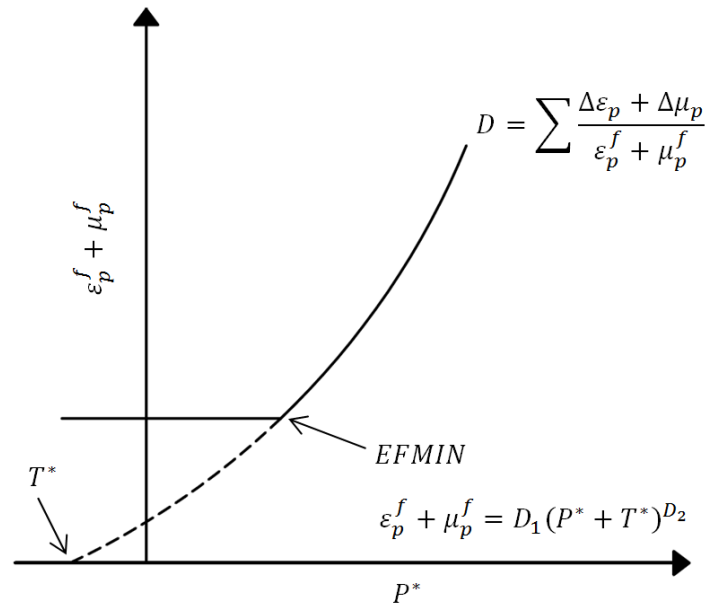


Figure 3.37. Normalized pressure and damage relation of HJC model

The hydrostatic pressure-volume relationship is shown in Figure 3.38. The relation between pressure and volume is described in three different regions. The first region states linear elastic region where $P \leq P_{crush}$. P_{crush} and μ_{crush} are the pressure and volumetric strain values at the upper end of first region. Second region is called as transition region where $P_{crush} \leq P \leq P_{lock}$. In this region, as pressure value goes P_{crush} to P_{lock} the material undergoes plastic volumetric strain and by compressing the air voids out of concrete with increasing plastic volumetric strain causes compaction damage until reaching P_{lock} and μ_{lock} . The third region starts when the air voids are totally removed from material when pressure reaches to P_{lock} . In this region, all the air voids in the material are collapsed. So, the material is called as fully dense material and cannot be compressible any further. The material is fully compacted in this stage, correspondingly P_{lock} and μ_{lock} are fully compacted pressure and volumetric strain, respectively. Consequently, pressure rises rapidly when small amount of increase in volumetric strain.

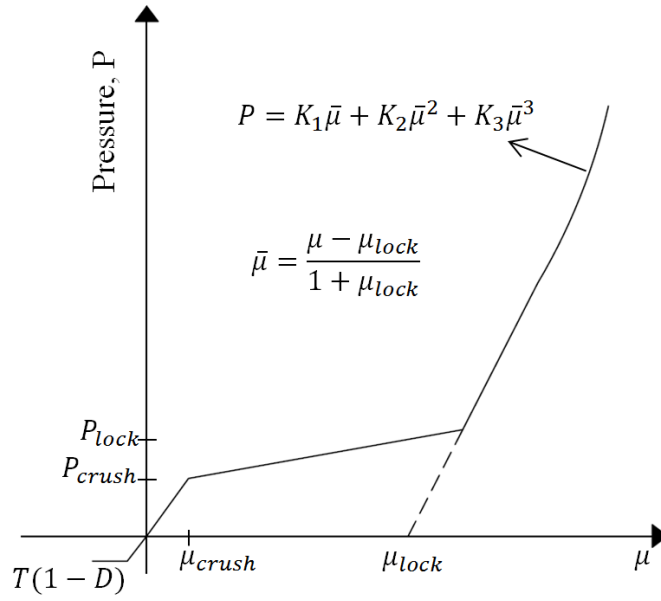


Figure 3.38. The hydrostatic pressure-volume relation of HJC model

The expression for this region is given in Equation 3.4. K_1 , K_2 , and K_3 are three constants to fit the cubic polynomial equation to the test data.

$$P = K_1\bar{\mu} + K_2\bar{\mu}^2 + K_3\bar{\mu}^3 \quad (3.4)$$

Pressure is given as a function of volumetric strain, $\bar{\mu}$, where

$$\bar{\mu} = \frac{\mu - \mu_{lock}}{1 + \mu_{lock}} \quad (3.5)$$

The standard volumetric strain is $\mu = \rho/\rho_0 - 1$ where ρ is the current density and ρ_0 is the initial density. The locking volumetric strain (μ_{lock}) was found using $\mu_{lock} = \rho_{grain}/\rho_0 - 1$ where ρ_{grain} is the density of the material without any voids.

3.4 Determination of Model Parameters

HJC material model constants were determined using both results of experiments and numerical analysis. First, the mass density of the cylindrical concrete sample was found by dividing the mass by volume of the cylinder and it was calculated as 2183 kg/m³. Quasi-static uniaxial compressive strength, f'_c and Poisson's ratio, ν ,

were calculated from quasi-static tests results. Three compressive quasi-static test results at 0.0045 mm/s cross-head speed which was the lowest rate of deformation were used to find f'_c . Uniaxial compressive strength (f'_c) of concrete was measured as 62 MPa. Poisson's ratio of the concrete determined using strain gage data and calculated as 0.2. Elastic modulus of concrete samples were determined using ACI 318-08 standard. Average elastic modulus, E , was found as 32 GPa by taking the slope of quasi-static stress-strain curve where stress values reach up to $0.45f'_c$. The shear modulus, G , was calculated by using the equation $G = E/2(1 + \nu)$ which was resulted as 13.32 GPa.

The reference strain rate ($\dot{\epsilon}_0$) was selected as $3.554 \times 10^{-5} \text{ s}^{-1}$ which was the smallest strain rate obtained in the quasi-static tests. The maximum tensile hydrostatic pressure parameter, T is defined as the maximum tensile strength of the material can withstand. T was found as 6.3 MPa by averaging the three split tensile tests. Normalizing T by f'_c results in $T^* = 0.102$. Afterwards, strain rate sensitivity parameter (C) was determined. Least square fit method was performed to the strain rate–stress data as shown in Figure 3.39. Stress values were normalized with $f'_c = 62 \text{ MPa}$ and corresponding strain rate values were used for each quasi-static and dynamic test.

In Figure 3.39, two strain rate sensitivity parameters were found C_{static} and C_{dynamic} . Quasi-static tests were used to find C_{static} fit whereas both quasi-static and dynamic tests were used to find C_{dynamic} fit. Strain rate sensitivity parameter including dynamic tests (C_{dynamic}) was found as 0.0472 which is 2.3 times of the C_{static} where only static tests were considered ($C_{\text{static}}=0.0205$). This shows that strain rate coefficient is influenced with not only strain rate but also other factors such as dynamic confinement effects, micro-inertial effects, and transition of uniaxial stress state to uniaxial strain in high strain rate tests. For this reason, $C_{\text{static}}=0.0205$ value was selected as the strain rate parameter to see only the strain rate effect without including hydrostatic pressure effects on the strength increase of the material itself (Tasdemirci et al., 2018).

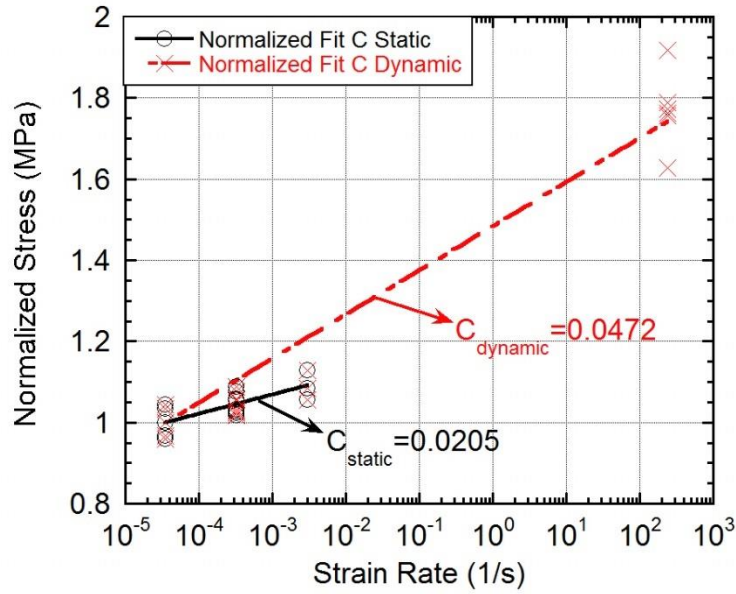


Figure 3.39. Strain rate sensitivity parameter fit

Next, normalized maximum strength (S_{max}), normalized cohesive strength (A), and pressure hardening coefficient (N) were determined using the data provided by (Hanchak et al., 1992). S_{max} is the maximum stress where the stress values no longer increase with increasing pressure (Figure 3.36). The shear strength and pressure relation for determining S_{max} is presented in Figure 3.40. This figure shows that shear strength increased with increasing pressure for both 48 MPa and 140 MPa concrete and nearly parallel to each other. Thus, a curve of 62 MPa concrete can be interpolated in between these curves and normalizing shear strength values by f'_c resulted in S_{max} value as 5.70.

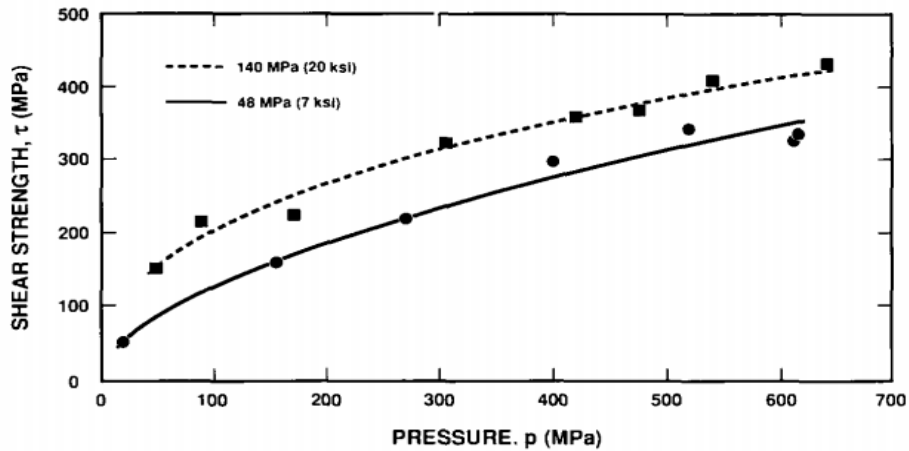


Figure 3.40. Pressure-Shear strength relation for 48 MPa and 140 MPa concrete slabs (Source: Hanchak et al., 1992).

Normalized cohesive strength was taken from literature as $A=0.79$ where A is the difference between the undamaged strength and completely fractured strength at a given pressure in Figure 3.36. Pressure hardening exponent was taken as $N=0.61$ as stated in the literature by setting a fit through fractured material strength. Normalized pressure hardening coefficient, (B) was found as 0.90 by fitting numerical transmitter bar stress to the experimental stress by parametric trials on the B value as shown in Figure 3.41.

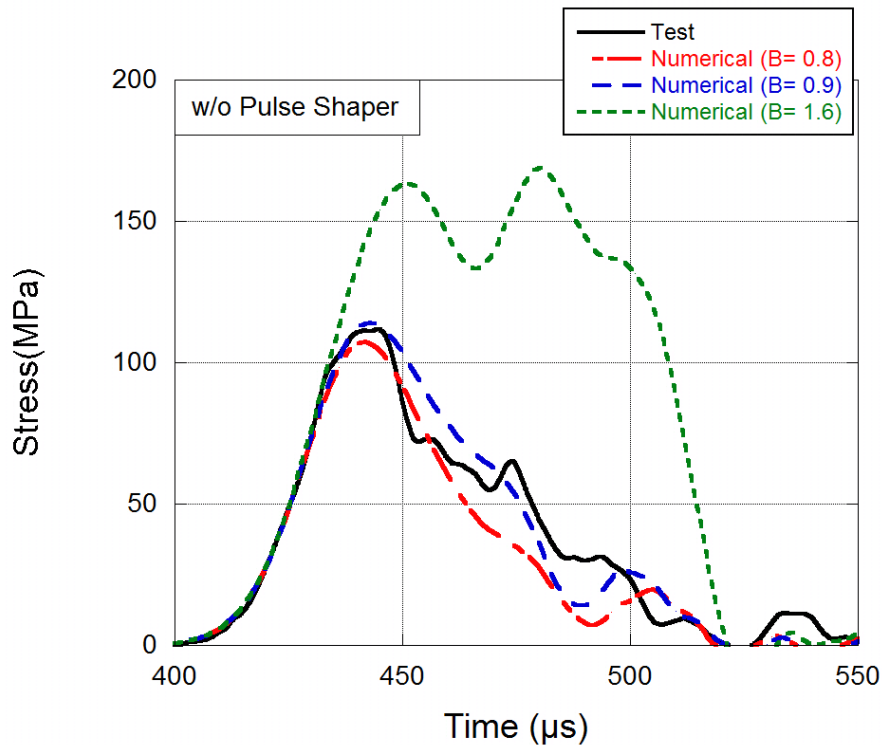


Figure 3.41. Transmitter bar stress and numerical trials

Next, the parameters to define fully compacted region which is the third region were determined. Crushing pressure (P_{crush}) was determined using $f'_c/3$ and it was found as 21 MPa. To determine volumetric crushing strain (μ_{crush}) where $\mu_{crush} = P_{crush}/K_{elastic}$ first elastic bulk modulus $K_{elastic}$ was found using elasticity theory ($K_{elastic} = E/3(1 - 2\nu)$) which is 17.77 GPa. Then, μ_{crush} was found as 0.001. The locking volumetric strain (μ_{lock}) defines the air void ratio of the material and it was found using $\mu_{lock} = \rho_{grain}/\rho_0 - 1$ where ρ_{grain} is the grain density and ρ_0 is the initial mass density of the material where $\rho_{grain}=2560 \text{ kg/m}^3$ and $\rho_0=2183 \text{ kg/m}^3$. So, locking volumetric strain can be found as 0.173. Locking pressure (P_{lock}) is the pressure where all the air voids are removed from the material and it was taken from literature as

$P_{lock} = 0.80$ GPa (Holmquist et al., 1993) where a best fit method applied through the data presented in Figure 3.38.

The constants $K_1 = 85$ GPa, $K_2 = -171$ GPa, and $K_3 = 208$ GPa are the pressure coefficients to define for fully crushed curve and obtained from literature (Marsh, 1980) which are shock Hugoniot data for granite and quartz.

Due to the unavailable cyclic compression loading test data with this study, the damage constants D_1 , D_2 and $EF_{min} (\epsilon_p^f)$ were taken from literature (Holmquist et al., 1993). In Figure 3.42, the equivalent plastic strain at fracture (ϵ_p^f) was taken as 0.010. Setting $T^* = 0.083$, $P^* = 1/6$ and assuming $\epsilon_p^f + \mu_p^f = 0.01$ and $D_2 = 1.0$ in Equation 3.6. So, the constant D_1 , was determined as 0.04.

$$\epsilon_p^f + \mu_p^f = D_1(P^* + T^*)^{D_2} \quad (3.6)$$

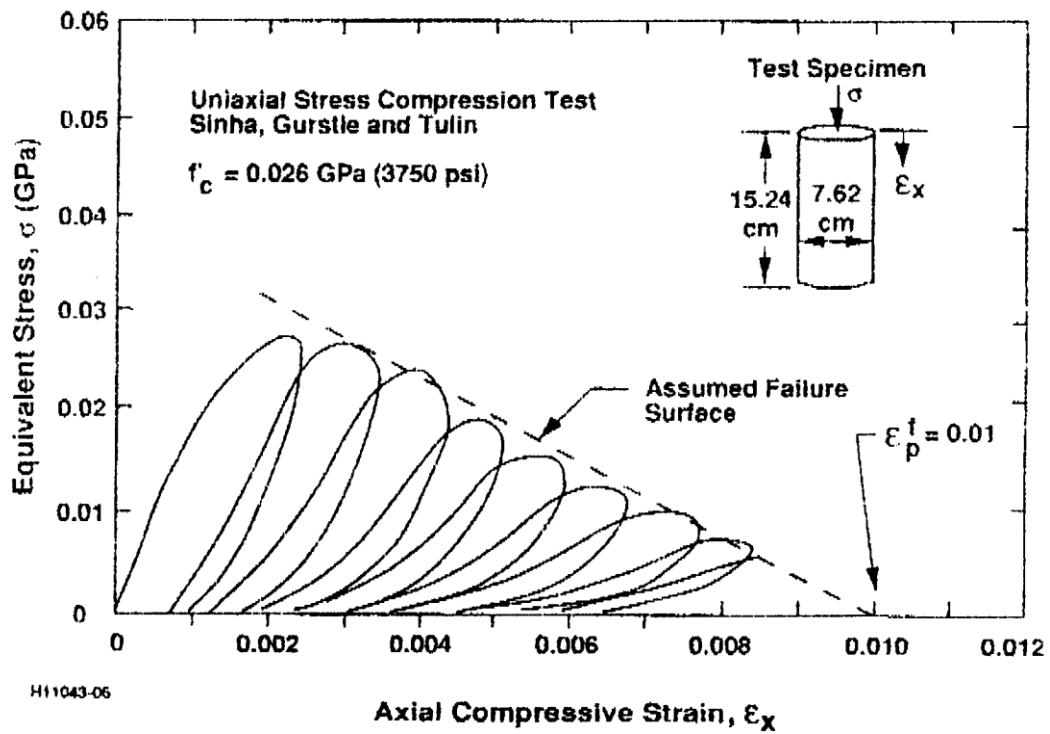


Figure 3.42. Stress-strain results of a cyclic compression test (Source: Holmquist et al., 1993)

The Johnson Holmquist Cook (HJC) material model parameters used in numerical analysis are presented in Table 3.2.

Table 3.2. Johnson Holmquist Cook material model parameters
 (*Source: Holmquist et al., 1993)

| | | |
|--|---|---------------------------|
| Material Properties | ρ_0 (Mass density) | 2183 (kg/m ³) |
| | ν (Poisson's ratio) | 0.2 |
| Strength Constants | A (Normalized cohesive strength) | 0.79* |
| | B (Normalized pressure hardening) | 0.90 |
| | N (Pressure hardening exponent) | 0.61* |
| | C (Strain rate coefficient) | 0.0205 |
| | f_c' (Quasi-static uniaxial compressive strength) | 62.08 (MPa) |
| | Smax (Normalized maximum strength) | 5.7 |
| | E (Elastic modulus) | 32 (GPa) |
| | G (Shear modulus) | 13.32 (GPa) |
| Damage Constants | K (Bulk modulus) | 17.77 (GPa) |
| | D ₁ (Damage constant) | 0.04* |
| | D ₂ (Damage constant) | 1.0* |
| Pressure Constants | EFMIN (Plastic strain before fracture) | 0.01 |
| | P _{crush} (Crushing pressure) | 21 (MPa) |
| | μ_{crush} (Crushing volumetric strain) | 0.001 |
| | K ₁ (Pressure constant) | 85 (GPa)* |
| | K ₂ (Pressure constant) | -171 (GPa)* |
| | K ₃ (Pressure constant) | 208 (GPa)* |
| | P _{lock} (Locking pressure) | 80 (MPa)* |
| | μ_{lock} (Locking volumetric strain) | 0.173 |
| T (Maximum tensile hydrostatic pressure) | 6.3 (MPa) | |

CHAPTER 4

NUMERICAL STUDY

4.1 Introduction

Numerical modeling and analysis of this study cover the high strain rate behavior of concrete. After experimental tests and mechanical material characterization of concrete were completed, numerical analysis is one step further investigation of concrete under dynamic loading condition. In this context, validation of experimental SHPB test results was investigated by using finite element analysis (FEA) program.

Finite element method for this purpose is used as a tool to solve the complex structural problem by using partial differential equations. Finite element methods can be divided into two categories. These are explicit and implicit numerical methods. An implicit analysis requires a series of iterations for the solution of each step to establish equilibrium within a specified tolerance. It uses larger time steps than the explicit analysis since it is unconditionally stable. The implicit approach is more convenient for solving problems when time dependency is not an important factor such as static, quasi-static, linear and modal analysis. In contrast to implicit methods, the explicit solution is a function of time and the solution works with time step increments. The explicit method is not a matrix solution and no iteration needed. Therefore, computational time per load step is lower than implicit method. So, the explicit analysis is more suitable for non-linear dynamic problems such as impact, blast, and crush. LS-DYNA computer software is a suitable finite element program for investigation of the behavior of concrete which is exposed to impact loading conditions. Also, LS-DYNA is a powerful tool to solve problems especially including complex, non-linear, large deformations and transient dynamic finite element code with the explicit solver.

In this chapter, modeling of the SHPB test setup is described in detail and numerical results of the high strain rate test are compared with experimental results. Afterwards, design considerations for the specimen geometry used in an SHPB test are discussed. Various specimen geometries are presented within their effect to the dynamic stress equilibrium parameter.

4.2 Modeling of SHPB Test and Numerical Results

Three-dimensional numerical model of SHPB test setup was created in the LS-PrePost which is the preprocessor of LS-DYNA. Numerical test setup consists of 4 main solid parts. These solid parts are incident bar, transmitter bar, test specimen and aluminum insert discs. In most of the cases, Ls-PrePost was used to create and mesh these parts. However, ANSYS APDL software was used in some special cases where Ls-PrePost was unable to mesh parts. For meshing, three-dimensional hexahedron mesh type was used for its highest accuracy in the numerical computations. A hexahedron element has 8 vertices, 12 edges and 6 quadrilateral faces which is a cubic structure. Also, hexahedron elements were structured as mapped mesh. Mapped mesh is just used for quadrilateral area mesh or hexahedra volume mesh. Mapped mesh has a regular pattern and structure for elements. Main features of mapped mesh are that it contains a lower number of element than free mesh and it looks aesthetic.

In numerical analysis, bar components and the specimen are designed with having the same dimensions with the experimental setup. The test without pulse shaper was modeled with a striker for the wave generation within the impact. Whereas, the test with pulse shaper did not include any striker since the pulse-shaped incident wave was given directly to the strain gage location in the numeric model. A full three-dimensional model with striker contains 317950 total elements and 339999 nodes. The numerical model of the without pulse shaper test is shown in Figure 4.1.

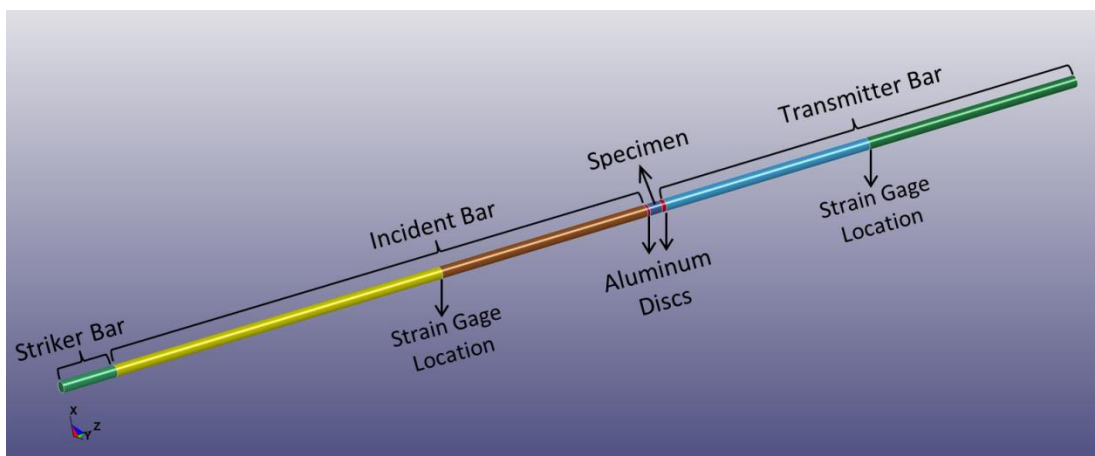


Figure 4.1. Numerical model of the Split Hopkinson Pressure Bar test

Material models for the aluminum bars and concrete specimen are embedded in LS_DYNA. MAT_ELASTIC material model was used for aluminum solid parts and MAT_JOHNSON_HOLMQUIST_CONCRETE material model was used for the concrete test specimen. Since aluminum bars remain elastic during the deformation of concrete in an SHPB test, an elastic material model was selected and material properties of aluminum 7075-T6 were inserted into that material model. Likewise, the material model parameters of JOHNSON_HOLMQUIST_CONCRETE were inserted within the parameters which were found in this study. The striker and the incident bar impact was modeled using SURFACE_TO_SURFACE contact type. Static and dynamic coefficients of friction were set to 0.3 and 0.2, respectively. A node set was defined to the specimen and this node set was contacted with bar-specimen interfaces. Contact type for bar-specimen interfaces was NODE_TO_SURFACE. Since grease was used to minimize friction effect in the bar-specimen interfaces, static and dynamic coefficients of friction were set to 0.1 and 0.05, respectively.

The impact velocity of the striker bar was generated in the model having 22.8 m/s and then this impact created a 200 MPa incident wave amplitude. The result of the bar stresses as a function of time for the numerical without pulse shaper test is presented in Figure 4.2.

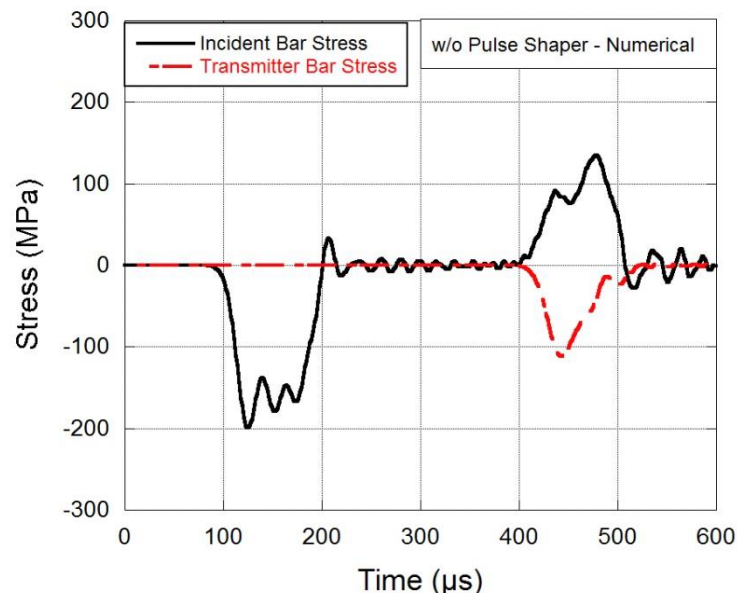


Figure 4.2. Stress history of the numerical test without pulse shaper

Stress wave analysis was also performed for the numerical study. 1-wave, 2-wave and 3-wave analyses were done using the formulation which was given in chapter 2. The experimental and numerical comparative results of the wave analysis were given in Figure 4.3. Although it was seen that experimental and numerical results provided very close agreement, the numerical one-wave analysis showed the best agreement with the experimental result.

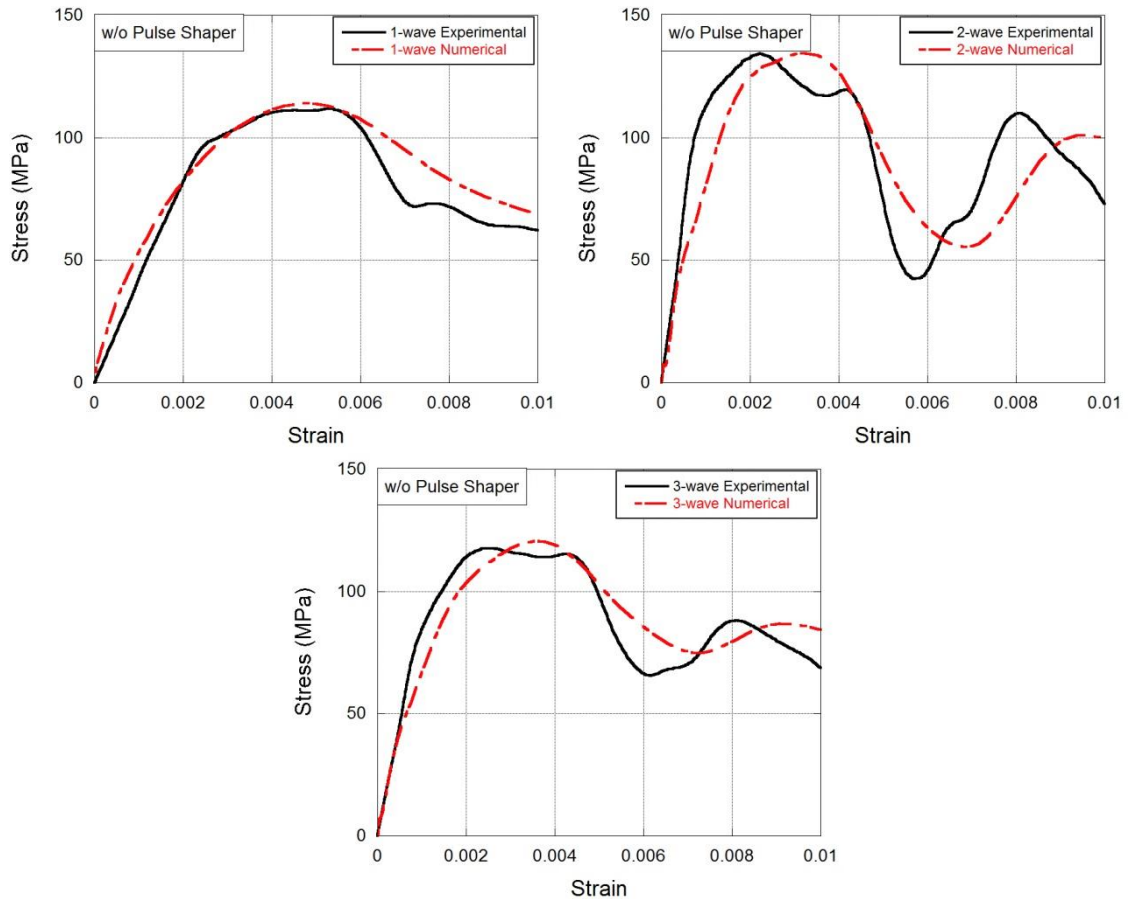


Figure 4.3. Experimental and numerical Comparison of stress-strain wave analysis of test without pulse shaper

Numerical comparison of the 1-wave, 2 wave, and 3-wave stress-strain curves are presented in Figure 4.4 where similar trend with the experimental results are seen. At the failure of the sample, one-wave analysis shows the lowest stress and highest strain values. Two-wave analysis illustrates the highest stress and lowest strain values and three-wave analysis shows the stress-strain values in between one-wave and two-wave analysis.

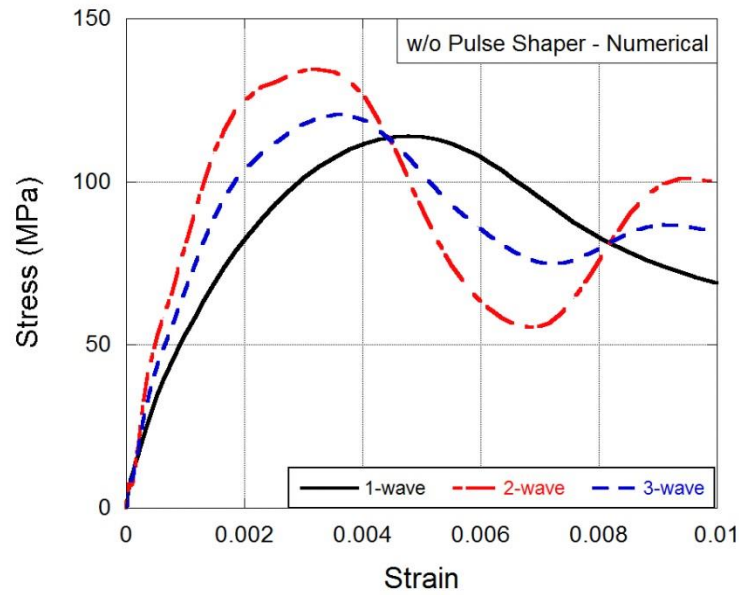


Figure 4.4. Numerical stress wave analysis of the test without pulse shaper

The strain-strain rate comparison of the numerical and experimental result of the without pulse shaper test is given in Figure 4.5. Again, numerical and experimental results present a very good agreement. Both results show that strain rate at the failure is found as 244 s^{-1} where strain is measured as 0.0047.

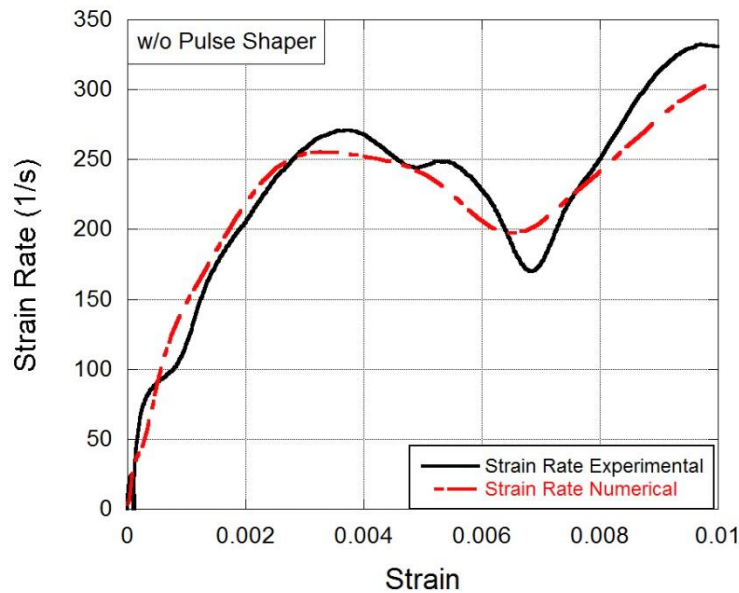


Figure 4.5. Comparison of the experimental and numerical strain-strain rate history of the without pulse shaper test

Dynamic stress equilibrium parameter, $R(t)$ has also a similar pattern in both experimental and numerical result in the test without pulse shaper as shown in Figure 4.6. However, after the failure strain which is 0.0047, the curves diverge from each other which are an expected situation due to the wave distortion. Both curves approach nearly zero $R(t)$ value as strain value moves towards peak strain

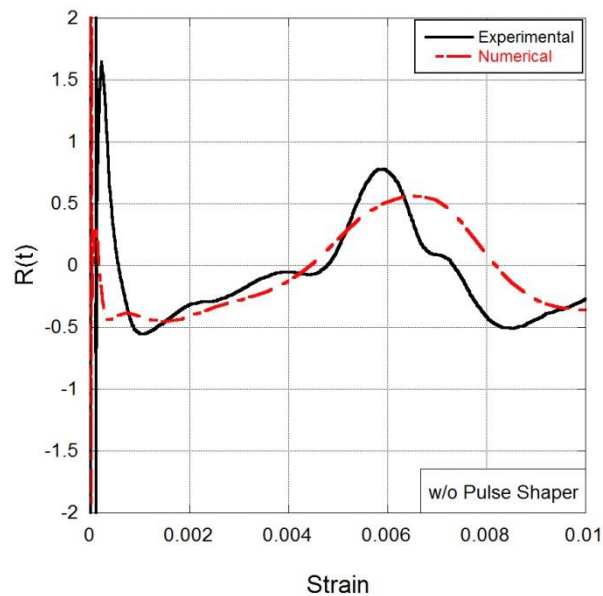


Figure 4.6. Comparison of the experimental and numerical $R(t)$ parameter of the test without pulse shaper

A comparative study of experimental and numerical test with pulse shaper was also performed. An experimental incident pulse was generated numerically at the strain gage location on the incident bar. Then, wave propagation this numerical incident pulse created numerical reflected and transmitter stress waves as seen in in Figure 4.7. The amplitude of the numerically generated incident pulse was recorded as 211 MPa. It can be seen that numerical result of the test with pulse shaper (Figure 4.7) presents much smoother and non-oscillatory stress history than the test without pulse shaper (Figure 4.2).

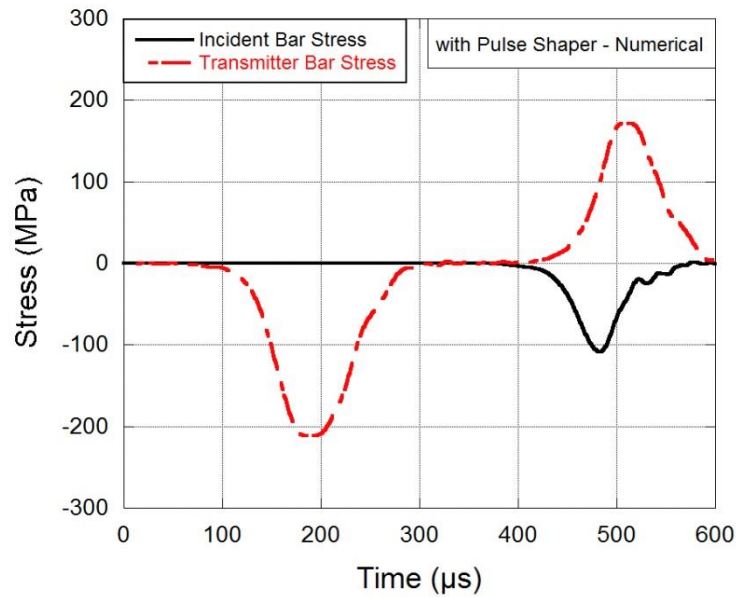


Figure 4.7. Stress history of the numerical test with pulse shaper

The stress-strain curves of one-wave, two-wave and three-wave stress analysis are shown in Figure 4.8. One-wave analysis performs a good agreement for both experimental and numerical analysis. Moreover, the numerical one-wave analysis shows smoother curve without any fluctuations unlike experimental results. Thus, in the numerical one-wave analysis, it is easier and more apparent to determine peak stress and strain values at the failure. However, two-wave and three-wave stress analyses show a very distinctive behavior for the experimental and numerical pulse shaper test. Although peak stresses are 125 MPa for both experimental and numerical two-wave analysis, strain values are very different at these peak stresses where 0.0090 for experimental and 0.0050 for numerical analysis. For three-wave analysis, same behavior with the two-wave analysis occurred. In experimental analysis strain value at the peak stress was 0.0030 higher than the numerical strain. Three-wave peak stresses are 118 MPa and 113 MPa for experimental and numerical analysis, respectively. These results show that experimental two-wave and three-wave results may be misleading determining stress and strain values. So, it is much more trustworthy to use one-wave analysis to determine stress-strain values with the help of numerical analysis.

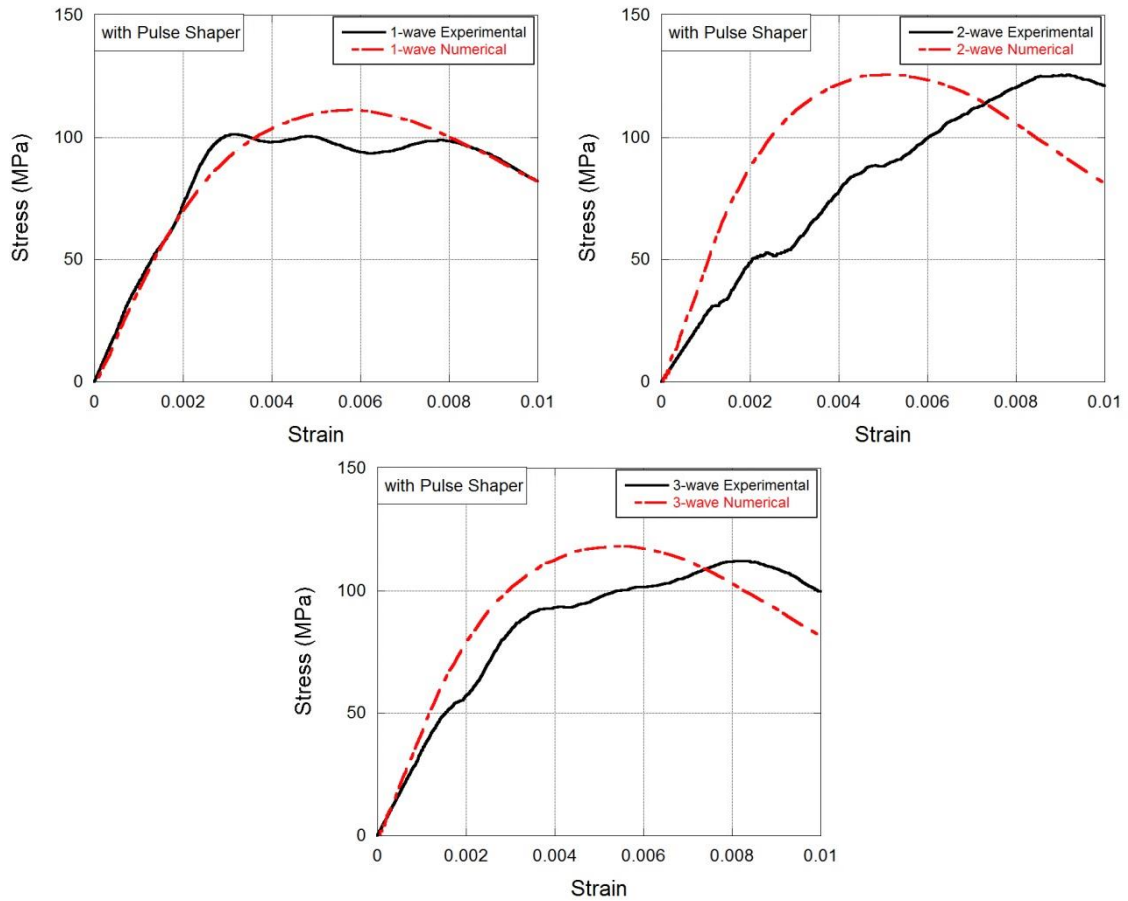


Figure 4.8. Experimental and numerical Comparison of stress-strain wave analysis of test with pulse shaper

One-wave, two-wave and three-wave stress analysis comparison of the numerical test with pulse shaper is presented in Figure 4.9. It is seen that stress wave analysis in numerical pulse shaper test gives closer results among those stress-strain curves. One-wave, two-wave and three-wave stress-strain curves have the similar initial stress rise and post-peak stresses. Likewise, other stress analysis curves, one-wave stress gives the lowest stress value at the peak, two-wave gives highest and three-wave is in the middle but these stress differences are the 7-8 MPa and strain values at these stress levels are very similar for those stress-strain curves.

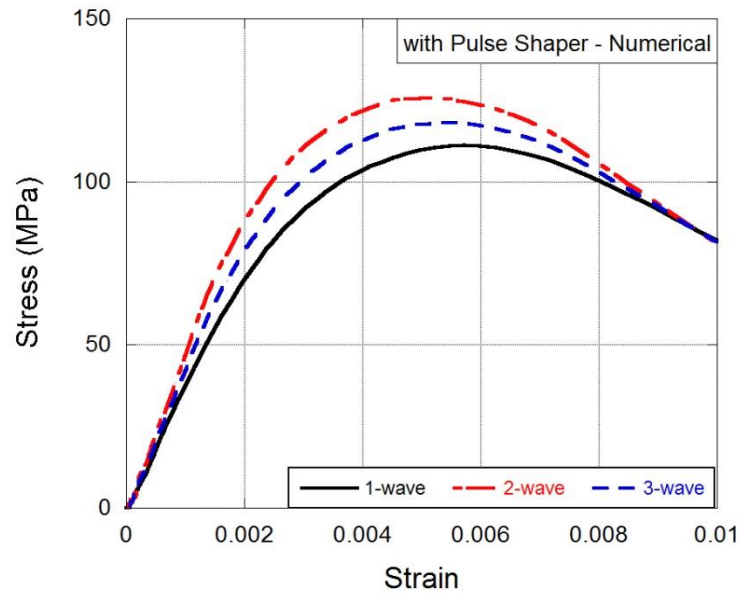


Figure 4.9. Numerical stress wave analysis of the test with pulse shaper

Figure 4.10 illustrates the comparison of experimental and numerical strain rate curve as a function of strain for the test with pulse shaper. It was seen that both experimental and numerical curves increased continuously along the observed strain range. However, experimental strain rate data showed a little fluctuation over the strain range. It was found that experimental strain rate was determined as 244 s^{-1} whereas numerical strain rate was 265 s^{-1} at failure strain 0.0057.

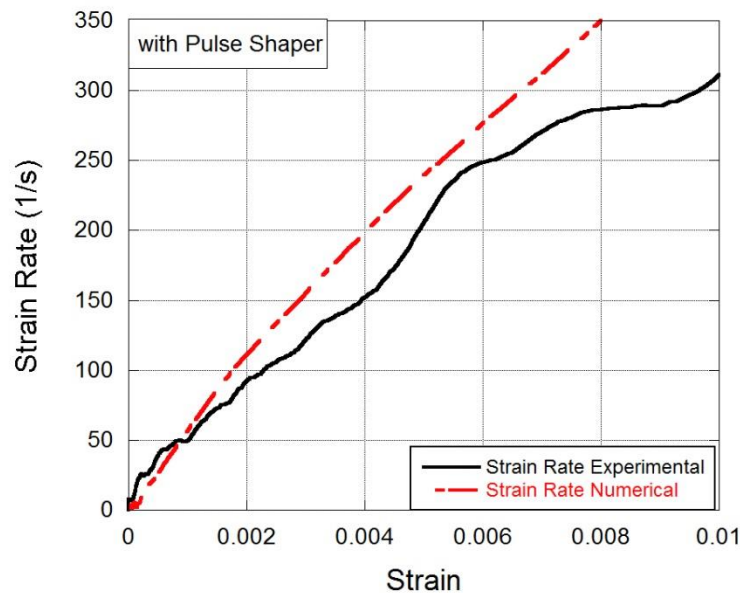


Figure 4.10. Comparison of the experimental and numerical strain-strain rate history of the test with pulse shaper

Stress equilibrium parameter showed a pretty good agreement in both experimental and numerical data except the initial stress rising portion until 0.0040 strain. After strain value reaches 0.0040, both experimental and numerical data followed a very similar curve which is pretty close to stress equilibrium.

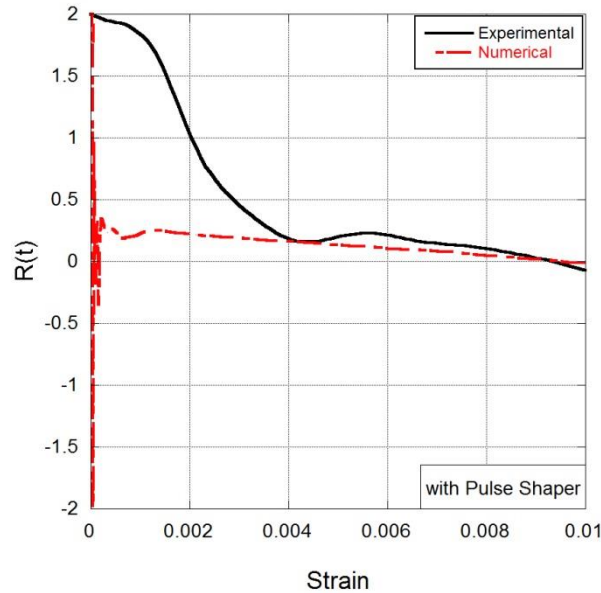


Figure 4.11. Comparison of the experimental and numerical $R(t)$ parameter of the test with pulse shaper

4.3 Numerical Study on the SHPB Specimen Geometry

Homogeneous and uniform stress distribution over the specimen length is an important factor for a Split Hopkinson Pressure Bar test so that the data taken from the test is valid, accurate and reliable. For this purpose, equilibrium parameter $R(t)$, which can be calculated by using either stress or force on both front and back specimen-bar interfaces is used to show the validation of uniform and uniaxial state of stress within the specimen. In order to make this assumption, loading pulse duration should be chosen enough longer such that there are sufficient wave reflections through specimen before failure.

To investigate the effect of specimen geometry on the dynamic stress equilibrium parameter, two different geometric parameters were examined. First, specimen length to diameter (L/D) ratio was changed from 0.25 to 1.25 with 0.25 increments. While keeping the diameter of the test specimen constant at 39.50 mm, the length of the specimen was changed with the relevant L/D ratio. In Figure 4.12,

numerical test specimens which have L/D ratio of 0.25, 0.50, 0.75, 1.0 and 1.25 are presented respectively.

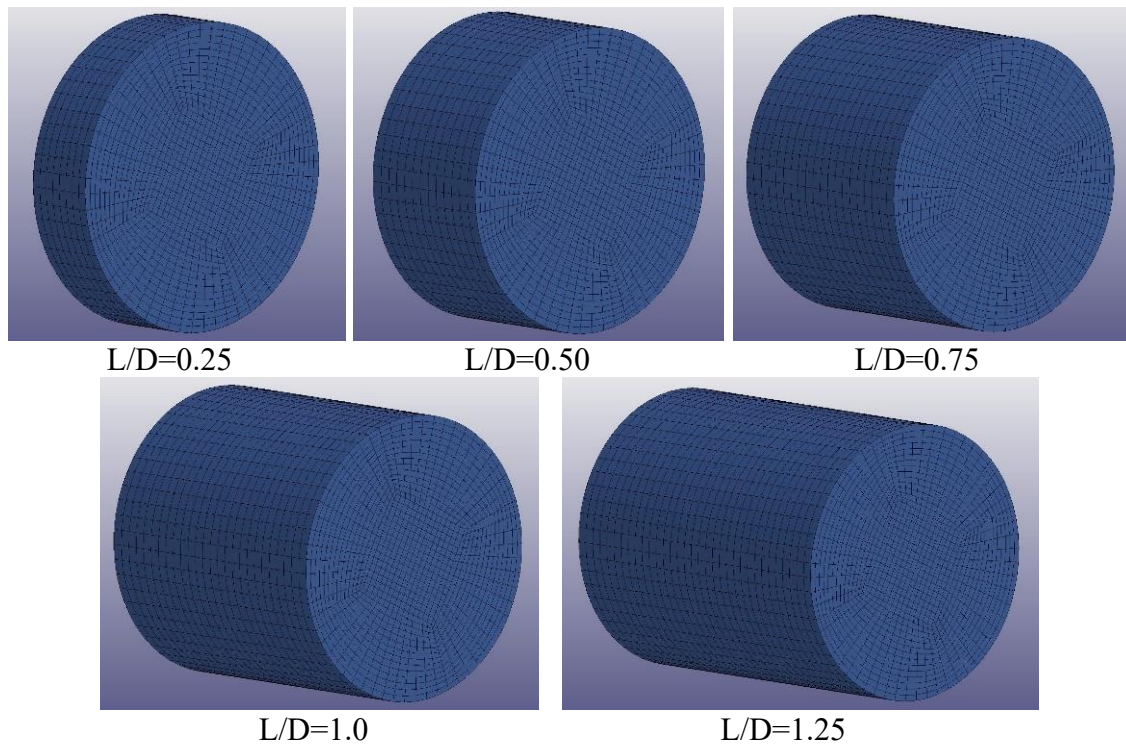


Figure 4.12. Numerical test specimens with different L/D ratio

In the numerical analysis of these set of different numerical test specimens, an incident pulse obtained in the SHPB experiments was generated as a compressive pulse in the incident bar. $R(t)$ parameters as a function of strain in the test with and without pulse shaper are presented in Figure 4.13 and Figure 4.14. It was figured out that specimen L/D ratio and usage of a pulse shaper affect $R(t)$ parameter considerably. As the L/D ratio decreases, $R(t)$ reaches nearly stress equilibrium earlier than the greater L/D ratios. This is caused by reverberation time increases as the specimen length increases. Since it was stated that it requires 3-4 reverberations (time for stress pulse travel back and front of the specimen) to reach dynamic stress equilibrium in a ceramic specimen (Subhash and Ravichandran, 2000), the results obtained from numerical L/D ratio trials proved that the time to reach nearly stress equilibrium increases as the length of specimen increases. When L/D ratio is chosen as 0.25, equilibrium parameter does not change with the deformation or time in the test with pulse shaper. However, as the L/D ratio increases, $R(t)$ value in the earlier of the deformation increases and reaches equilibrium by time. One of the reasons for the higher stress difference in the earlier of

the deformation is that stress values at those strains are so small that the ratio of stress difference gives bigger $R(t)$ values.

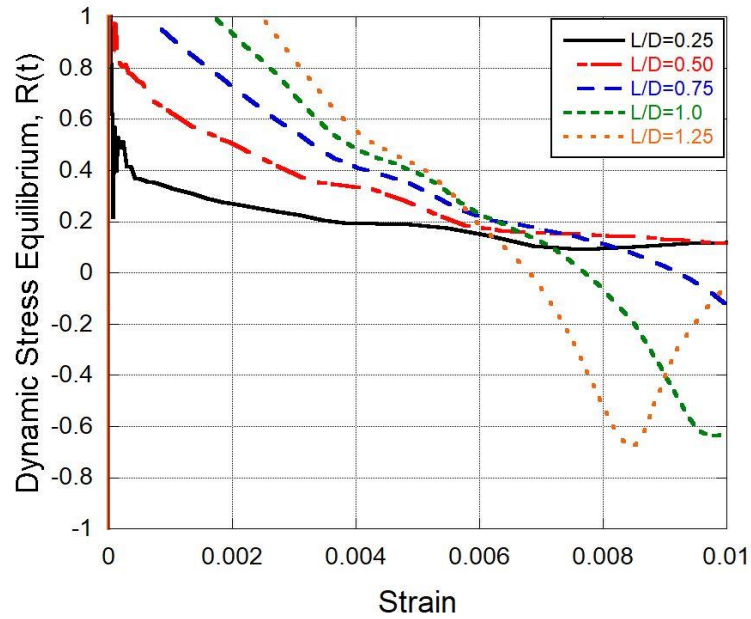


Figure 4.13. The effect of L/D ratio on the dynamic stress equilibrium parameter in the test without pulse shaper

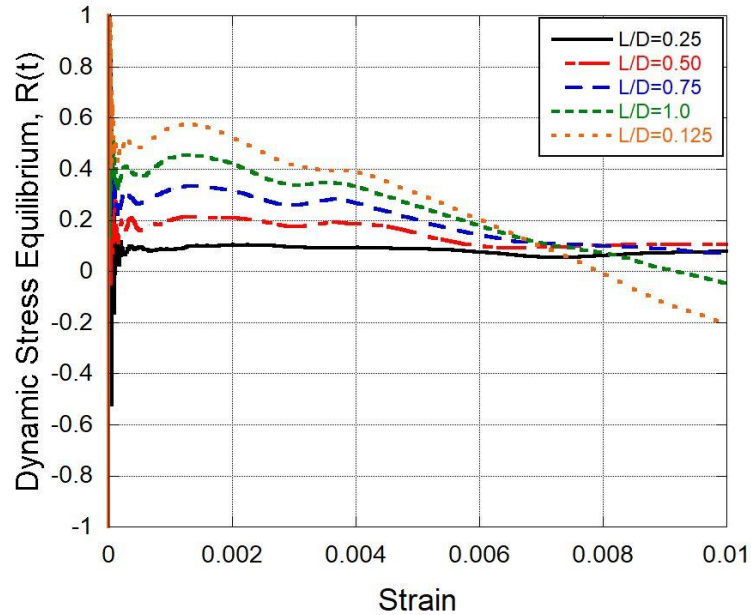


Figure 4.14. The effect of L/D ratio on the dynamic stress equilibrium parameter in the test with pulse shaper

Next, the effect of annular specimen geometries on the dynamic equilibrium was investigated. In this geometry, the length and the outer diameter of the specimen was chosen same as the test specimen used in experiments which is 45 mm in length and

39.50 mm diameter. Three different annular specimen geometries were created having the ratio of inner radius to outer radius 0.25, 0.50, and 0.75, respectively as shown in Figure 4.15. The annular geometry indicates that the ratio of the radius of the hole in the center divided by the specimen outer diameter.

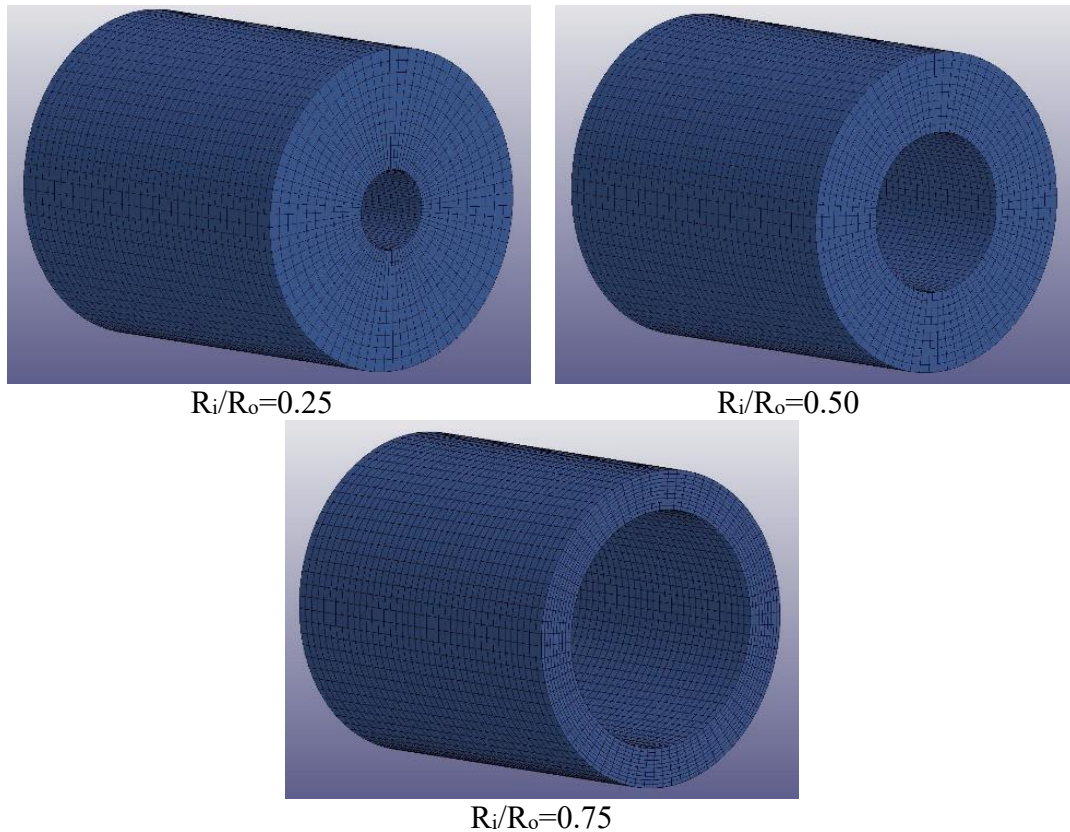


Figure 4.15. Numerical test specimens with different R_i/R_o ratio

The results obtained from annular specimen geometry showed that specimen R_i/R_o ratio does not affect the dynamic stress equilibrium parameter as L/D ratio does. There are small differences in between full cylinder geometry and other annular geometries. So, it can be said that the annular specimens have negligible effect on the stress equilibrium. Also, it must be considered manufacturing of these complex geometries are costly and needs more careful.

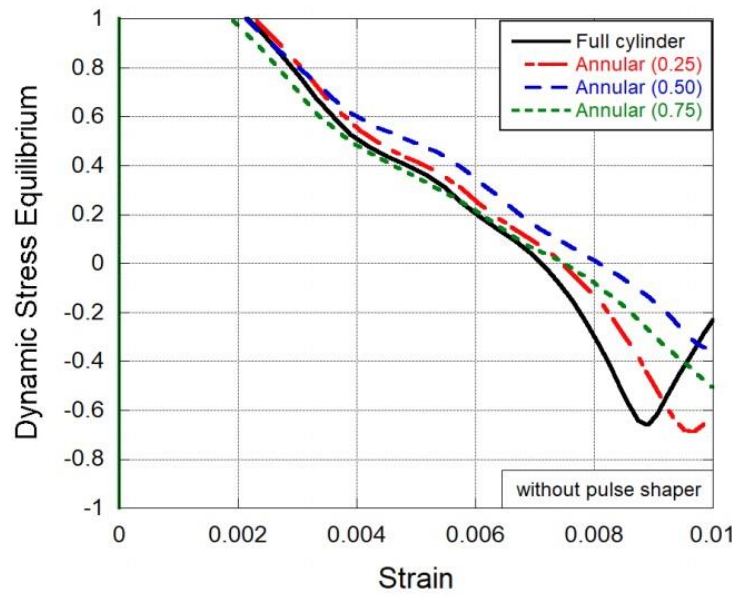


Figure 4.16. The effect of annular specimen geometry on the dynamic stress equilibrium parameter in the test without pulse shaper

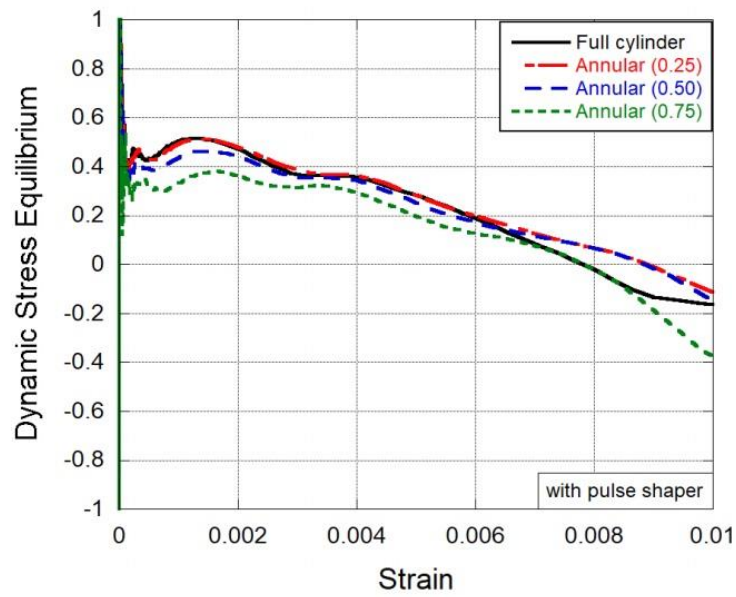


Figure 4.17. The effect of annular specimen geometry on the dynamic stress equilibrium parameter in the test with pulse shaper

CHAPTER 5

CONCLUSIONS

In this study, dynamic mechanical characterization of concrete was performed by implementing unique techniques for both experimental tests and numerical analyses. The methodology and process which were followed during the experimental and numerical study were presented. Quasi-static and high strain rate compression tests to determine the compressive mechanical behavior of concrete were completed. Split Hopkinson pressure bar test apparatus was found to be a successful testing methodology to determine dynamic behavior of concrete.

EPDM rubber circular pulse shaper was used in the SHPB tests. To see the effect of pulse shaper, SHPB tests were also performed without pulse shaper. It was seen that having the similar incident pulse amplitude, pulse duration increased from 115 microseconds to 220 microseconds. Also using pulse shaper provided a ramp pulse which is non-oscillatory stress wave propagates through the specimen. This non-oscillatory ramped incident pulse ensured uniform and uniaxial stress distribution in the specimen as well as obtaining nearly constant strain rate.

Piezo-electric quartz crystals as a force transducer were embedded on the specimen-bar interfaces. Such an application has not yet been carried out when testing of concrete and concrete-like materials. Quartz crystal force transducers are capable of measuring force-time histories of front and back faces of the test specimen in a real-time having higher sensitivity and accuracy than strain gages. It was seen that especially in the test without pulse shaper, quartz crystals provided non-oscillatory and correct force measurements comparing to force obtained from strain gages.

In quasi-static experiments, the uniaxial compressive strength of the concrete specimen was found as 62 MPa in average at the lowest range of strain rate. Tensile strength was determined as 6.34 MPa according to splitting tensile test results. The mechanical properties of the concrete were determined using quasi-static test results using strain gage mounted specimen. The Young's modulus, shear modulus, Poisson's ratio, and the density of the concrete were determined. In dynamic tests, compressive strength of concrete increased twice as much in the quasi-static test. Peak stresses were

measured as 101 MPa (at 242 s⁻¹ strain rate) and 110 MPa (at 244 s⁻¹ strain rate) in the test with and without pulse shaper, respectively.

The numerical simulations were executed using commercial finite element software LS-DYNA. Holmquist-Johnson-Cook (HJC) material model which is a built-in material model in LS-DYNA as MAT_111 was used in numerical analyses. It was deduced that this material model is highly rate sensitive. Taking into consideration of rate sensitivity of concrete, strain rate parameter (C) was determined according to quasi-static test results. C parameter calculated from both quasi-static and dynamic tests overestimated the strength of concrete.

Experimental and numerical results showed very good agreement. SHPB tests with and without pulse shaper were investigated numerically. The stress-strain, strain rate and dynamic stress equilibrium parameter comparisons were made between numerical and experimental results. From the results, it was seen that LS-DYNA is a powerful tool for simulation of SHPB tests.

Damage profiles of quasi-static and high strain rate compression tests were shown from the images captured using high-speed camera. It was observed that crack and failure pattern of quasi-static and dynamic tests were distinctive. In the quasi-static test the specimen failed at the weakest point and new cracks occurred by time. Since there is no time for crack growth in dynamic test, several cracks occurred simultaneously in failure. Also, it was observed that cracks occurred through aggregates in the dynamic tests causing dynamic strength increase of concrete.

Numerical study showed that specimen geometry has a great influence on dynamic stress equilibrium parameter. The specimen having smaller length reaches dynamic equilibrium earlier as compared to other specimen having same diameter. However, when designing the specimen geometry, limitations must be considered such as maximum aggregates size to length of the specimen ratio on the concrete material. Also, tubular geometry trials did not show apparent effect on the dynamic equilibrium.

The improvements and suggestions that can be studied for future work can be listed as follows:

- New insert geometries may be applied to the bar-specimen interfaces to prevent stress concentrations on the specimen-bar interfaces. Also, a well-designed insert geometry may improve uniform stress distribution over the specimen. Also, different specimen geometries other than the annular or having various length to diameter ratios may be tried but it

must be considered that manufacturing such a complex specimen geometry would be hard to obtain and costly in a ceramic material like concrete.

- Damage and crack profiles were captured using a high-speed camera. Using a high-speed camera coupling with a digital image correlation (DIC) system may be used for better strain measurements and observe damage and crack profiles more clearly.
- The methodology followed in this study can be implemented to the mechanical characterization of other materials. Especially using quartz crystal force transducers may provide non-oscillatory and reliable force measurements for brittle materials.

REFERENCES

- 211, A. C. (2002). Standard Practice for Selecting Proportions for Normal, Heavyweight, and Mass Concrete (ACI 211.1-91). *Concrete*, 91(Reapproved), 1–38.
- A. Ross, C. (1989). *Split-Hopkinson Pressure Bar Tests*.
- ACI Committee 318. (2008). *Building Code Requirements for Structural Concrete (ACI 318-08)*. American Concrete Institute (Vol. 2007).
- ASTM C496. (2011). ASTM C496-11 Standard Test Method for Splitting Tensile Strength of Cylindrical Concrete Specimens. *Annual Book of ASTM Standards Volume 04.02*, 1–5.
- Bagher Shemirani, A., Naghdabadi, R., & Ashrafi, M. J. (2016). Experimental and numerical study on choosing proper pulse shapers for testing concrete specimens by split Hopkinson pressure bar apparatus. *Construction and Building Materials*, 125, 326–336.
- Bancroft, D. (1941). The Velocity of Longitudinal Waves in Cylindrical Bars. *Phys. Rev.*, 59(7), 588–593.
- Bischoff, P. H., & Perry, S. H. (1991). Compressive behaviour of concrete at high strain rates. *Materials and Structures*, 24(6), 425–450.
- Chen, W. (1995). *Dynamic Failure Behavior of Ceramics under Multiaxial Compression, 1995*.
- Chen, W., Lu, F., & Zhou, B. (2000). A quartz-crystal-embedded split Hopkinson pressure bar for soft materials. *Experimental Mechanics*, 40(1), 1–6.
- Chen, X., Ge, L., Zhou, J., & Wu, S. (2016). Experimental Study on Split Hopkinson Pressure Bar Pulse-Shaping Techniques for Concrete. *Journal of Materials in Civil Engineering*, 28(5), 4015196.
- Chen, X., Ge, L., Zhou, J., & Wu, S. (2017). Dynamic Brazilian test of concrete using split Hopkinson pressure bar. *Materials and Structures*, 50(1), 1.
- Chen, X., Wu, S., & Zhou, J. (2013). Experimental and modeling study of dynamic mechanical properties of cement paste, mortar and concrete. *Construction and Building Materials*, 47, 419–430.
- Cui, J., Hao, H., & Shi, Y. (2017). Discussion on the suitability of concrete constitutive models for high-rate response predictions of RC structures. *International Journal of Impact Engineering*, 106, 202–216.

- Davies, R. M. (1948). A Critical Study of the Hopkinson Pressure Bar. *Philosophical Transactions of the Royal Society of London. Series A, Mathematical and Physical Sciences*, 240(821), 375–457.
- Dehestani, M., Nikbin, I. M., & Asadollahi, S. (2014). Effects of specimen shape and size on the compressive strength of self-consolidating concrete (SCC). *Construction and Building Materials*, 66, 685–691.
- Frew, D. J., Forrestal, M. J., & Chen, W. (2002). Pulse shaping techniques for testing brittle materials with a split hopkinson pressure bar. *Experimental Mechanics*, 42(1), 93–106.
- Gama, B. A., Lopatnikov, S. L., & Gillespie, J. W. (2004a). Hopkinson bar experimental technique: A critical review. *Applied Mechanics Reviews*, 57(4), 223.
- Gama, B. A., Lopatnikov, S. L., & Gillespie, J. W. (2004b). Hopkinson bar experimental technique: A critical review. *Applied Mechanics Reviews*, 57(4), 223.
- Goldsmith, W., Polivka, M., & Yang, T. (1966). Dynamic Behavior of Concrete. *Experimental Mechanics*, 65–79.
- Gray, G. (2000). Classic Split-Hopkinson Pressure Bar Testing. *Materials Park, OH: ASM International, 2000.*, 8, 462–476.
- Hanchak, S. J., Forrestal, M. J., Young, E. R., & Ehrgott, J. Q. (1992). Perforation of concrete slabs with 48 MPa (7 ksi) and 140 MPa (20 ksi) unconfined compressive strengths. *International Journal of Impact Engineering*, 12(1), 1–7.
- Hao, Y., & Hao, H. (2011). Numerical Evaluation of the Influence of Aggregates on Concrete Compressive Strength at High Strain Rate. *International Journal of Protective Structures*, 2(2), 177–206.
- Hao, Y., Hao, H., Jiang, G. P., & Zhou, Y. (2013). Experimental confirmation of some factors influencing dynamic concrete compressive strengths in high-speed impact tests. *Cement and Concrete Research*, 52, 63–70.
- Hao, Y., Hao, H., & Li, Z. X. (2010). Numerical analysis of lateral inertial confinement effects on impact test of concrete compressive material properties. *International Journal of Protective Structure*, 1(1), 145–167.
- Hao, Y., Hao, H., & Li, Z. X. (2013). Influence of end friction confinement on impact tests of concrete material at high strain rate. *International Journal of Impact Engineering*, 60, 82–106.
- Holmquist, T. J., Johnson, G. R., & Cook, W. H. (1993). A computational constitutive model for concrete subjected to large strains, high strain rates, and high pressures.pdf. *14th International Symposium on Ballistic, Quebec City, Canada.*

- Hopkinson, B. (1914). X. A method of measuring the pressure produced in the detonation of high explosives or by the impact of bullets. *Philosophical Transactions of the Royal Society of London A: Mathematical, Physical and Engineering Sciences*, 213(497–508), 437–456.
- Hopkinson, J., & Hopkinson, B. (1901). *Original Papers by the Late John Hopkinson: Technical papers*. University Press.
- Johnson, G. R., Beissel, S. R., Holmquist, T. J., & Frew, D. J. (1998). Computed radial stresses in a concrete target penetrated by a steel projectile. In *Proceedings of the 5th International Conference on Structures under shock and impact, Portsmouth, UK* (pp. 793–806).
- Karnes, C. H., & Ripperger, E. a. (1966). Strain rate effects in cold worked high-purity Aluminium. *Journal of the Mechanics and Physics of Solids*, 14, 75–88.
- Khoogar, A. R., Mohades, M. A., and Vahedi, K. (2013). Int J Advanced Design and Manufacturing Technology. *Int J Advanced Design and Manufacturing Technology*, 6(3), 1–7.
- Kolsky, H. (1949). An Investigation of the Mechanical Properties of Materials at very High Rates of Loading. *Proceedings of the Physical Society. Section B*, 62(11), 676–700.
- Krafft, J. M., Sullivan, A. M., & Tipper, C. F. (1954). The Effect of Static and Dynamic Loading and Temperature on the Yield Stress of Iron and Mild Steel in Compression. *Proceedings of the Royal Society of London. Series A, Mathematical and Physical Sciences*, 221(1144), 114–127.
- Landon, J. W., & Quinney, H. (1923). Experiments with the Hopkinson Pressure Bar. *Proceedings of the Royal Society of London, Series A*, 103, 622–643.
- Li, Q. M., Lu, Y. B., & Meng, H. (2009). Further investigation on the dynamic compressive strength enhancement of concrete-like materials based on split Hopkinson pressure bar tests. Part II: Numerical simulations. *International Journal of Impact Engineering*, 36(12), 1335–1345.
- Li, Q. M., & Meng, H. (2003). About the dynamic strength enhancement of concrete-like materials in a split Hopkinson pressure bar test. *International Journal of Solids and Structures*, 40(2), 343–360.
- Lindholm, U. S. (1964). Some experiments with the split hopkinson pressure bar*. *Journal of the Mechanics and Physics of Solids*, 12(5), 317–335.
- Livermore Software Technology Corporation. (2016). *LS-DYNA Keyword User's Manual Volume II Material Models. LS-DYNA Keyword User's Manual (Vol. II)*.
- Lu, D., Wang, G., Du, X., & Wang, Y. (2017). A nonlinear dynamic uniaxial strength criterion that considers the ultimate dynamic strength of concrete. *International Journal of Impact Engineering*, 103, 124–137.

- Malvern, L. E., Jenkins, D. A., Tang, T., & Ross, C. A. (1985). Dynamic compressive testing of concrete. *Proceedings of Second Symposium on the Interaction of Non-Nuclear Munitions with Structures*, 194–199.
- Marsh, S. P. (1980). LASL Shock Hugoniot Data. *Los Alamos Series on Dynamic Material Properties*, 150.
- Meyer, C. S. (2011). Development of Geomaterial Parameters for Numerical Simulations Using the Holmquist-Johnson-Cook Constitutive Model for Concrete.
- Mu, Z. C., Dancygier, A. N., Zhang, W., & Yankelevsky, D. Z. (2012). Revisiting the dynamic compressive behavior of concrete-like materials. *International Journal of Impact Engineering*, 49, 91–102.
- Ramírez, H., & Rubio-Gonzalez, C. (2006). Finite-element simulation of wave propagation and dispersion in Hopkinson bar test. *Materials and Design*, 27(1), 36–44.
- Rossi, P. (1991a). A physical phenomenon which can explain the mechanical behavior of concrete under high strain rates. *Materials and Structures*, 24, 422–424.
- Rossi, P. (1991b). Influence of cracking in the presence of free water on the mechanical behaviour of concrete, (154), 53–57.
- Rossi, P., van Mier, J. G. M., Boulay, C., & Le Maou, F. (1992). The dynamic behaviour of concrete: influence of free water. *Materials and Structures*, 25(9), 509–514.
- Song, B., & Chen, W. (2004). Dynamic stress equilibration in split Hopkinson pressure bar tests on soft materials. *Experimental Mechanics*, 44(3), 300–312.
- Song, B., & Chen, W. (2005). Split Hopkinson pressure bar techniques for characterizing soft materials. *Latin American Journal of Solids and Structures*, 2(June), 113–152.
- Song, B., Chen, W. W., & Lu, W. Y. (2007). Mechanical characterization at intermediate strain rates for rate effects on an epoxy syntactic foam. *International Journal of Mechanical Sciences*, 49(12), 1336–1343.
- Subhash, G., & Ravichandran, G. (2000). Split-Hopkinson Pressure Bar Testing of Ceramics. *ASM Handbook, Volume 8: Mechanical Testing and Evaluation*, 8, 497–504.
- Sunny, G., Yuan, F., Prakash, V., & Lewandowski, J. (2009). Design of inserts for split-hopkinson pressure bar testing of low strain-to-failure materials. *Experimental Mechanics*, 49(4), 479–490
- Tai, Y. S. (2009). Flat ended projectile penetrating ultra-high strength concrete plate target. *Theoretical and Applied Fracture Mechanics*, 51(2), 117–128.

- Tasdemirci, A., Cankaya, M. A., Seven, S. B., Uysal, C., & Saatci, S. (2016). The effect of pulse shaping on the dynamic mechanical behavior of concrete. In *22nd DYMAT Technical Meeting, Grenoble - 2016* (pp. 56–60).
- Tasdemirci, A., Çankaya, M. A., Seven, B. S., Uysal, E. Ç., Saatcı, S., & Güden, M. (2018). The effect of strain rate on the compressive mechanical behavior of concrete. *International Journal of Impact Engineering*, under revision.
- Tasdemirci, A., Turan, A. K., & Guden, M. (2012). The effect of strain rate on the mechanical behavior of Teflon foam. *Polymer Testing*, *31*(6), 723–727.
- Tedesco, J. W., & Ross, C. A. (1998). Strain-Rate Dependent Constitutive Equations for Concrete. *Journal of Pressure Vessel Technology*, *120*(4), 1053–1067.
- Togami, T. C., Baker, W. E., & Forrestal, M. J. (1996). A split Hopkinson pressure bar technique to evaluate the performance of accelerometers. *Trans. ASME: J. Appl. Mech.*, *63*(June 1996), 353–356.
- Wasley, R. J., Hoge, K. G., & Cast, J. C. (1969). Combined strain gauge - Quartz crystal instrumented Hopkinson split bar. *Review of Scientific Instruments*, *40*(7), 889–894.
- Zhang, J., Wang, Z., Yang, H., Wang, Z., & Shu, X. (2018). 3D meso-scale modeling of reinforcement concrete with high volume fraction of randomly distributed aggregates. *Construction and Building Materials*, *164*, 350–361.
- Zhou, X. Q., & Hao, H. (2008). Modelling of compressive behaviour of concrete-like materials at high strain rate. *International Journal of Solids and Structures*, *45*(17), 4648–4661.
- Zhou, Z., Chen, P., Guo, B., & Huang, F. (2012). Dynamic tensile deformation and fracture of a highly particle-filled composite using SHPB and high-speed DIC method. *EPJ Web of Conferences*, *26*, 1005.